AD NUMBER
ADC074755
CLASSIFICATION CHANGES
TO: unclassified
FROM: confidential
LIMITATION CHANGES
TO: Approved for public release, distribution unlimited
FROM: Distribution: Further dissemination only as directed by Defense Advanced Research Projects Agency, ATTN: TIO, 3701 North Fairfax Dr., Arlington, VA 22203, DEC 1969, or higher DoD authority.
AUTHORITY
NRL ltr dtd 3 Sep 2003; NRL ltr dtd 3 Sep 2003

Gp-3

CONFIDENTIAL

~~SECRET~~

NRL Memorandum Report 2072
Copy No. 64 of 150 Copies

NRL EIGHTH CARD Program Interim Progress Report 1 March 1969 to 30 September 1969

[Unclassified Title]

H. W. GANDY

December 31, 1969

EIGHTH CARD Program. This report may not be distributed further by the holder or released outside the holder's organization, except with the specific approval of ARPA/TIO. No distribution to DDC is authorized. This report may be cited, abstracted or quoted only in documents bearing the EIGHTH CARD notation. Information contained herein may be released only to persons known by the holder to be on the master access list of persons who have been authorized access to controlled EIGHTH CARD information.

NAVAL RESEARCH LABORATORY
Washington, D.C.

CONFIDENTIAL

SECURITY

This document contains information affecting the national defense of the United States within the meaning of the Espionage Laws, Title 18, U.S.C., Sections 793 and 794. The transmission or revelation of its contents in any manner to an unauthorized person is prohibited by law.

The work described in this technical progress report has been sponsored by the Naval Ordnance Systems Command, Code 0832, under OrdTask ORD-0832-129/173-1/U1754.

Technical Officer: H. W. Gandy, Tel. 202-767-3273
Security Officer: J. J. Bagley, Tel. 202-767-2391

CONTENTS

Abstract ii
Problem Status ii
Authorization ii

INTRODUCTION 1

SUMMARY OF SITE IMPLEMENTATION, INSTRUMENTATION, AND BEAM ANALYSIS 2

SUMMARY OF PROPAGATION TESTS AND ANALYSIS 4

SUMMARY OF LOW-POWER ATMOSPHERIC TRANSMISSION 6

SUMMARY OF LABORATORY STUDIES OF THERMAL BLOOMING 7

SUMMARY OF TARGET MATERIALS DAMAGE TEST AND ANALYSIS 7

SUMMARY OF HIGH-ENERGY LOADING ON MIRRORS 9

REFERENCES 10

APPENDIX A - Measurements of Vibration Characteristics of the Ground at CBD A1

APPENDIX B - Atmospheric Propagation with Thermal Blooming B1

APPENDIX C - Equilibrium Temperatures C1

APPENDIX D - Suppression of Thermal Blooming by Wind D1

APPENDIX E - Measurement of Atmospheric Meteorological Parameters E1

APPENDIX F - Atmospheric Laser Propagation Measurements F1

APPENDIX G - Beam Propagation in Air Doped with SF_6 G1

APPENDIX H - Target and Materials Damage Analysis H1

APPENDIX I - A Theoretical Study of Heat Conduction in Solids Due to Laser Radiation I1

APPENDIX J - High-Energy Loading on Mirror Devices at 10.6 μm J1

ABSTRACT
(Confidential)

This report presents the progress made at NRL in support of Advanced Development Objective (ADO) 17-54X, the High Energy Laser Program of the Navy, from the time of its initiation at the Laboratory in April 1969 through September 1969. This report includes both summary and detailed accounts of activities carried out in the three major areas of NRL responsibility: Site Implementation and Instrumentation, High-Power Propagation Test and Analysis, and Target and Materials Damage Test and Analysis.

PROBLEM STATUS

This is an interim report on the Eighth Card Program.

AUTHORIZATION

Project ORD-0832-129/173-1/U1754

NRL EIGHTH CARD PROGRAM INTERIM PROGRESS REPORT
1 MARCH 1969 TO 30 SEPTEMBER 1969
(Unclassified Title)

INTRODUCTION

(S) The Naval Research Laboratory is serving as a principal Technical Support Agent to the Surface Warfare Systems Directorate of the Naval Ordnance Systems Command (NOSC) for Advanced Development Objective (ADO) 17-54X, High Energy Laser Program. This is the Eighth Card Program of the Navy. The purpose of this program is to determine the feasibility and suitability of high-energy, high-power gas-dynamic-laser (GDL) devices as weapons in the fleet.

(S) In its role as Technical Support Agent to NOSC for this ADO, NRL has the responsibility of providing scientific and technical data relating to GDL devices and their operation in a naval environment which will aid NOSC in its evaluation and assessment of these devices as naval weapons. These support activities are being carried out under OrdTask ORD-0832-129/173-1/U 1754, Problems 1, 2, and 3.

(S) The purpose of Problem 1, Site Preparation and Instrumentation, is to plan for and prepare a suitable site for the installation, evaluation, and operation of a high-energy GDL. This activity also includes all site and range instrumentation as well as providing target sites to support this operation. Problem 2, Propagation and Damage Test and Analysis is concerned with the programmatic use of the Navy GDL. The purpose of the propagation test and analysis program is to determine and evaluate the propagation of high-power, high-energy-density radiation from GDL devices for atmospheric conditions encountered in naval environments. The purpose of the damage test and analysis program is to perform a comprehensive study on the effects of high-energy, high-power-density GDL radiation on various target materials, structures, and components and to provide the quantitative data necessary for the assessment of the effectiveness of GDL devices as naval weapons. Problem 3, Effects of High Energy Loading on Mirror Devices, is concerned with the determination of the effects of high-energy loading on mirrors and mirror structures. Effects to be considered include, but are not limited to, mirror figure, stability, and damage.

(U) This report represents the first NRL written report of progress on its Eighth Card Program activities to the program sponsor, NOSC. This report includes ONR-funded as well as NOSC-funded NRL support to the Eighth Card Program covering the time period from its initiation at NRL in March 1969 through 30 September 1969. Substantial initial research which provided a background for NOSC's requirements to establish a Navy high-energy laser program was begun by NRL personnel in June 1968 and extended to March 1969. Funding for this effort came from the Laboratory's resources and was coordinated by the NRL Laser Council. Their contributions included study group activity relating to the work of the Millburn Committee, preparation of technical summaries, and in particular the first Navy TDP on the Navy High Energy Laser Program. In addition, considerable effort was expended in formulation of plans relating to the use of NRL's Chesapeake Bay Division for a high-energy test station and in initial formulation of the site requirements.

(U) Six sections summarizing NRL activities constitute the main body of this report; more detailed technical descriptions of these activities are given in the appendixes. Since this is a progress report, some of the results given here may be modified or even substantially changed in future reports as indicated by continued study and experiment. Comments about and criticisms of this report are welcome.

SUMMARY OF SITE IMPLEMENTATION, INSTRUMENTATION, AND BEAM ANALYSIS

(C) Naval Research Laboratory personnel initiated efforts on the Eighth Card Program in June 1968, supporting NOSC's objective of acquiring a large gas dynamic laser (GDL) to be evaluated as a weapon system for use by the fleet. Factors surveyed included potential sites, the availability of technical support facilities, and access to the NRL community of scientists and engineers. Based on these studies, a proposal, NRL Secret letter 5110-70:EFK:eml SER: 00170 dated 19 March 1969, was submitted to the Chief of Naval Research (Code 108) recommending a site at NRL's Chesapeake Bay Division (CBD). Following the decision to locate a GDL here, and until the receipt of NOSC funding in April 1969, Eighth Card efforts were expanded to meet the schedule of activity required. Construction scope plans for a high-energy facility (HEF) including a three-building complex, and site layouts for support systems were developed. Surplus high-pressure-gas tankage was located, and specifications were prepared for an air compressor and for two cryogenic gas storage systems. Closely related efforts were initiated on studies of the CBD environment, safety, security, and instrumentation, and on theoretical and experimental programs. During the period June 1968 to March 1969 the Laboratory contributed approximately three man-years of effort totaling about $100,000 of ONR funds to this NOSC project. This program was undertaken by the Applied Physics Branch, NRL Code 5110, of the Applications Research Division, where a continuing effort is directed toward site implementation, instrumentation, beam analysis, and the conduct of experiments in support of the Navy's Eighth Card researchers.

(S) Meanwhile, the Navy is participating in a tri-service procurement with the AVCO Systems Division for three gas dynamic lasers expected to produce a power output of 150 kW at a wavelength of 10.6 μm. The 50-cm-diameter, focusable, highly coherent beam will have a near single-mode characteristic and a far-field spot size within twice the diffraction limit. The beam is to be stable to within 1/2 the beam diameter during a typical 15-second run. Delivery of the Navy's GDL is anticipated by June 1970. It will be installed at CBD, located about 40 miles from Washington, D.C., on the west shore of the Chesapeake Bay. This maritime environment will provide overwater paths from a cliff-edge building to a target tower on Tilghman Island about 15 km away and to floating or bottom-anchored platforms at intermediate distances. The laboratory facilities in this area are well adapted to conduct a variety of high-energy propagation and target damage tests. A test-tunnel will provide complete confinement of the beam for many of the target damage tests, and for a critical evaluation of the performance of the GDL. Instrumentation needs for amplitude, spatial, temporal, and coherence measurements will be purchased if possible, but the high energy level at this wavelength presents unusual problems which in many cases can be met only by the development of specialized equipments. Although the CBD population density and water traffic is low, an extensive safety program has been inaugurated to protect all persons and property within the entire region from accidential exposure to the laser energy and to insure that the atmospheric release of any gases will result in concentrations which remain below the allowable levels for toxicity.

(C) The high-energy facility (HEF) will consist of a 30 by 30 foot control building, a 40 by 60 foot secure reinforced-concrete building to house the GDL, a 10 by 140 foot enclosed-experiment tunnel attached to the building housing the GDL, and an existing 40 by 100 foot quonset-type building to house the high-pressure gas tank farm and air compressor, external tankage and compressors for cryogenic gas systems, and tanks for cooling water storage. The Tilghman Island Navy property comprises a 70-foot observation tower topped by an enclosed work space. A 20-foot square platform 10 feet above mean water level, positioned 5000 yards at 150 degrees (true) from the GDL building and about 1000 feet offshore, is available for planned intermediate-range propagation studies. Details of the general site configuration, safety and security provisions are described, with photographs, in Ref. 1.

(C) Architectural plans were contracted for by the Chesapeake Division of the Naval Facilities Engineering Command and completed about 1 August. Coring samples of the soil at the HEF site were obtained to determine soil stability characteristics. The Ocean Structures Branch of the Ocean Technology Division has contributed consultative services through studies of the potential shock and vibration environment and its influence on the beam pointing stability of the GDL. Vibration tests of the soil at the GDL site were conducted through the cooperation of the Naval Ship Research and Development Center. Appendix A and Refs. 2 through 11 are a series of reports on these efforts.

(C) To avoid dividing GDL beam performance responsibility, NRL asked that AVCO's contract be extended to cover preparing the specification for the GDL supporting system. On 1 July 1969 AVCO submitted the final design consisting of three concrete-base pads independently supported by rubber isolators resting on a large concrete mat which underlies the entire GDL. Negotiations are now in progress to have AVCO contract for the construction of the supporting system using their plans.

(U) The Chemistry Division has undertaken a study regarding the hazards involved in storing carbon monoxide at high pressure. (Carbon monoxide serves as the major fuel which, when burned, generates the carbon dioxide fundamental to the laser operation.) Under some conditions it has been reported that iron and nickel carbonyls may be formed causing problems due to high toxicity and to stress corrosion of storage tanks with resultant weakening. Interim reports, Refs. 12 and 13, review the results of conferences with industrial users, and of laboratory reports. Present indications are that CO can safely be stored at 2200 psi.

(C) Safety considerations are receiving extensive study. Cooperation has been extended to NOSC and NWL personnel in their safety review of the Eighth Card Program. Problems of handling high-pressure, toxic, explosive gases, and provisions for suitable sensors and alarms are under continuing evaluation. A surveillance system has been designed to give complete assurance that no hazard will threaten either the project personnel, any unwary individuals, or any property throughout the external propagation range. Refractory and ablative, nonspecular materials have been examined for beam containment at the target site. Consultations with the Air Force, the Army, AVCO, and United Aircraft Laboratory are continuing, to insure a maximum of safe operating conditions for site personnel and for the community.

(C) Theoretical and experimental beam analyses have been undertaken to determine the optimum energy distribution across the GDL output aperture with the objective of achieving a maximum on-axis intensity at the far-field target site, while minimizing side lobes. An interim report, Ref. 14, indicates that a Bessel function distribution may be superior to the truncated Gaussian.

(C) Beam instrumentation studies have considered the equipment designs needed to study the amplitude, spatial, temporal and coherence characteristics at the GDL, in the near-field test tunnel, and at remote target sites. Imaging scanners and direct receptor arrays must be designed to accommodate the exceptional power levels and the amplitude bandwidths expected. A survey report is presented in Ref. 15.

(U) Additional progress reports and consultative services reports are included in Refs. 16 through 22.

(C) The reductions in the funding which had been programmed will soon adversely affect NRL's ability to initiate procurements which are vital to meeting the Navy's obligations to provide significant support elements essential to the completion of a functioning GDL. Major items affected include the cryogenic gas storage and compressor systems for nitrogen and carbon monoxide, the contracting for the supplying of liquid N_2 and CO and of gaseous oxygen and methane, the refurbishing of surplus gas tankage, the construction of the supporting system for external high-pressure gas lines and control cables, the construction of the foundation for the air compressor and the subsequent installation services, the procurement and installation of toxic-gas sensing and alarm system, the procurement and installation of the television and communication safety surveillance system, the installation of the surveillance radars and indicators, and the procurement of instrumentation for beam diagnostics and target damage effects at local and remote stations.

SUMMARY OF PROPAGATION TESTS AND ANALYSIS

Purposes and Plan

(C) Work in the category of Propagation Test and Analysis can be considered as taking place in two phases. The second phase will include a program of high-power atmospheric propagation tests carried out with the Navy GDL at CBD under differing meteorological conditions. Because of the expected complex interactions of the high-energy, high-power beams with the maritime atmosphere, and because of the high expense of performing GDL tests and the low rate of field testing (six to eight runs per day at best), it is desirable to develop a carefully-laid-out test program for the efficient and meaningful utilization of the Navy GDL. The purpose of the first phase of the propagation effort is to develop this test program prior to the initiation of GDL field testing, which is presently expected in the second or third quarter of FY-1971.

(C) Three areas of activity are being carried out during the first phase: Theoretical Studies of High Energy and High Power Laser Beam Propagation, Studies of Low Power Atmospheric Transmission, and Laboratory Studies of Thermal Blooming of Laser Beams in Gases.

(C) The purpose of the theoretical study is to develop models for the interaction of high-energy, high-power optical beams with the atmosphere which will (a) predict the spatial and temporal characteristics of these beams when focused and unfocused to serve as a basis for test program planning, (b) provide the baseline information against which field tests may be compared and studied, and (c) provide information to be used for instrumenting the optical range and planning the reduction of data.

(C) The purpose of the low-power atmospheric transmission studies is to quantitatively study the effect atmospheric turbulence has on the propagation of laser beams,

both in the visible and at 10.6 micrometers. The results of these studies can be used in determining realistically the pointing and training requirements and specifications for high-energy laser systems as well as providing a needed quantitative input to the theoretical propagation effort.

(U) The purpose of the laboratory study of thermal blooming is to study quantitatively thermal defocusing of CO_2 laser beams in static and flowing gases of controlled compositions and with controlled additions of water vapor and other absorbing gases. The results of these studies will be used by the propagation theory program.

Propagation Theory

(C) In about the middle of the reporting period, Dr. H. B. Rosenstock, NRL Code 6404, was designated as head of the propagation theory group, which consists of personnel from the Optical Sciences, Solid State, Nuclear Physics, and Applications Research Divisions with consultive support being given from the Plasma Physics and Ocean Sciences Divisions. During the earlier part of this period, the theory group became familiar with the status of the field in general and considered those propagation problems directly related to the operation of the Navy GDL as well as to more general long-range problems. The problems of interest may be generally classified as linear or nonlinear. In the linear case, the effect under consideration is proportional to the power density P^n of the optical beam with n equal to 1, whereas in the nonlinear case, the effects are proportional to P^n with n greater than 1.* The linear problems include such things as direct optical absorption by atmospheric gases, scattering by aerosol particles, and atmospheric turbulence. These effects represent losses which are proportional to the optical beam power density and may at least in principle be compensated for by using higher beam powers. On the other hand, the so-called nonlinear problems increase in importance with beam power by a power higher than 1 and can therefore lead to absolute limits to the propagation possibilities, uncompensable by higher power levels. These propagation problems include: the modification of atmospheric properties by the beam itself (blooming, or the negative lens effect), heating and cooling on account of wind, induced atmospheric instabilities, multiple quantum absorption, stimulated inelastic scattering, and other effects commonly referred to as true nonlinear optical effects.

(U) During the reporting period, one NRL Report has been prepared, and several informal preliminary reports have been completed. The NRL Report is included here as Appendix B. The preliminary reports now being circulated internally are: J.W. Tucker, "Diffraction Limitations"; J.W. Tucker, "Bending Effects of Wind"; J.N. Hayes, "Short-Time Thermal Defocusing of Laser Beams"; W.R. Faust, "Equilibrium Temperatures"; and H.B. Rosenstock, "Suppression of Blooming by Wind"; the last two of these are included as Appendixes C and D.

---

*(C) The term "nonlinear" as used here differs from conventional usage of this term in Nonlinear Optics and Quantum Optics. The accepted meaning of nonlinear in these fields indicates that an effect is proportional to a higher power of the optical dielectric constant of the propagating medium. Typically, these nonlinear effects occur at optical power densities much higher than those that are presently under consideration for Navy GDL field testing. In an attempt to relieve this ambiguity, it has been suggested tentatively that for the present usage, the terms "linear" and "nonlinear" be replaced by "power independent" and "power dependent."

(U) Most of the reports here deal with the phenomenon of thermal blooming. The one by DeWitt and Tucker (Appendix B) considers the transient case, as does the one by Hayes, which is limited to short times. Both assume absence of turbulence and of both free and forced convection but used different models for the hydrodynamics of the atmosphere. The same assumption of a quiet, nonturbulent atmosphere in the absence of wind is made by Faust's manuscript (Appendix C), which obtains a maximum temperature rise of 24°C under such conditions. The steady state estimate of an 0.004°C temperature rise obtained by Rosenstock (Appendix D) is based on the presence of wind, which will cause any given volume of air to be heated for only a short time. Rosenstock's report predicts that thermal blooming is essentially negligible under expected conditions—in the open air in a naval environment.* By comparison, it would seem that the so-called linear effects may be of comparable practical importance, vis-a-vis thermal blooming. This tentative conclusion should be considered at present as a moot question because the work done so far in this field has not modeled the maritime atmosphere realistically; this is certainly to be expected because of the mathematical complexity of the practical problem.

(C) Linear effects such as turbulence and aerosol scattering should be considered at low optical beam power densities and then at increasing densities. It is of some practical interest to ascertain whether or not a threshold exists for the transition of lamellar flow of optical energy through the atmosphere to what may be considered as a turbulent mode of atmospheric propagation in which small disturbances in the beam would tend to be amplified.

(U) It should be clear from the preceding that even though the Eighth Card Program is classed as Advanced Development, much of the work in atmospheric propagation falls into the Exploratory Development and Basic Research categories. With this in mind, the program plans in the theoretical effort will be determined and paced by the understanding of and insight into the real-world problem as work progresses.

SUMMARY OF LOW-POWER ATMOSPHERIC TRANSMISSION

(U) All of the work in the category of low-power atmospheric transmission is being carried out by personnel of the Infrared Branch (NRL Code 6530) of the Optical Sciences Division. The principal objective of this effort is to experimentally determine the effects of turbulence in a maritime atmosphere on the radiant energy and phase distribution of a low-energy CO_2 laser beam. During the early part of this work visible lasers are being used to provide familiarity with the general character of the effects caused by turbulence and to develop experimental methods for the CO_2 wavelengths where suitable imaging methods are not available at present. Initial propagation measurements using an overland path have been made, but soon overwater studies will begin. One difficulty in making overwater measurements is monitoring the requisite meteorological parameters for such paths. To this end a J-boat (a 40-foot launch) is being equipped with suitable temperature and humidity monitoring apparatus. In addition, a sensitive, fast-response thermometer system is being checked out, which will be used for a nonoptical determination of atmospheric turbulence along the paths being used for laser propagation studies.

*This view appears to be in accord with conclusion more gradually and cautiously reached by other groups outside NRL, who, after considerable work on the subject of blooming, have recently reported results at an ARPA sponsored meeting in Lexington, Massachusetts (15-16 October 1969).

(U) Preliminary measurements of atmospheric meteorological parameters have been made over several overwater optical ranges at CBD. Some of the preliminary results of overwater variations in atmospheric temperature and humidity may be found in Appendix E. A discussion of the experimental methods used and planned improvements is also included. Following equipment improvements, data needs to be obtained for a variety of weather conditions.

(U) An overland propagation test range has been set up at CBD to make a preliminary study of the effects of atmospheric turbulence on laser beam transmission and to develop and prove optical and electronic methods and techniques that will later be employed in measurements on over-the-water optical ranges. The preliminary measurements made on this range have been concerned with the amplitude and frequency statistics of time-varying signals using a helium-neon laser ($\lambda = 0.633$ μm) as the transmitting source. A detailed discussion of the experimental methods used, some of the preliminary data obtained and its analysis, and plans for future work may be found in Appendix F.

SUMMARY OF LABORATORY STUDIES OF THERMAL BLOOMING

(C) All of the laboratory studies of thermal blooming are being carried out by personnel in the Plasma Physics Division. This work has been in progress for about 2-1/2 years. Work prior to the start of the Eighth Card program at NRL was concerned with thermal defocusing of visible laser radiation in passing through doped liquids. These studies indicated that if the blooming experiments could be carried out with experimental conditions which corresponded to the assumptions that were made in the theoretical treatment of the problem, then the experimental results do agree with the theory.

(U) Similar work has been carried out recently in air doped with sulfur hexafluoride gas using CO_2 laser beams at a wavelength of 10.6 μm (Appendix G). In this case also, preliminary results indicate that if experimental conditions are tailored to fit the assumptions of the theory which is being used to interpret the experiments, then the experiments do agree with the theory. This conclusion should only be considered valid for the levels of power absorption by the gas mixtures that have been used in the experiments thus far. Nevertheless, it does tend to give confidence in the use of theory to predict propagation characteristics in more complex environmental conditions. Clearly experiments must be carried out at higher power levels.

(U) Experiments of the type described here are planned using nitrogen-carbon dioxide mixtures with controllable amounts of water vapor introduced into the mixture. It is hoped that these experiments will yield some realistic insight of the effect of humidity on the temporal and spatial defocusing characteristics of laser beams in atmospheric gas mixtures.

SUMMARY OF TARGET AND MATERIALS DAMAGE TEST AND ANALYSIS

(S) The effort in damage test and analysis has been divided into two phases for essentially the same reasons as was mentioned earlier for the propagation program. The second phase of this program will involve studying target damage using the Navy GDL in the tunnel at CBD which is presently expected to be initiated in FY-1971. Again for reasons of expense of GDL operation and rate of experimentation, it is

necessary to carefully plan for the most efficient and meaningful use of the GDL. This is the purpose of the first phase of this work.

(S) Theoretical as well as experimental damage studies will be used as the basis for planning the materials and damage test schedule for the Navy GDL. The experimental threat analysis and damage test and failure diagnostics program are expected to provide target vulnerability information as well as quantitative input data to update and refine the theoretical models. For the power density levels and wavelengths of the CO_2 GDL radiation, it is expected that the important damage mechanism will be predominantly thermal in character and will involve melting, burning, charring, vaporization, thermal fracture, thermally induced rupture of highly stressed materials, and possibly other thermal phenomena depending on target materials, construction methods of the target structure, and the environment. In the theoretical damage studies, the spatial and temporal temperature and stress distributions in a material are being calculated as a function of incident optical power density and angle. These studies will include material parameter variations with such things as material-temperature and simulated environmental conditions. The aim of the initial laboratory materials damage program will be to determine quantitatively the conditions of material failure under carefully controlled laboratory conditions which simulate expected environmental conditions. The failure diagnostics program will study the macroscopic as well as microscopic changes in target materials of interest caused by high-energy doses of laser radiation. Information from both of these programs will be incorporated in the theoretical damage program so that meaningful calculations may be scaled to predict the conditions of failure in larger, more complex target structures.

(S) The experimental damage studies will examine materials such as metals and alloys, ceramics including refractory materials, optical materials, sensor materials, ablative materials, and organic dielectric materials. It should be noted that information derived from the damage test and analysis should be most useful in formulating technical countermeasures to GDL radiation attack.

(U) During late summer, Dr. C.C. Klick, NRL Code 6400, was designated to head the materials damage test and analysis in this program. This includes both the theoretical and experimental efforts.

(S) A detailed quantitative understanding of target materials damage effects is as important to the design specifications of an effective naval weapon system as is a detailed understanding of high-power optical propagation effects in a maritime atmosphere. This provides needed supportive information to the determination of target mission abort criteria, duration of irradiation, etc., and hence to the sizing and operational doctrine of such a system. Most of the work carried out in this area thus far must be considered exploratory and is indicative of general effects only. It is important to determine when damage theory and calculations are reliable and when they are not. It is important to understand the different damage mechanism in different types of materials so that they may be more intelligently exploited. In a practical sense, combined effects involving the environment as well as the physical and chemical character of targets should be expected and must ultimately be understood on a quantitative basis.

(C) When considering all the types of materials that should be examined for quantitative damage characteristics in support of this program, different uses of materials in target systems must be considered, such as structural, optical, sensor, guidance, command, control, and countermeasures. Even a preliminary analysis of this partial list indicates that a rather substantial number of materials can be listed for quantitative

laboratory investigation. In the interest of assigning priorities for the experimental effort as well as not overlooking any materials for consideration, the following approach was selected.

(S) A list of all the possible targets for naval GDL radiation attack that could be identified at present was made. A preliminary technical analysis of these targets is being carried out to evaluate the target technical characteristics relevant to optical radiation attack. This technical "threat analysis" is helpful in determining the most vulnerable areas of each target and in identifying those knowledge deficiencies regarding materials damage that occur most frequently in the spectrum of GDL targets. This information is being used now and will continue to be used as a basis for planning and executing as complete and as responsive a laboratory materials damage program as is possible under present budgetary restrictions. A more detailed description of this process is given in Appendix H.

(C) Thermal damage in materials is also being studied theoretically. The problem of the heating of a material due to irradiation by intense laser beams is considered in a classical treatment using blackbody reradiation at the surface as the preliminary boundary conditions, and assuming constant thermal parameters (Appendix I). While this treatment is somewhat idealized, as shown in detailed treatment in Appendix I, it is of some practical value in making estimates of such things as the time required to cause surface melting for a given material with a given optical power distribution incident upon the material. Future work will generalize this thermal-damage treatment to more closely model anticipated test conditions. This future work will include temperature-dependent thermal parameters, and surface considerations will include convection and ablation as well as reradiation.

SUMMARY OF HIGH-ENERGY LOADING ON MIRRORS

(S) Several mirrors in beam-folding optics are included in the current design of the tri-service laser to be delivered to NRL. The rated reflectance of the individual mirrors is 99.2 to 99.5 percent. The part which is not reflected is absorbed in the mirror, and the resulting heat may cause mirror image distortion, instabilities, and reduction of beam output quality. Many techniques such as using maximum allowable mirror diameters, water cooling, and a low-temperature-coefficient base supporting the mirror structure may be used to minimize the effect on mirror integrity and beam quality.

(S) Because of the high power output (nominally 150 kW) generated by the GDL, any improvement in reducing the mirror absorptance will significantly reduce mirror loading and damage. The studies at NRL have been directed toward mirror design as affected by design complexity, size, mirror support systems, and reflective film coatings capable of reducing mirror absorptance by orders of magnitude. New techniques for measuring actual mirror absorptance have been developed. These experimental and theoretical aspects are discussed in Appendix J. This work was done in the Optical Sciences Division, Applied Optics Branch, and is currently not being supported because of the shortage of funds.

REFERENCES (U)

1. "Site Preparation," Memorandum 5110-100:DJM:eml of 7 May 1969 by D. J. McLaughlin

2. "Explore Equipment Availability at NSRDC for Shaking a Foundation of a Building," CSR 9H40 dated 25 Apr. 1969 by Code 8441

3. "Inspect Equipment Available at NSRDC for Shaking Foundation of a Building," CSR 9H42 dated 28 Apr. 1969 by Code 8441

4. "Explore Cooperative Arrangements Between NRL and NSRDC for Vibration Testing of a Building Foundation at the Chesapeake Bay Division of NRL," CSR 9J01 dated 16 May 1969 by Code 8441

5. "Discuss Redesigned Foundation, View Core Samples, and Sight Ground Pistons for Proposed Vibration Tests of Building Foundation at Chesapeake Bay Division," CSR 9K22 dated 6 June 1969 by Code 8441

6. "Obtain Latest Information on Foundations for Building at Chesapeake Bay Division," CSR 9K39 dated 13 June 1969 by Code 8441

7. "Examine Site for Proposed Vibration Tests and Make Preliminary Plans," CSR 9L81 dated 24 June 1969 by Code 8441

8. "Determine Latest Progress in Vibration Tests at Building Site at Chesapeak Bay Division," CSR 9M56 dated 7 July 1969 by Code 8441

9. "Discuss Change in Plans for Shaker to be Used in Vibration Test of Building Site at CBD," CSR 9M57 dated 8 July 1969 by Code 8441

10. "Report Latest Progress in Vibration Tests of Building Site at CBD," CSR 9M58 dated 11 July 1969 by Code 8441

11. "Check Status of NSRDC in Participation in Tests of Ground Vibration at CBD," CSR 9099 dated 11 Aug. 1969 by Code 8441

12. "Trip Report (C.T. Ewing to United Aircraft Corp., Pratt and Whitney, FRDC, West Palm Beach, Fla.)," from Code 6130 to Code 5110; 6130-247:CTE:cmc dated 8 Sept. 1969

13. "High Pressure Storage of Carbon Monoxide," Memorandum 6130-254:CTE:cmc dated 17 Sept. 1969 to Code 5110

14. "Intensity Distributions in Truncated Laser Beams of Near-Gaussian Form," NRL Memorandum Report by M. DeLong (in preparation)

15. "High Energy Laser Beam Monitoring," by F. R. Fluhr, Memorandum for File (in preparation)

16. "NRL Eighth Card Program Status – May 1969," Memorandum 5110-112A:EFK:eml dated 5 June 1969

17. "To Present AVCO's Eighth Card Support Design," CSR 5110-145:DJM:eml dated 11 Aug. 1969

18. "To Review Delivery Schedule of Eighth Card TSL Components to CBD and Establish Support Requirements," CSR 5110-144:DJM:eml date 11 Aug. 1969

19. "To Discuss Eighth Card Supports," CSR 5110-143:DJM:eml dated 11 Aug. 1969

20. "To Discuss Eighth Card Support and Accessory Components," CSR 5110-148:DJM: kag dated 13 Aug. 1969

21. "Progress Report – Eighth Card," 5110-147:EFK:kag dated 20 Aug. 1969

22. "Discuss CBD HEF Facility," CSR 5110-151:CJK:eml dated 29 Aug. 1969

Appendix A

NRL Memorandum Report 2033

Measurements of Vibration Characteristics of the Ground at the Chesapeake Bay Division of the Naval Research Laboratory

R. L. BORT

Ocean Structures Branch
Ocean Technology Division

August 1969

NAVAL RESEARCH LABORATORY
Washington, D.C.

CONTENTS

Abstract	ii
Problem Status	ii
Authorization	ii
LIST OF TABLES	iii
LIST OF FIGURES	iii
INTRODUCTION	1
TEST PREPARATIONS	2
INSTRUMENTATION	4
TEST RESULTS	6
ANALYSIS	9
DISCUSSION	11
ESTIMATES FOR BUILDING FOUNDATION	15
SUMMARY AND CONCLUSIONS	18
ACKNOWLEDGMENTS	19
REFERENCES	20

ABSTRACT

Vibration measurements were made at the site of a building which is to be constructed at the Chesapeake Bay Division, three miles south of Chesapeake Beach, Maryland. A rotating mass vibration generator was used to apply vertical oscillating forces with amplitudes 0.3 to 22 kilonewtons at frequencies 3 to 33 Hz to a circular steel plate 1.8 meters in diameter placed on the surface of the ground. The plate and vibration generator had a mass of 4 metric tons. It was found that the ground behaved nearly as a linear medium over the range of forces and frequencies tested and supported the equipment with a natural frequency of 25 Hz and damping 12 percent of critical near resonance. Damping was variable and decreased appreciably after a rainstorm at the site. Ground waves transmitted away from the plate at 20 Hz appeared to have a phase velocity of 132 meters per second near the ground surface but the velocity increased to 266 meters per second at a depth of 9 meters. Data from the measurements are presented and a procedure is given for scaling the data to obtain estimates of entrained mass of soil, stiffness, and damping for vertical vibrations of a reinforced-concrete mat placed onto the ground at the test site.

PROBLEM STATUS

This is an interim report on one phase of a problem. Work on other phases continues.

AUTHORIZATION

The present work was conducted under NRL Problem F02-18, and R05-31, and represents special consultation on vibration problems done by the Ocean Technology Division, Ocean Structures Branch at the request of the Applications Research Division, Applied Physics Branch. Project Number for this report is RR 009-03-45-5757.

List of Tables

		Page
1.	Locations of Transducers	21
2.	Test Runs Conducted	22
3.	Acceleration Amplitudes Read from Oscillograms	23
4.	Acceleration Phases Read from Oscillograms	24
5.	Ground Motions at Different Distances from the Ground Piston	25
6.	Vertical Motions of the Center of the Ground Piston	26

List of Figures

1.	Test Site at the Chesapeake Bay Division	27
2.	Vibration generator and ground piston	28
3.	Typical record.	29
4.	Resonance curve for vertical response of the ground piston	30
5.	Apparent mass.	31
6.	Apparent stiffness.	32
7.	Apparent damping on July 18.	33
8.	Apparent damping on July 22.	34
9.	Acceleration amplitudes at the ground surface along a line extending south from the ground piston.	35
10.	Phase shifts for 20-Hz waves transmitted away from the ground piston.	36
11.	Rotations of the ground piston about horizontal axes.	37

INTRODUCTION

The Ocean Structures Branch of the Ocean Technology Division was asked by the Applied Physics Branch of the Applications Research Division to supply consultative services concerning vibration characteristics of foundations to be installed in a building planned for the Chesapeake Bay Division of the Naval Research Laboratory. The proposed building was to be located at a site 30 meters north of existing Building 5 at the Chesapeake Bay Division and there was some concern that the soft and sandy soil at the site would lead to problems of unacceptable vibrations of foundations within the building.

The tests reported here were planned to produce data directed toward the following questions:

1. Can the soil beneath a concrete mat laid on the ground at the building site be represented by equivalent values of mass, stiffness, and damping? If so, what values would be appropriate for particular mats under particular conditions?

2. Is the subsurface ground structure such that there are likely to be strong reflections or standing waves associated with layers of different soils at the building site?

3. Are vibrations transmitted through the soil from or to the proposed building likely to be troublesome?

Measurements were made by mounting a rotating-mass vibration generator atop a circular steel plate placed on the ground surface at the building site and monitoring motions of the plate and of the ground surface with accelerometers. This report describes the tests conducted and gives the results of an analysis of oscillographically-recorded data from the tests.

TEST PREPARATIONS

Ground Piston

The ground piston consisted of a circular steel plate 5.5 inches thick (140 millimeters) with a nominal mass of 5500 pounds (2.5 metric tons). The bottom of the piston had a diameter of 71.5 inches (1.82 meters) measured to the outside of a flange. The lowest natural frequency which could be calculated for the piston was 210 Hz, obtained by considering it as a thin circular plate fixed at its center.

Placement of Ground Piston

A spot was leveled on sloping ground 30 meters north of Building 5 at the Chesapeake Bay Division and the piston was laid flat onto undisturbed soil at the bottom of the shallow excavation. The test site was located midway between two test borings 11 meters apart which were said to mark two points on the foundation for the proposed building. The piston was placed on dry soil **2 July 1969** and there was no rain at the test site from that day until after the first series of tests were conducted on July 18. Figure 1 is a photograph of the test area.

Vibration Generator

The TMB 5000 Pound Three-Mass Vibration Generator was used to apply forces to the ground piston. The generator contains three rotating masses of 200 pounds each (91 kilograms) which may be adjusted to place their centers of mass at eccentricities up to 3.5 inches (89 millimeters) from their centers of rotation. Shafts supporting the masses are geared together so that the center mass rotates in one direction while the two outer masses rotate in the opposite direction. No provisions are made for measuring the forces generated; forces are regularly calculated from the values of mass, eccentricity, and speed of rotation. Reference 1 describes the vibration generator used and gives instructions for its use, together with formulas for calculating forces. The generator was used in accordance with the instructions of Ref. 1.

Placement of Vibration Generator

The vibration generator was supplied mounted to a steel plate, with its electric drive motor mounted above the generator on a four-legged stand attached to the plate. The generator was placed atop the ground piston with its long axis aligned approximately northeast-southwest and with the shafts for the rotating masses aligned southeast-northwest. It was held in place by welding the steel plate to the top of the ground piston. Shafts for the rotating masses were 0.43 meters above the bottom of the ground piston. The center mass was over the center of the ground piston and the two outer masses

were 0.51 meters northeast and southwest of the center. Figure 2 shows the vibration generator in place on the ground piston. Mass of the vibration generator (2100 pounds), drive motor (600 pounds), steel plate, and mounting stand was about 1.4 metric tons.

INSTRUMENTATION

Transducers

Transducers were Kistler Servo Accelerometers Model 305T, range 50 g maximum, with sensitivities standardized to 0.20 milliamperes per g. Seven accelerometers were mounted on the ground piston at the locations shown in Table 1. Each accelerometer was screwed to an aluminum mounting pad 40 by 40 by 13 millimeters using Kistler adapters Part Numbers 300-1 or 300-2, and the pad was fastened to the ground piston with Hysol Epoxi-Patch from Hysol Kit Number 309. Three other accelerometers (Table 1) were screwed to a steel block 40 millimeters cube which could be moved about to measure accelerations at selected locations.

Amplifiers

Each accelerometer was connected to a matched Kistler Model 515T Servo Amplifier through a cable about 32 meters long. Signals from the servo amplifiers were further amplified by a 14-channel DTMB Type 514-1A Accelerometer Amplifier in which each channel had a switch-selectable gain of 1, 10, or 100.

Recorders

Signals from the DTMB amplifiers were recorded by a Consolidated Electrodynamics Corporation Recording Oscillograph 5-119 equipped with Type 7-123 galvanometers. Signals were also recorded by a 14-channel tape recorder in a format compatible with analysis equipment on hand at the Naval Ship Research and Development Center.

Calibration

A pushbutton on each Kistler amplifier produced a signal equivalent to a step acceleration of -1.0 gravities. These signals were recorded on the oscillograph with gain settings of unity. Subsequent acceleration records were scaled to these signals with allowance for the settings of gain switches on each Kistler and DTMB amplifier. Settings of the twenty gain switches were recorded manually for each run. An oscillator monitored by a Ballantine voltmeter was used to inject a calibration signal at 20 Hz with peak-to-peak amplitude representing 1.0 gravity and this signal was recorded on the oscillograph and tape. This calibration signal was supplied to accommodate the analysis equipment at the Naval Ship Research and Development Center.

Phase and Frequency

A phase reference was supplied by an electromagnetic pickup which was mounted on the vibration generator to produce a spike of signal whenever a nail taped to the shaft of the vibration generator passed by the pickup.

The nail was placed on the shaft so that the spike occurred when all three rotating masses were at the top of their travel, and thus marked the time of maximum upward force. Frequency was measured in revolutions per minute by an electronic counter which counted pulses per second from a 60-pulse-per-turn generator attached to the drive motor of the vibration generator.

TEST RESULTS

Records for All Runs

Twenty-three runs are listed in Table 2. The runs are numbered in the order in which they were conducted. A tape recording with duration at least 2 minutes was made of each run (identified by run number in a voice announcement on the tape) and an oscillographic recording with duration about 10 seconds was made at some time during the tape-recorded portion of the run.

Runs on July 18

Runs 1 through 10 were made July 18, 1969. It was necessary to operate the vibration generator for about 30 minutes, at frequencies up to 20 Hz, during instrument check-out prior to conducting Run 1. The data from Runs 1 through 4 (frequencies 5 to 20 Hz) thus do not represent initial vibration tests applied to a virgin sample of soil. After Run 1, successive runs proceeded at 5-minute intervals except between Runs 6 and 7, when the vibration generator was shut down for about 20 minutes. The weather was hot and dry, and there had been no rain for more than two weeks.

Runs on July 22

Runs 11 through 23 were made July 22, 1969. No instrument check-out was needed and Run 11 was obtained during the first five minutes of operation of the vibration generator. Successive runs proceeded at 5-minute intervals except between Runs 13 and 14, when the generator was shut down for about one hour to allow a change in the eccentricity settings of the masses, and between Runs 21 and 22, when the generator was shut down for about 25 minutes. The weather was warm and moist, and a rain gage near the test site indicated that there had been about an inch of rainfall. There was some standing water in the shallow excavation in which the ground piston was mounted before the tests began, but the water had disappeared before Run 11 was conducted.

Data from Oscillograms

Amplitudes and phases of accelerations read from the oscillographic records from Runs 1 through 23 are shown in Tables 3 and 4. Tracings from the test oscillograph record are shown in Fig. 3. Note from the tracing that the signals from the ground piston include both harmonic and subharmonic distortion, and that they are also affected by machinery noise and ringing which is not harmonically related to the vibration frequency. The data in Tables 3 and 4 were obtained from a single selected cycle of response on the oscillographic records and represent an attempt to estimate visually the amplitude and phase of a particular component of a signal which includes appreciable amounts of harmonic, subharmonic, and anharmonic distortion.

Correction for Amplifier Characteristics

The DTMB amplifiers, which were not direct-coupled, converted the calibration step provided by the Kistler amplifiers into an initial step followed by decay with time constant 0.18 seconds. Gains calculated from this decay time range from 0.96 at 3 Hz to substantially 1.00 for 10 Hz and above. Phase shifts range from -16 degrees at 3 Hz to -2 degrees at 33 Hz. All of the data in Tables 3 and 4 have been corrected for the calculated gains and phase shifts of the DTMB amplifiers.

Sweep Record

Run 10 consisted of a manually-controlled sweep from a frequency of 5 Hz to 33 Hz. The oscillogram for this run was inspected to locate possible resonant peaks in response occurring between the test frequencies used for the other runs. None were found. Resolution of the oscillogram for this run was low because gain settings of the amplifiers had to be chosen to accommodate the largest accelerations expected at any frequency.

Traffic-Noise Record

A record was taken on July 22, shortly before Run 11, of signals from the accelerometers as a heavy automobile (a 1966 Bonneville convertible) was driven north at 15 miles per hour along a road which was located about 20 meters to the west of the test site. Bursts of motion with accelerations up to 22 milligravities were noted at the ground piston and 4.6 milligravities at the floor of Building 5. These accelerations correspond to earthquakes of Scale VII ("Very strong") and Scale V ("Rather strong"), respectively, on the obsolete Cancani dynamic intensity scale*. Both maxima were in the vertical direction. Motions of the ground piston included a strong component of rocking about an axis to the southeast, with predominant frequencies estimated in the range 15 to 21 Hz. Vertical accelerations in Building 5 were at a predominant frequency of 30 Hz. The bursts of motion seemed to be associated with passage of the automobile over chuckholes in the road surface. The motions noted above came from a particular chuckhole located west-southwest of the ground piston, according to rough triangulation from arrival times at the ground piston and Building 5.

Ground-Transmission Records

A set of 12 recordings was made on the oscillograph only during Run 13 (20 Hz) as the accelerometers at Positions 8, 9, and 10 were held or placed against the ground surface at different distances from the ground piston. Data read from these 12 records were summarized in Table 5.

*This scale is historically coupled to numerical accelerations.

Motion of Vibration Generator

Accelerations at the top of the electric drive motor mounted over the vibration generator were measured during Run 13 by holding the steel block to which accelerometers at Positions 8, 9, and 10 were attached, in contact with the outer case of the drive motor. Oscillograph records were read to obtain the estimated amplitude and phase of the 20-Hz component of the acceleration signal, in the same way as the other records were read. Position 8 (up) had amplitude 58 milligravities at phase 227 degrees relative to the upward force. Position 9 (northeast) had 33 milligravities at 263 degrees. Position 10 (southeast) had 6 milligravities at 118 degrees.

ANALYSIS

Vertical Responses of the Ground Piston

Data from the four accelerometers which measured vertical motions of the ground piston were combined in a weighted average to obtain the vertical motion at the center of the ground piston. Average motions are listed in Table 6. The data from Table 6 have been plotted in different ways in Figs. 4 through 8. Each figure includes a calculated curve based on a simple assumption which may be compared with the plotted data.

Transmission of Waves Along the Ground Surface

Data on vertical amplitudes and phases of motions at the ground surface taken from Table 5 have been plotted in Figs. 9 and 10. The phase data in Fig. 10 have been fitted to an arrival-time curve based on an assumption that the speed of the waves varied linearly with depth in the ground. The best-fit linear variation was then used to calculate wave amplitudes for a spherically-symmetric source and the resultant variation in vertical motion of the ground surface with distance has been plotted in Fig. 9.

Check of Precision of the Data

The four accelerometers which measured vertical motion of the ground piston gave an overdetermined representation of the three applicable rigid-body motions of the ground piston (vertical translation, rotational motions about two horizontal axes). If the data were perfectly accurate and the ground piston were perfectly rigid, it would be possible to combine the data from the four accelerometers to show that no accelerometer moved out of the plane established by the other three accelerometers. A check of consistency of the data was made by estimating the motion of the center of the ground piston using data from Positions 1 and 3 only, or data from Positions 2 and 4 only, and comparing the estimate with that obtained from all four positions (Table 6). Such a check covers all aspects of the precision of the data (comparative calibrations among the accelerometers, relative gains of the amplifiers, reading of amplitudes and phases from the records, and so on) but cannot confirm the absolute accuracy of the data.

Precision of Amplitude Measurements

A check of the amplitude errors in Table 6 using the method described above showed that the median of the absolute values of the errors was 11 percent for Runs 2 through 9 and 25 percent for runs 11 through 23. The larger error for the later runs was the result of a consistent difference between amplitudes of average

motions at Positions 1 and 3 compared to Positions 2 and 4. During Runs 13, 17, and 19 through 22 the amplitudes from Positions 1 and 3 averaged 52 percent higher than the amplitudes from Positions 2 and 4. Data for these runs shown in Table 3 suggest that the difference occurred because the amplitudes at Position 3 were read and scaled as having nearly twice the values of the amplitudes at Positions 1, 2, and 4. A careful recheck of the calibration values and of the 48 values of attenuator settings logged for these four positions and six runs has failed to suggest any explanation for the consistent error.

Precision of Phase Measurements

A check of the phase errors in Table 6 using the method described above showed that the median of the absolute values of the errors was 8 degrees for all runs.

Rotational Motions of the Ground Piston

Figure 11 shows rotational motions of the ground piston calculated from the difference between the motions at Positions 1 and 3 (for rotations about an axis to the southeast) and the difference between the motions at Positions 2 and 4(for rotations about an axis to the northeast).

Additional Analyses

The preceding analyses were based entirely on the oscillographic records from the test. Each recorded value is based on a visual reading made from a single cycle of response chosen as typical. Tape recordings of the data from Runs 1 through 23 are in a format acceptable to automatic analysis equipment on hand at the Naval Ship Research and Development Center. The analysis equipment can perform repeated analyses of tape loops and can average the data over many cycles of response. The tape is presently in the custody of William E. Leyda and Irvin L. Young of the Naval Ship Research and Development Center, and can be analyzed by them as directed.

DISCUSSION

Linearity

In Fig. 4 the data on vertical motions for all runs have been plotted as if they had been obtained from a linear system. The data have been fitted with a resonance curve calculated for a mass of 4 tons mounted on a linear spring with stiffness 100 kilonewtons per millimeter and viscous damping 150 kilonewton-seconds per meter. The graph suggests that there is no consistent difference between the data from Runs 2 through 13 and the data from Runs 14 through 23, although the latter runs involved force amplitudes ten times the force amplitudes for the earlier runs. It may be concluded that the ground behaved approximately as a linear system over the range of forces and frequencies tested. The calculated linear resonance curve seems appropriate except that it tends to be low in the range from 10 Hz to 20 Hz and does not account for the single data point at 3 Hz.

Mass

The apparent mass of the system consisting of the vibration generator, drive motor, and ground piston resting on the soil at test site is plotted in Fig. 5. The data have been fitted with a curve showing the calculated apparent mass for a 4-ton mass supported by a massless spring having vertical stiffness 100 kilonewtons per millimeter. Total mass of the vibration generator, drive motor, and ground piston was 3.9 tons. If these behaved as a rigid body, it would be expected that the apparent mass of the system would be larger than 3.9 tons because of the entrained mass of soil beneath the ground piston, which moves with the piston. The data suggest that this entrained mass varied from less than 0.1 ton at 33 Hz, to a value of 5 tons at 12 Hz. The entrained mass for a piston with radius 0.91 meters looking into a fluid with density 1.5 tons per cubic meter would be 3.0 tons.

Stiffness

The apparent stiffness of the system is plotted in Fig. 6 and the data are fitted by the calculated stiffness of a linear spring with stiffness 100 kilonewtons per millimeter which is supporting a rigid mass of 4 tons. The data suggest that the value of spring stiffness chosen is appropriate over the range 4 Hz to 9 Hz.

Damping

The values of damping calculated from the vertical-motion data were significantly different for the runs conducted July 18 and those conducted July 22. Values for the two days are shown separately in Figs. 7 and 8. The values of damping are shown in terms of an error band representing the ranges of damping corresponding to errors of

10 percent in amplitude and 10 degrees in phase angle. As the width of the error band in Fig. 8 suggests, the measured dampings below 10 Hz are quite unreliable. Values of damping which had overlapping error ranges were averaged in an attempt to improve the accuracy of the data.

Change in Damping

It is tempting to assume that the large change in damping between Figs. 7 and 8 was the result of the rainstorm which soaked the test area between July 18 and July 22. The data in Fig. 7 (dry soil) have been fitted with an average viscous damping of 150 kilonewton—seconds per meter. This value seems an appropriate average over the frequency range 20 Hz to 30 Hz, near the vertical natural frequency of the system. The damping in Fig. 7 decreases with increasing frequency in the range from 10 Hz to 20 Hz, indicating that the damping is more nearly proportional to displacement than to velocity. This type of damping is characteristic of hysteresis or friction damping, and suggests that the damping may have been associated with friction between the ground piston and the soil. The data in Fig. 8 (wet soil) have been fitted with a curve representing the calculated low-frequency radiation damping for a piston with radius 0.91 meters looking into a fluid having density 1.5 tons per cubic meter and speed of sound 132 meters per second. Here the damping increases as the square of the frequency, following the trend suggested by the damping values in the range from 10 Hz to 20 Hz in Fig. 8.

Transmission Along the Surface of the Ground

The smooth variation of phase with distance shown in Fig. 10 despite the varying character of the ground surface (grass, gravel, concrete) suggests that the waves measured were not being transmitted along the ground surface. The curvature of the phase plot also shows that the waves did not travel at constant velocity. The curve fitted to the phase data assumes that the velocity of the waves increases with depth with a constant velocity gradient of 14.4 inverse seconds and a surface velocity of 132 meters per second. On this model, for example, the waves received at the last station (distance 32.0 meters, near the middle of the concrete floor of the Balloon Room of Building 5)left the ground piston travelling downward at an angle of 150 degrees from the vertical. They reached a maximum depth of 9.3 meters at a point halfway to Building 5, and had a maximum speed of 266 meters per second at that depth. They were then refracted upward and arrived from beneath the floor of Building 5 travelling upward at an angle 30 degrees from the vertical. Calculated travel time along this path is 184 milliseconds and is shorter than the travel time calculated

along any other path. The data do not indicate what type of wave is measured (shear, compression, or a combination).

Attenuation of the Transmitted Waves

The upward refraction indicated by the velocity-structure model developed from the phase-velocity data implies that motions at the ground surface should not decrease as rapidly with distance as they would if they were not augmented by the refraction. Data on vertical amplitudes in Fig. 9 have been fitted with calculated amplitudes for the refractive condition on the assumption that the ground piston transmitted an initial wave which had spherical symmetry and that the ground surface was uniform. The data points in Fig. 9 suggest that the ground surface had some effect on amplitude. Amplitudes drop suddenly when the gravel (parking lot) is encountered, and drop rapidly again at the concrete floor for Building 5. The measured amplitudes also tend overall to decrease more rapidly with distance than indicated by the calculation. This may indicate a general spreading of the refractive pattern caused by a slight decrease in the velocity gradient with depth. Such a decrease is also suggested by the differences between the phase data and the fitted arrival-time curve; actual arrival times were slightly greater than calculated at distances beyond 25 meters. The waves arriving at the greatest distance also travelled to the greatest depth, and their actual velocity did not seem to be quite as large as that determined from the constant-gradient model.

Rotational Motions

The rotational motions of the ground piston plotted in Fig. 11 were presumably driven by small unbalanced horizontal forces and moments developed by the rotating masses in the vibration generator, or by small differences between the center of action of the vertical force and the center of reaction of the soil on the ground piston. Note that there was appreciably less rotation of the ground piston during tests conducted on wet soil July 22 than on dry soil July 18. The decreased rotation may represent better coupling of the ground piston to wet soil than to dry, and may explain in part the decreased damping observed on July 22.

Motions of the Vibration Generator

The single measurement made atop the drive motor for the vibration generator during Run 13 showed that the vertical amplitude of the motor (58 milligravities) was only 28 percent of the average vertical amplitude of the ground piston (210 milligravities) during

that run. The presence of differential motions in the equipment indicates that it is not appropriate to consider the ground piston, vibration generator, and drive motor as a single mass as was done in interpreting the mass data of Fig. 5. No information seems to be available, however, on the resonant frequencies and modeshapes of the vibration generator and its associated equipment. Internal resonances would act to decrease the apparent mass of the generator-piston combination and produce an underestimate of the entrained mass of soil moving with the ground piston.

ESTIMATES FOR BUILDING FOUNDATION

Scaling

Data from the ground piston may be scaled to a building foundation by multiplying all linear dimensions by a scale factor S and requiring that the scaling leave the density of the soil and the stresses in the soil unchanged. These three requirements completely determine the scaling and produce what is known as inertia scaling or Hopkinson scaling. In this scaling, frequencies vary as $1/S$, masses as S^3, stiffnesses as S, dampings as S^2, and so on. Inertia scaling has the unrealistic feature that it scales depths in the ground, while the depths to various layers in the ground actually should remain unchanged in the scaled-up structures. Inertia scaling also scales accelerations by $1/S$, while the acceleration of gravity should remain unchanged in the scaled-up structure.

Example

Data from the ground piston are scaled here to a reinforced-concrete mat 14 meters long by 6 meters wide which has a total mass of 73 tons. The mat has an area of 84 square meters while the ground piston had an area of 2.60 square meters. A linear scale factor may be defined to match the areas:

$$S = \sqrt{84/2.60} = 5.68 \qquad (1)$$

Suppose that equipment is to be mounted on the mat using resilient mounts which support the equipment at a natural frequency of 8 Hz. Scaled down to the ground piston, the frequency of special interest becomes

$$8\,S = 45 \text{ Hz.} \qquad (2)$$

At the highest frequencies tested, data from the ground piston indicate an effective mass of 4.0 tons (Fig. 5), a stiffness of 100 kilonewtons per millimeter (Fig. 6), and a damping of about 100 kilonewton-seconds per meter (Fig. 7). Of the mass, 3.9 tons represents the ground piston and vibration generator, leaving 0.1 ton as an entrained mass of soil. The data scale as follows:

$$0.1\,S^3 = 18 \text{ tons entrained mass.} \qquad (3)$$

$$100\,S = 570 \text{ kilonewtons per millimeter stiffness} \qquad (4)$$

$$100\,S^2 = 3200 \text{ kilonewton-seconds per meter damping.} \qquad (5)$$

Total mass of the slab and entrained soil is 91 tons. Its vertical natural frequency is

$$\frac{1}{2\pi}\sqrt{\frac{570{,}000}{91}} = 13 \text{ Hz} \tag{6}$$

and its damping relative to critical is

$$\frac{1}{2}\frac{3200}{\sqrt{570{,}000}\sqrt{91}} = 0.22. \tag{7}$$

The values of frequency and damping do not make any allowance for the reaction of the supported equipment.

Alternate Scaling (Not Recommended)

The data from the ground piston may be scaled by applying the scaling factor S to horizontal dimensions only and still requiring that the density of the soil and the compressive stresses from a vertical force remain unchanged. This scaling avoids the problem of the preceding scaling in that it does not require depths in the ground or the vertical acceleration of gravity to scale unrealistically. For this scaling, vertical frequencies are unchanged, masses vary as S^2, stiffnesses as S^2, and dampings as S^2. The ground-piston data should be consulted at a frequency of 8 Hz to obtain an estimated entrained mass of 0.1 ton, a stiffness of 100 kilonewtons per millimeter, and damping (wet soil) of 20 kilonewton-seconds per meter. These values scale up to:

$$0.1\ S^2 = 3 \text{ tons entrained mass} \tag{8}$$

$$100\ S^2 = 3200 \text{ kilonewtons per millimeter stiffness} \tag{9}$$

$$20\ S^2 = 640 \text{ kilonewton-seconds per meter damping.} \tag{10}$$

Total mass of the mat and entrained soil is 76 tons. Vertical natural frequency is 33 Hz and damping is 2 percent of critical. This scaling is not recommended because it incorrectly represents the shear stresses produced by vertical forces applied to the mat. The forces scale as S^2 but the vertical shear areas scale only as S, so that shear stresses produced in the soil by the mat appear as S times the shear stresses produced by the ground piston. The increase in shear stress is not matched by any increase in shear strain, and the mat thus appears to be much more stiffly supported than when the estimates are made by the recommended scaling.

English Units

Data from the recommended scaling in Equations 3 through 5 can be converted to English units by using 1 ton = 2204.6 pounds, 1 kilonewton = 225 pounds, and 25.4 millimeters = 1 inch. Results are:

Dimensions of reinforced-concrete mat	20 by 46 feet
Weight of mat	160,000 pounds
Entrained weight of soil	40,000 pounds
Stiffness for vertical support	3,200,000 pounds per inch
Damping	1,500,000 pound-second per foot.

SUMMARY AND CONCLUSIONS

Tests Conducted

Tests were conducted at a point about 30 meters north of Building 5 of the Chesapeake Bay Division of the Naval Research Laboratory. The Chesapeake Bay Division overlooks Chesapeake Bay three miles south of Chesapeake Beach, Maryland. A rotating-mass vibration generator was mounted to a steel ground piston 1.8 meters in diameter (total mass 3.9 tons) and vertical forces from 0.3 to 22 kilonewtons were applied at frequencies from 3 Hz to 33 Hz. The resulting motions of the piston and the ground surface were measured with accelerometers. One record of an automobile passing the test site was also taken.

Test Findings

1. The ground responded as a nearly linear medium over the range of forces and frequencies tested.
2. The ground piston and vibration generator responded approximately as a linear system with vertical natural frequency 25 Hz and damping 12 percent of critical near resonance.
3. Mass of the entrained soil moving with the ground piston varied from 0.1 ton to 5 tons and was very small above the resonant frequency.
4. Apparent stiffness of the soil supporting the ground piston was 100 kilonewtons per millimeter.
5. Near resonance damping of the soil was about 150 kilonewton-seconds per meter. Damping in the range 10 Hz to 20 Hz decreased with increasing frequency when the ground was dry but the low-frequency damping fell nearly to zero after a rainstorm at the test site.
6. There was no indication of strong reflections or standing waves.
7. The velocity of 20-Hz waves transmitted from the piston was 132 meters per second at the ground surface but increased to 266 meters per second at a depth of 9 meters.
8. A passing automobile produced accelerations equivalent to a very strong earthquake (22 milligravities) at the ground piston.

Scaled Estimates for Building Foundation

1. A reinforced-concrete mat 20 feet by 46 feet would have its apparent mass increased by 40 thousand pounds by entrained mass of the adjacent soil which would move with it for vertical motions.
2. The mat would be supported with an effective ground stiffness of 3.2 million pounds per inch for vertical motions.
3. Vertical damping for the mat would approximate 1.5 million pound-seconds per foot.
4. If the mat weighed 160 thousand pounds it would be supported with a vertical natural frequency of 13 Hz and a damping 22 percent of critical.

ACKNOWLEDGMENTS

The experiment reported here was suggested by Donald J. McLaughlin of the Applications Research Division, who also made preliminary arrangements for conducting the tests. All of the equipment used for the tests (vibration generator and instrumentation) was supplied by the Naval Ship Research and Development Center, Washington, D.C. William E. Leyda of the Center arranged for transportation and installation of the equipment, and also installed and operated all of the instrumentation. Richard K. Brown and Irvin L. Young of the Center operated the vibration generator and assisted in the conduct of the tests. Robert Conlyn and Albert C. Grosvenor of the Chesapeake Bay Division of the Naval Research Laboratory arranged for site preparation, instrumentation space, electrical power, and all of the other miscellaneous requirements of a test program.

REFERENCES

1. Price, Richard L., "The TMB 5000 Pound, Three-Mass Vibration Generator, Its Description and Operation," Washington, D. C., David Taylor Model Basin* Report No. 1781 (December 1963).

*Now the Naval Ship Research and Development Center, Washington, D.C. 20007

Table 1

Locations of Transducers

Transducers were Kistler Servo Accelerometers Model 305T, mounted with sensitive axes in the directions shown. Coordinates show distances of the center of the transducer from the center of the bottom of the ground piston along orthogonal axes taken as positive toward the southeast, northwest, and upward.

Position Number	Direction of Positive Acceleration	Transducer Attached To:	Coordinates		
			SE (meters)	NE (meters)	UP (meters)
1	UP	Top of ground piston near northeast edge	0.00	0.83	0.17
2	UP	Top of ground piston near southeast edge	0.82	0.03	0.17
3	UP	Top of ground piston near southwest edge	0.00	-0.83	0.17
4	UP	Top of ground piston near northwest edge	-0.82	-0.02	0.17
5	NE	Rim of ground piston on northeast side	0.00	0.88	0.13
6	NE	Top of ground piston near southeast edge	0.75	0.03	0.17
7	SE	Top of ground piston near southeast edge	0.69	0.03	0.17
8	UP	Top of steel block	22.6 a	-22.6 b	1
9	NE	Side of steel block	22.6 a	-22.6 b	1
10	SE	Side of steel block	22.6 a	-22.6 b	1

a - For runs 1 through 13. Placed 21.6 meters southeast of ground piston for runs 14 through 23.

b. For runs 1 through 13. Placed 21.6 meters southwest (-21.6 meters northeast) of ground piston for runs 14 through 23.

Table 2

Test Runs Conducted

The vibration generator contained three 91-kilogram masses which were adjusted by angle markings A to produce eccentricities calculated as 89 sin (A/2) millimeters. Forces below are centrifugal forces calculated from masses, eccentricities, and speeds of angular rotation about an assumed stationary axis.

Run Number	Frequency		Amplitude of Vertical Force (kilonewtons)	Eccentricity and Phase Settings
	Revolutions per minute	Hertz		
1	300	5.0	0.278	Center mass set to 2 degrees (1.55 mm) and outer masses set to 1 degree (0.78 mm). Phased for vertical forces (all three masses moved upward simultaneously).
2	600	10.0	1.11	
3	900	15.0	2.51	
4	1200	20.0	4.46	
5	1500	25.0	6.96	
6	1800	30.0	10.0	
7	1800	30.0	10.0	
8	2000	33.3	12.4	
9	1219	20.3	4.6	
10	a	b	c	
11	600	10.0	1.11	
12	840	14.0	2.18	
13	1200	20.0	4.46	
14	181	3.0	1.01	Center mass set to 20 degrees (15.5 mm) and outer masses set to 10 degrees (7.8 mm). Phased for vertical forces (all three masses moved upward simultaneously).
15	240	4.0	1.78	
16	300	5.0	2.78	
17	360	6.0	4.00	
18	420	7.0	5.44	
19	480	8.0	7.11	
20	540	9.0	8.99	
21	600	10.0	11.1	
22	720	12.0	16.0	
23	840	14.0	21.8	

a - Sweep from 300 rpm to 2000 rpm in about 2 minutes
b - Sweep from 5.0 Hz to 33.3 Hz
c - Sweep from 0.278 kn to 12.4 kn.

Table 3

Acceleration Amplitudes Read from Oscillograms

Tabulated values are the estimated amplitudes of the vibration component having the same frequency as the vibration generator. Amplitudes have been corrected for the low-frequency gains of the DTMB amplifiers used.

Run	Acceleration Amplitudes (milligravities) for Positions 1 through 10									
	Pos 1	Pos 2	Pos 3	Pos 4	Pos 5	Pos 6	Pos 7	Pos 8	Pos 9	Pos 10
1	a	a	a	a	1	a	b	c	c	c
2	28	11	30	9	10	11	b	0.08	0.03	c
3	99	11	160	52	240	35	87	140 d	0.53	c
4	260	310	390	190	350	32	39	3.5	0.16	0.24
5	800	860	980	720	200	230	76	6.2	3.1	2.1
6	860	860	900	640	210	170	100	15	6.6	1.6
7	850	860	800	660	220	170	93	15	5.5	1.2
8	1040	1060	980	900	240	170	130	8.0	2.3	1.9
9	470	380	670	340	110	90	39	4.1	2.6	2.5
10	e	e	e	e	e	e	e	e	e	e
11	8.7	7.7	8.9	8.0	3.8	5.6	1.4	0.09	0.03	0.05
12	140	80	170	79	66	83	15	1.7	0.55	0.35
13	170	230	390	180	44	47	7.8	2.5	0.59	2.6
14	1.5	1.0	1.9	2.0	0.57	0.54	0.51	c	c	c
15	1.4	1.9	2.8	1.4	0.92	0.88	0.69	c	c	c
16	2.4	3.5	3.7	3.4	1.1	1.4	1.2	0.04	c	c
17	7.8	3.9	9.9	5.7	2.7	3.5	1.8	0.05	0.05	c
18	8.7	9.7	16	10	2.3	3.5	2.4	0.06	0.03	c
19	17	17	39	18	5.9	8.2	3.4	0.10	0.08	0.05
20	31	31	68	32	18	22	4.9	0.23	0.18	0.07
21	44	58	110	55	32	39	5.4	0.73	0.34	0.24
22	200	190	430	210	150	160	16	2.7	1.5	0.80
23	600	500	570	530	120	130	51	9.4	1.5	1.8

a - Less than 2 milligravities (obscured by machinery noise)
b - Less than 0.2 milligravities (obscured by machinery noise)
c - Less than 0.02 milligravities (below minimum reading)
d - Doubtful scaling of record
e - Sweep record with varying frequency and response.

Table 4

Acceleration Phases Read from Oscillograms

Tabulated values are the estimated phase lags of the positive accelerations after the maximum upward force, for the vibration component having the same frequency as the vibration generator. Phases have been corrected for the low-frequency phase shifts of the DTMB amplifiers used.

Run	Acceleration Phases (degrees) for Positions 1 through 10									
	Pos 1	Pos 2	Pos 3	Pos 4	Pos 5	Pos 6	Pos 7	Pos 8	Pos 9	Pos 10
1	a	a	a	a	211	a	a	a	a	a
2	291	266	153	207	121	117	a	294	117	a
3	149	232	270	238	282	288	296	11	316	a
4	228	250	273	250	98	53	114	127	332	0
5	327	327	336	327	209	236	310	318	12	102
6	291	313	302	261	127	237	341	248	62	297
7	291	324	313	291	215	215	342	237	52	265
8	15	27	3	326	290	290	74	171	15	146
9	272	286	279	272	111	118	165	198	264	55
10	b	b	b	b	b	b	b	b	b	b
11	212	198	150	176	110	110	96	289	296	234
12	35	198	203	167	228	228	203	249	290	91
13	163	236	243	243	323	316	258	134	272	10
14	217	212	215	214	19	18	219	a	a	a
15	50	217	212	176	272	275	116	a	a	a
16	231	116	203	221	257	210	68	26	a	a
17	159	207	145	200	248	263	58	34	139	a
18	188	181	186	183	188	255	191	78	226	a
19	182	182	188	202	208	234	119	116	240	326
20	221	198	159	156	169	179	143	208	309	84
21	172	161	164	172	190	200	182	222	306	179
22	130	169	191	182	235	230	222	65	135	139
23	172	187	197	192	304	273	218	273	284	50

a - Oscillations at frequency of vibration generator not distinguishable on record

b - Sweep record with varying frequency and response.

Table 5

Ground Motions at Different Distances from the Ground Piston

The data below were taken during Run 13 (20.0 Hz) along a line extending to the south from the ground piston. The accelerometers at Positions 8, 9, and 10 were carried to the desired location and the steel block to which they were attached was placed on the surface of the ground to obtain the measurements. Phases are lags of the positive acceleration relative to upward force applied to the ground piston. Data at a distance of 32.0 meters represent the original location of Positions 8, 9, and 10 during Run 13.

Distance South of Center of Ground Piston (meters)	Acceleration Amplitude (milligravities)			Acceleration Phase (degrees)			Ground Surface
	Pos 8 (UP)	Pos 9 (NE)	Pos 10 (SE)	Pos 8 (UP)	Pos 9 (NE)	Pos 10 (SE)	
1.2	58	67	54	277	118	284	Grass
3.0	36	56	36	17	137	352	Grass
6.1	23	37	18	191	278	111	Grass
9.1	20	26	17	324	60	274	Grass
12.2	19	21	18	96	125	347	Grass
15.2	13	8.0	5.4	245	334	201	Gravel
18.3	14	2.5	2.0	10	40	237	Gravel
21.3	10	0.98	5.3	118	75	82	Gravel
24.4	7.5	1.1	1.5	235	293	184	Concrete pad
27.4	6.7	0.56	1.1	349	277	241	Concrete pad
30.5	3.2	1.1	2.3	82	234	10	Concrete floor
32.0	2.5	0.59	2.6	134	272	10	Concrete floor

Table 6

Vertical Motions of the Center of the Ground Piston

Phases and accelerations are weighted averages of the accelerations measured at Positions 1,2,3, and 4 about the edges of the ground piston. The phase angle represents lag of the upward acceleration relative to upward force. Velocity and displacement amplitudes were calculated from the frequency and the acceleration amplitude.

Run	Frequency (Hz)	Force Amplitude (kilonewtons)	Acceleration Phase (deg)	Amplitudes		
				Acceleration (m/sec^2)	Velocity (mm/sec)	Displacement (microns)
1	5.0	0.278	a	b	b	b
2	10.0	1.11	227	0.090	1.4	23
3	15.0	2.51	234	0.50	5.2	56
4	20.0	4.46	253	2.7	21	170
5	25.0	6.96	330	8.3	53	340
6	30.0	10.0	294	7.6	40	220
7	30.0	10.0	306	7.6	40	210
8	33.3	12.4	5	9.0	43	210
9	20.3	4.60	277	4.6	36	280
10	c	c	c	c	c	c
11	10.0	1.11	183	0.074	1.2	19
12	14.0	2.18	180	0.45	5.1	58
13	20.0	4.46	230	2.1	17	130
14	3.0	1.01	214	0.016	0.85	45
15	4.0	1.78	197	0.011	0.44	17
16	5.0	2.78	195	0.023	0.73	23
17	6.0	4.00	169	0.060	1.6	42
18	7.0	5.44	185	0.11	2.5	57
19	8.0	7.11	189	0.22	4.4	87
20	9.0	8.99	177	0.36	6.4	110
21	10.0	11.1	166	0.66	11	170
22	12.0	16.0	164	2.4	32	420
23	14.0	21.8	187	5.3	60	680

a - Oscillations not discernable on oscillograms
b - Accelerations less than 0.02 meters per second squared
c - Sweep record with varying frequency and response.

Fig. 1 - Test Site at the Chesapeake Bay Division. The photograph was taken looking south, and shows the vibration generator in the ground and Building 5 immediately behind it. The half-open overhead door in Building 5 leads into the Balloon Room, where recording instruments were installed and where some measurements of ground vibration were made. Photograph by Albert C. Grosvenor.

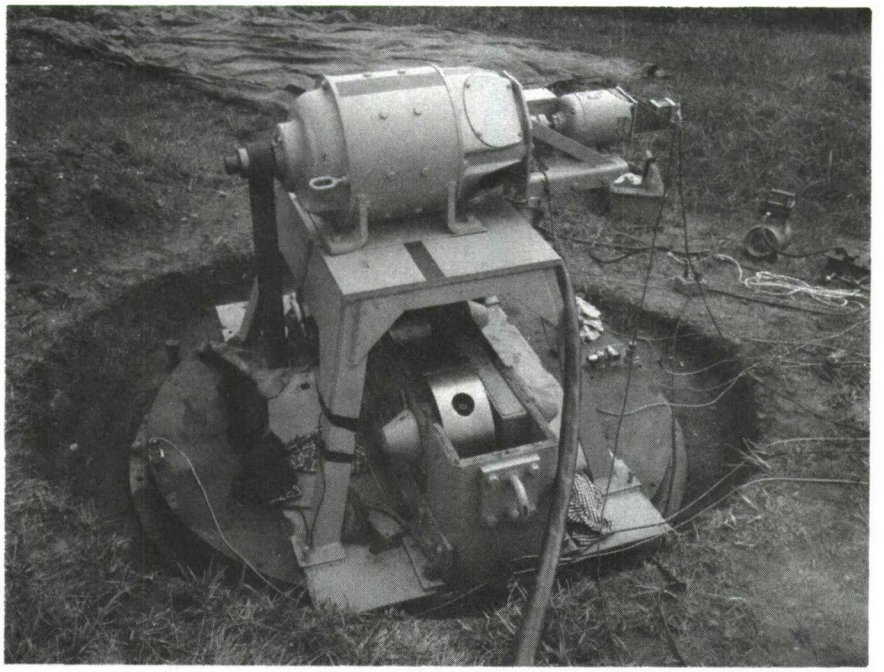

Fig. 2 - Vibration Generator and ground piston. The photograph was taken looking northeast and down, and shows the vibration generator, its drive motor mounted over it, and the ground piston installed in a shallow excavation needed to level the site. Five of the seven accelerometers mounted on the ground piston are visible in the photograph. One of the rotating masses in the vibration generator is visible at the nearer end of the generator. Photograph by Albert C. Grosvenor.

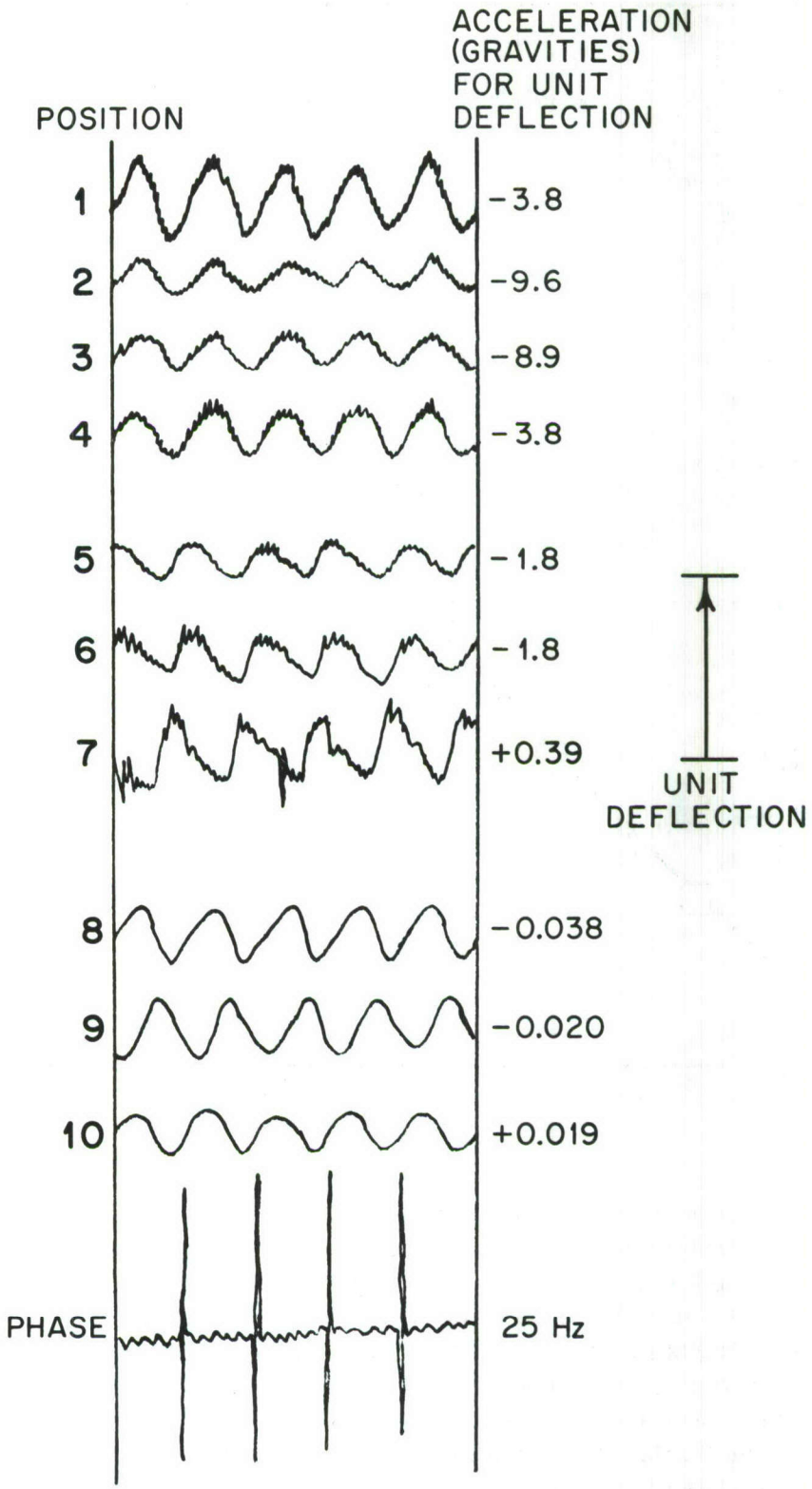

Fig. 3 - Typical record. The figure is a tracing of the oscillogram for Run 5.

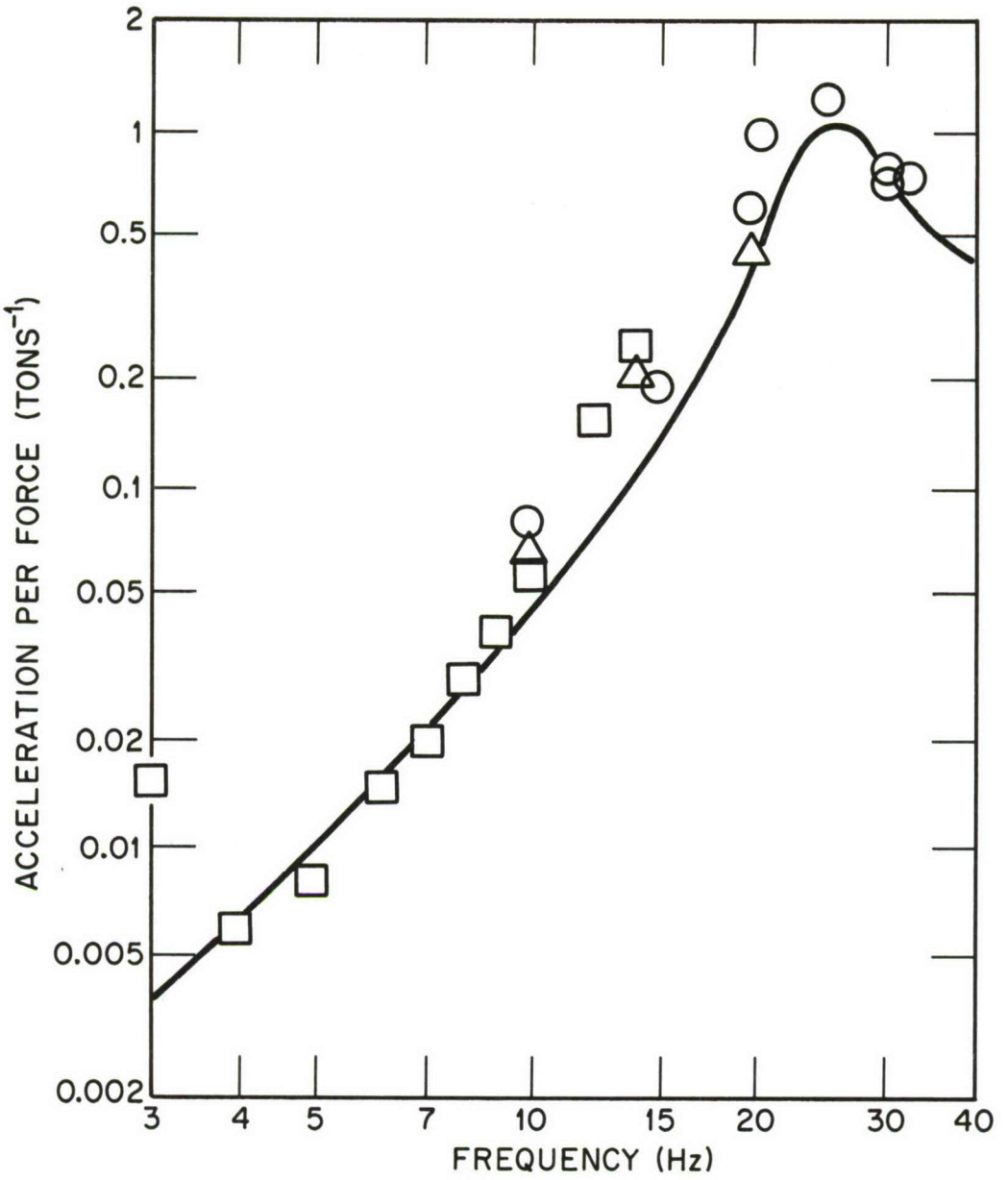

Fig. 4 - Resonance curve for vertical response of the ground piston. Amplitude of vertical acceleration of the piston has been scaled to unit force by dividing by the amplitude of the force, as for a linear system. Circles represent data from Runs 2 through 9, triangles are data from Runs 11 through 13, and squares are data from Runs 14 through 23. The vibration generator was reset to apply ten times as much vertical force after Run 13. Data from the low-force and the high-force runs overlap in the frequency range from 10 Hz to 14 Hz. The curve is for a system having natural frequency 25 Hz and damping 12 percent of critical.

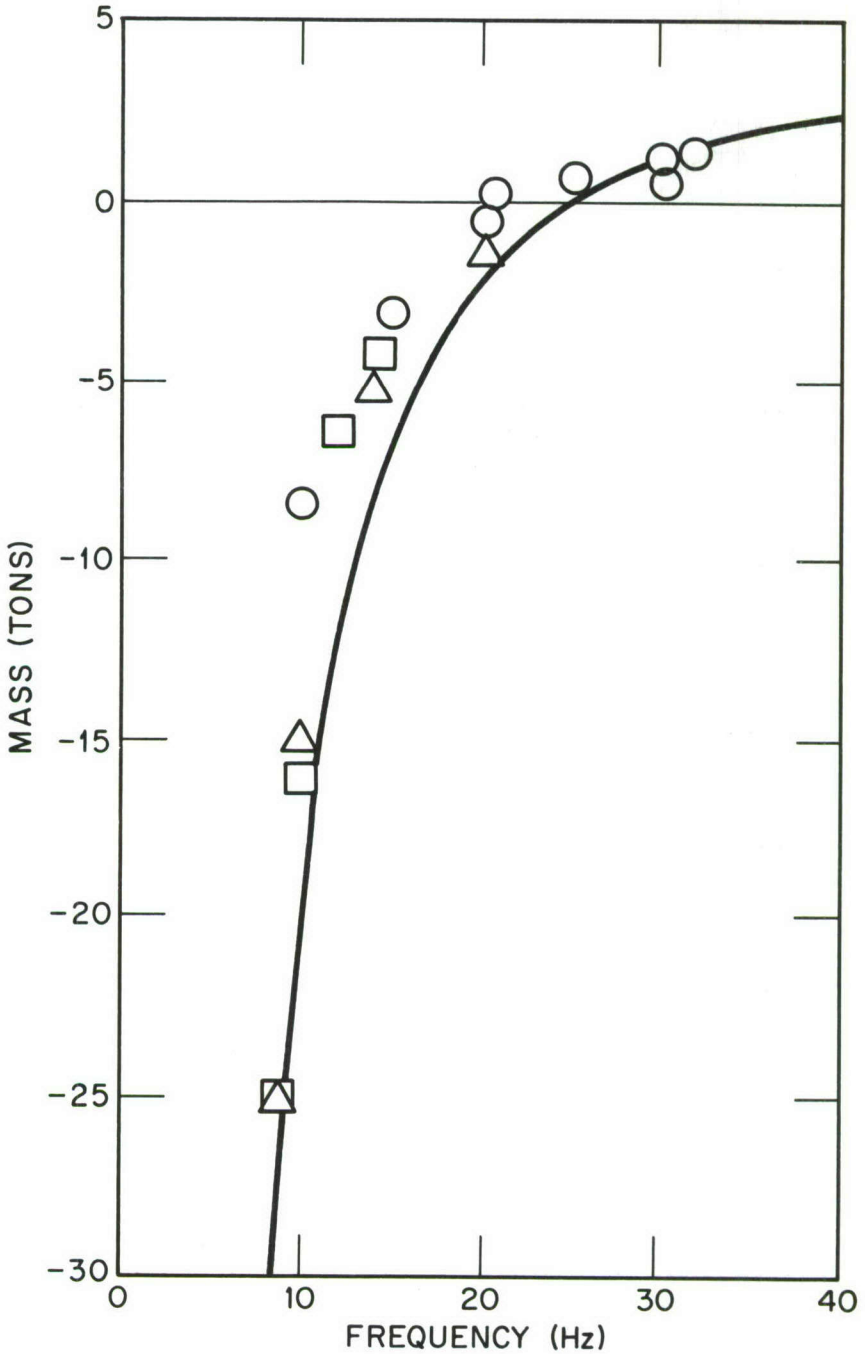

Fig. 5 - Apparent mass. Apparent mass is the ratio of the in-phase component of the force to the acceleration ($F = m\,a$). The curve shows calculated apparent mass for a 4-ton mass supported by a massless spring with stiffness 100 kilonewtons per millimeter. Circles are from vertical measurements of the ground piston during Runs 2 through 9, triangles are for Runs 11 through 13, and squares are for Runs 14 through 23.

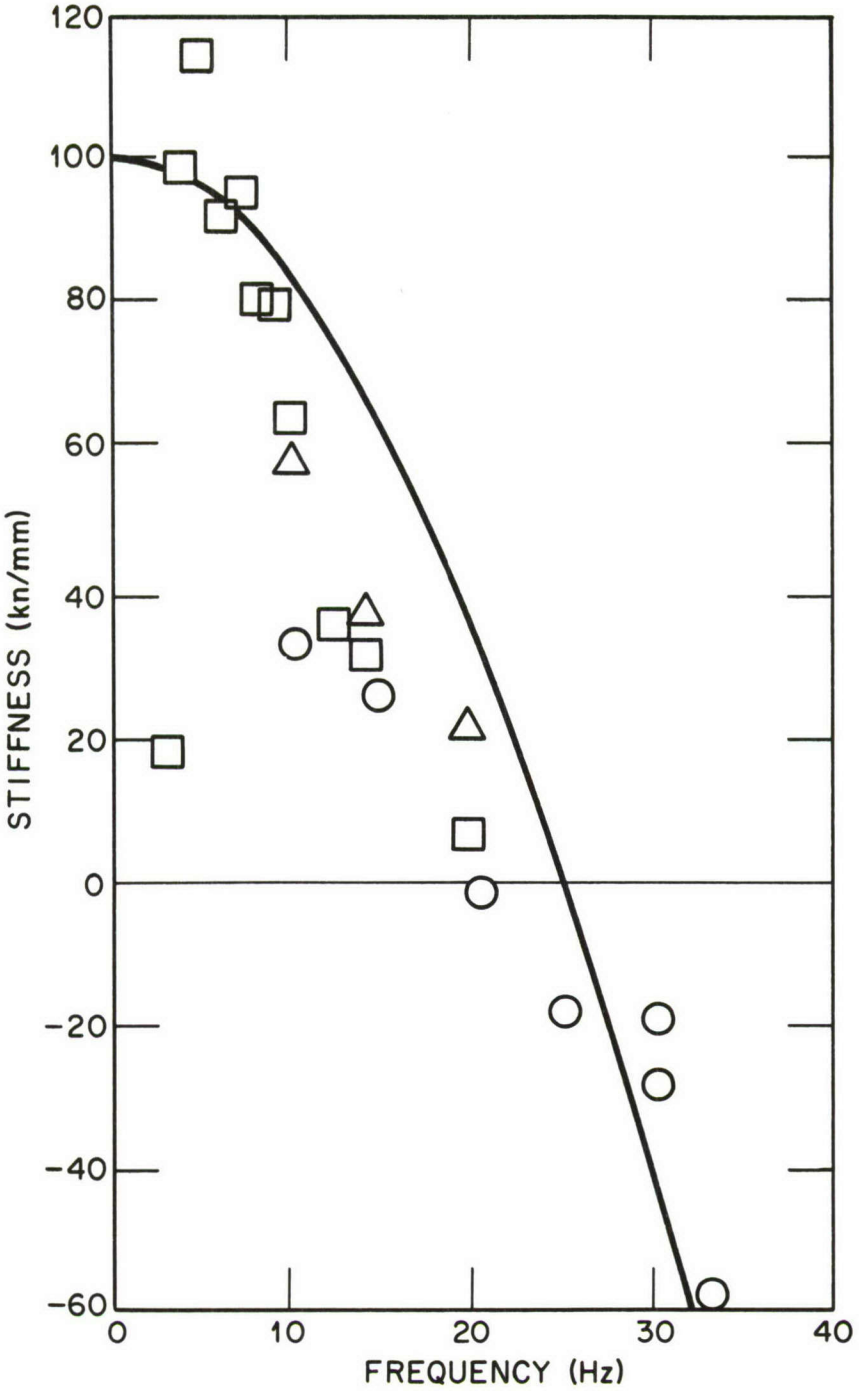

Fig. 6 - Apparent stiffness. Apparent stiffness is the ratio of the in-phase component of the force to the displacement ($F = kx$). The curve shows calculated apparent stiffness for a spring with stiffness 100 kilonewtons per millimeter which supports a mass of 4 tons. Circles are from vertical measurements of the ground piston during Runs 2 through 9, triangles are for Runs 11 through 13, and squares are for Runs 14 through 23.

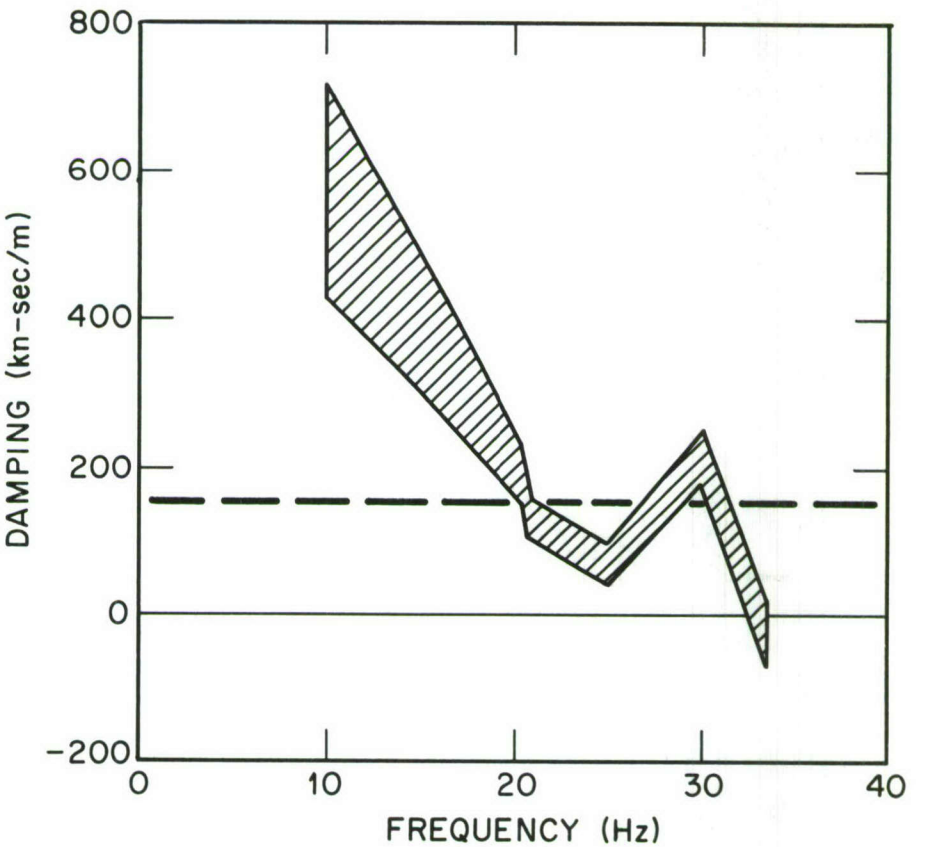

Fig. 7 - Apparent damping on July 18. Apparent damping is the ratio of the in-phase component of the force to the velocity ($F = cv$). Data are from vertical measurements of the ground piston during Runs 2 through 9 and are shown in terms of an error band representing estimated uncertainties of 10 percent in amplitude and 10 degrees in-phase for each response measurement. The horizontal broken line represents the apparent damping for a viscous damper with damping constant 150 kilonewton-seconds per meter.

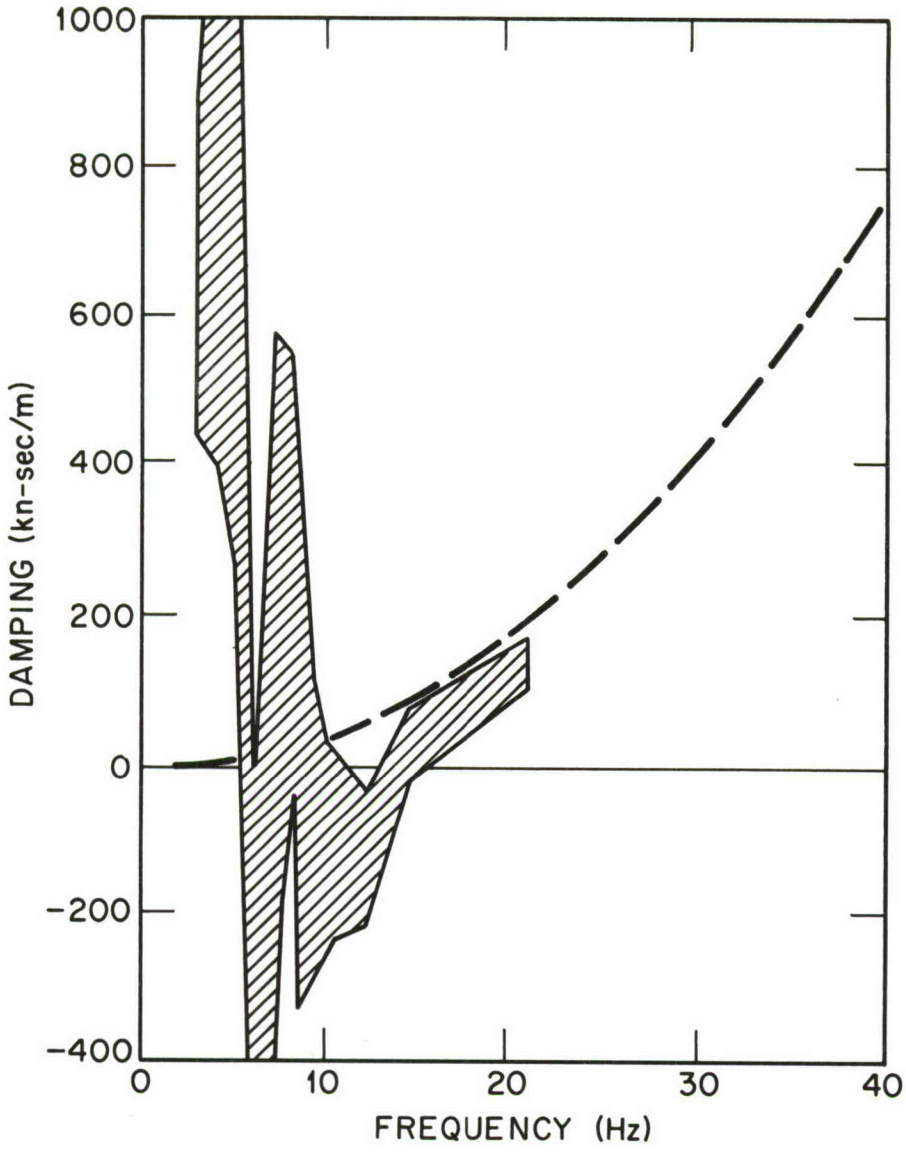

Fig. 8 - Apparent damping on July 22. Analysis and presentation is the same as in the preceeding figure, but the data are from Runs 11 through 23. The broken line represents the calculated low-frequency radiation damping for a piston 0.91 meters in radius looking into a fluid with density 1.5 tons per cubic meter and speed of sound 132 meters per second.

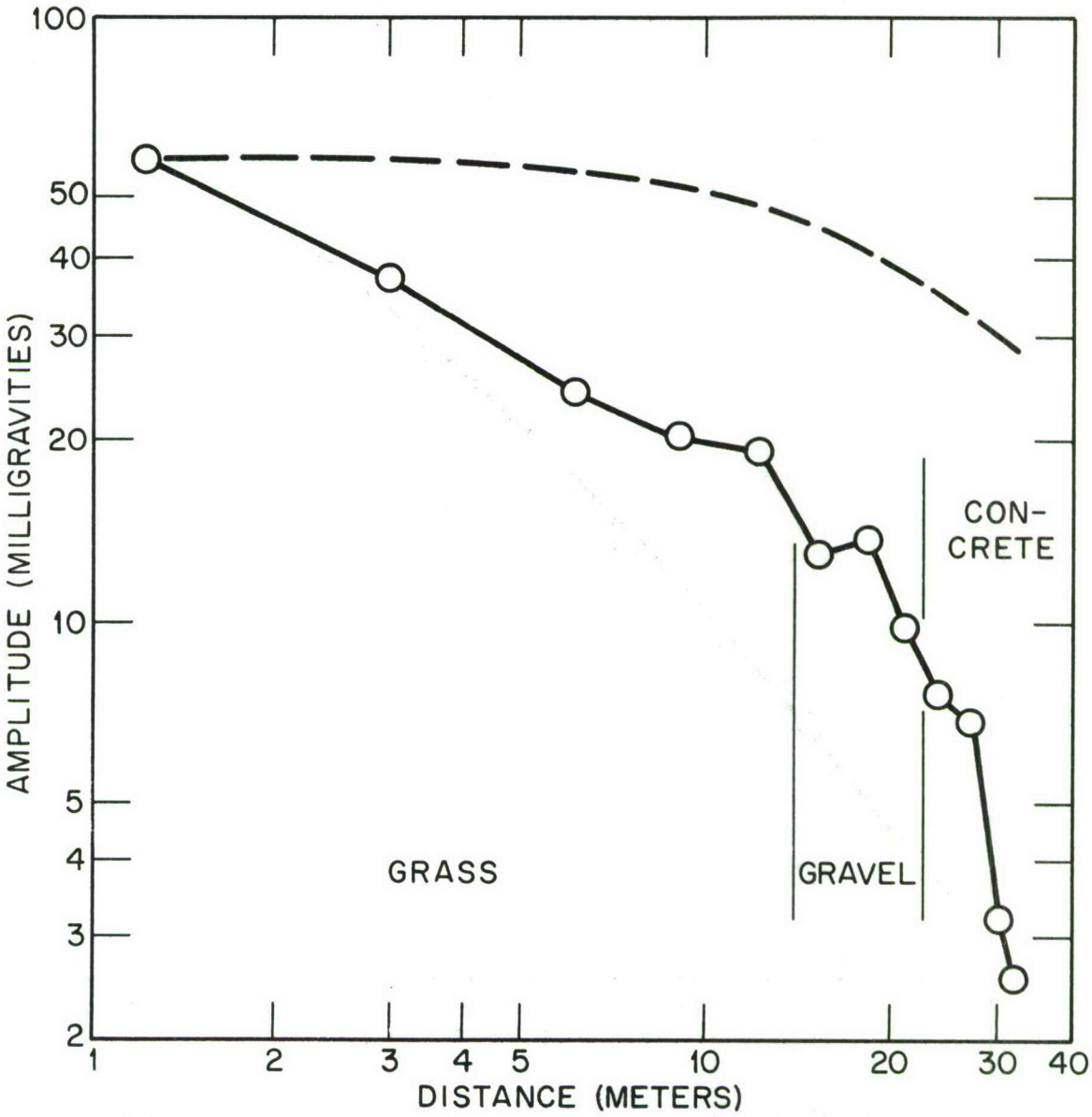

Fig. 9 - Acceleration amplitudes at the ground surface along a line extending south from the ground piston. The data points show amplitudes of vertical motions measured during Run 13 (20 Hz). The type of ground surface on which the accelerometer was placed is indicated. The broken line shows the calculated vertical motion of the ground surface which would be produced by a spherically-symmetric source operating under the upward-refracting conditions developed in the next figure.

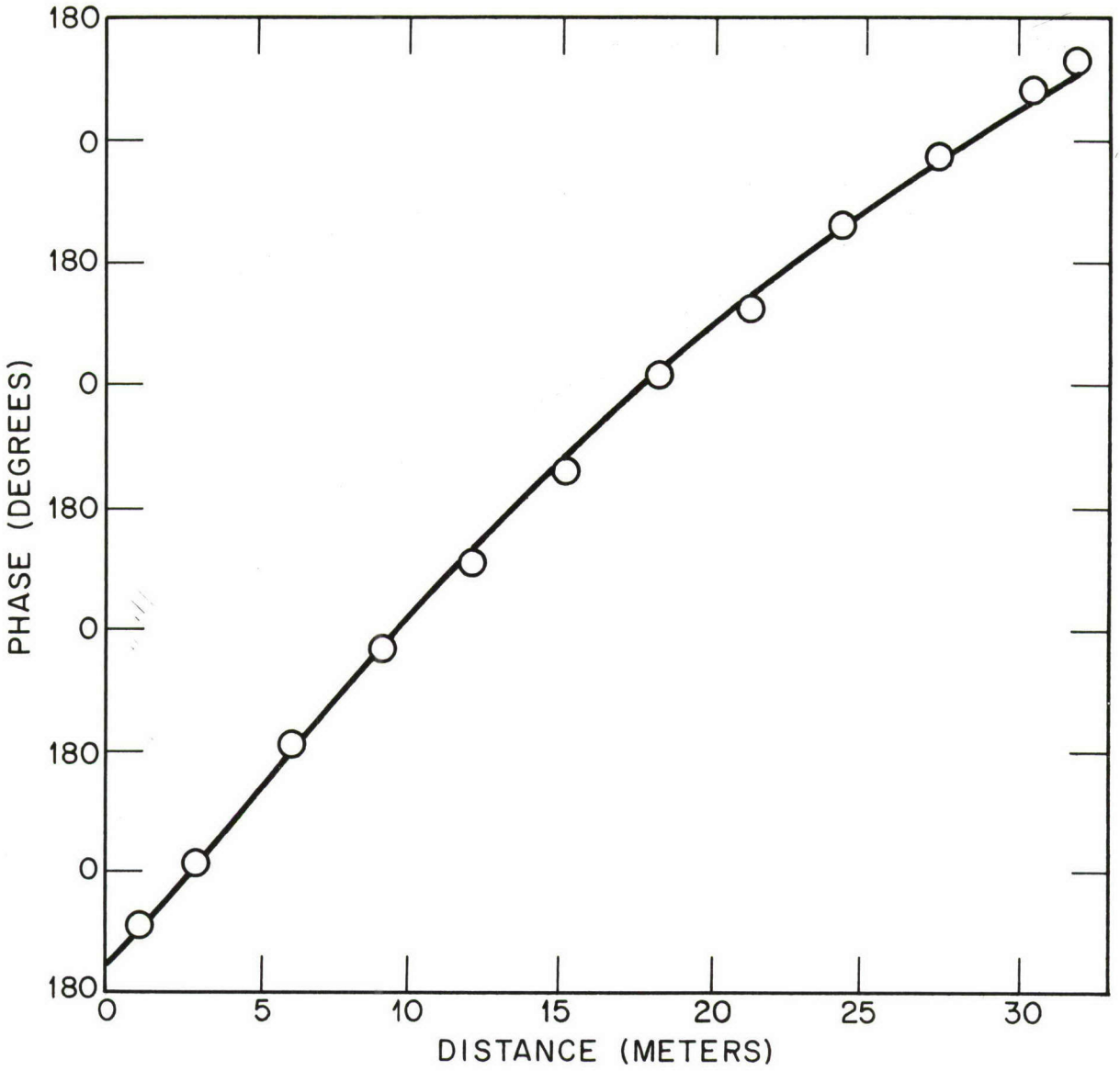

Fig. 10 - Phase shifts for 20-Hz waves transmitted away from the ground piston. Data points are the phases associated with the vertical amplitudes of the preceding figure. The curve represents phases calculated from travel times for minimum-time paths from the ground piston to the measurement points on the assumption that the velocity of the wave was 132 meters per second at the surface of the ground and that it increased by 14.4 meters per second for each meter of depth below the surface. The minimum-time paths under this condition dip downward into the ground and then turn back to approach the measurement point from beneath, suggesting an upward refraction of wave energy toward the surface.

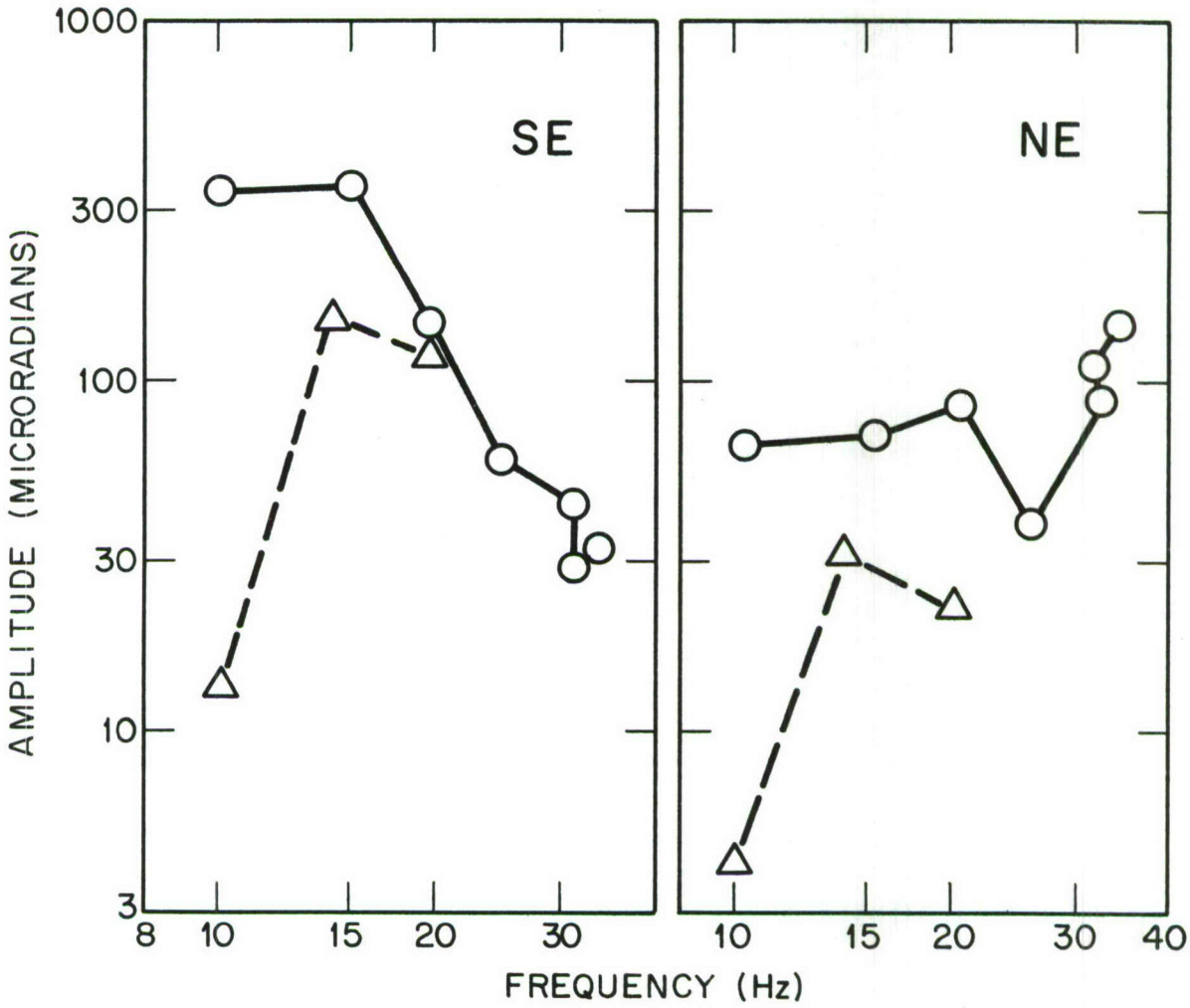

Fig. 11 - Rotations of the ground piston about horizontal axes. The graph at the left shows rotations about an axis toward the southeast, and the graph on the right shows rotations about the orthogonal axis toward the northeast. Circles indicate data from Runs 2 through 9 and triangles indicate data from Runs 11 through 13.

Appendix B

NRL Report 7038

Atmospheric Propagation with Thermal Blooming

J. W. TUCKER AND R. N. DEWITT

Applied Optics Branch
Optical Sciences Division

December 31, 1969

NAVAL RESEARCH LABORATORY
Washington, D.C.

CONTENTS

Abstract	ii
Problem Status	ii
Authorization	ii
INTRODUCTION	1
THE MODEL EQUATION	2
Normalization of the Distribution	2
The Eikonal Equation	2
Solution of the Eikonal	5
Numerical Applications	5
EFFECT OF OPTICAL FOCUSING	8
THE FAR FIELD OF A THERMALLY DEFOCUSSED BEAM	9
ASYMPTOTIC BEHAVIOR OF THE MODEL EQUATION	12
CONCLUSIONS AND SUMMARY	14
REFERENCES	15
APPENDIX – Far Field With Finite Aperture	16

ABSTRACT

Thermal blooming of a laser beam is described by a model equation for the trajectory of a selected profile ray. The model equation is applied to an examination of optical focusing for increasing transmitted power density. It is shown that the model equation is asumptotic in the far field to the geometric far field solution based on Snell's law for a stratified medium.

PROBLEM STATUS

An interim report on a continuing NRL Problem

AUTHORIZATION

NRL Problem R05-31.303
Project ORD 0832-129/173-1/V1754#2

Manuscript submitted December 16, 1969.

ATMOSPHERIC PROPAGATION WITH THERMAL BLOOMING

INTRODUCTION

Thermal defocusing of high-energy laser beams in liquids is a well known phenomenon (1-11) that has been used to measure weak absorptions (2). The analogous phenomenon in the atmosphere has been investigated in a simulated experiment (12).

As an intense laser beam propagates through the atmosphere, part of its energy will be absorbed by constituents of the air. This absorption will cause local heating with decrease in air density and refractive index in the beam. The bending of light rays toward regions of higher refractive index will cause the beam to spread. This phenomenon is referred to as thermal blooming or thermal defocusing, and it is the purpose of this report to develop simple equations descriptive of this effect under certain assumed conditions.

It is assumed that there is no wind and that convection and conduction can be neglected. True conduction is negligible, and conduction by microturbulence will be considered negligible for truly static air. Gravitational convection will be present but may be neglected for short time regimes because severe thermal blooming requires but a very small density differential.

As the atmosphere is rarely static, one might wonder what utility there is to a description based on such an assumption. The point is that static air represents the worst situation from the standpoint of thermal blooming and yet is the one situation that allows a simple closed form description of the development of thermal blooming. When wind is taken into account, a completely different and somewhat more approximate approach is needed. The figures for static air serve as references for the improvement due to wind, which will be considered in a later report.

It is assumed that the beam power density and the refractive index are radial Gaussian functions with the same spread parameter at a particular range and time. The assumption that the beam distribution remains Gaussian implies that there is no ray crossing, whereas the far field solution shows that ray crossing must be complete, that is, that the beam is turned inside out. It is important therefore to select as the profile ray one that is compatible with the far field solution. One can then hope that ray crossing will tend to balance out at intermediate ranges and that a solution that is asymptotically accurate at $z = 0$ and $z = \infty$ will be reasonably so at intermediate ranges.

Incidentally it is not necessary to use a Gaussian function for this method of solution to apply. It is, however, necessary to assume that the functional form of the radial distribution remains the same as the beam spreads. Alternate convenient distribution functions are

$$\begin{cases} P = 1 + \cos \dfrac{r^2}{b^2}, \quad 0 \le r \le \sqrt{\pi}\, b, \\ P = 0, \quad r > \sqrt{\pi}\, b, \end{cases} \tag{1}$$

and

$$\begin{cases} P = 1 + \cos \dfrac{r^2}{b^2} , \quad 0 \le r \le \sqrt{\dfrac{\pi}{2}}\ b , \\ \\ P = 0 , \quad r > \sqrt{\dfrac{\pi}{2}}\ b . \end{cases} \tag{2}$$

It is assumed that the total power in the beam is independent of range. With an absorption coefficient of 8×10^{-7} cm^{-1}, high-power beams will have done most of their bending in the first few kilometers before an appreciable fraction of the total beam power has been lost. For example at 2 kilometers the overall path transmission is

$$e^{-\alpha z} = e^{-0.16} = 0.85 . \tag{3}$$

THE MODEL EQUATION

Normalization of the Distribution

Consider a spreading beam as shown in Fig. 1. Let $a(z, t)$ be the characteristic beam radius with value a_0 at $z = 0$. The ray $r = a$ will generate a flared tube which will be considered the beam profile.

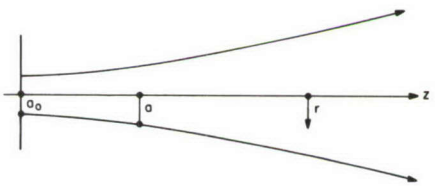

Fig. 1 - Beam geometry

Assuming that the radial distribution of power is Gaussian and remains Gaussian, the power flux can be written

$$P = N\, e^{-r^2/a^2} , \tag{4}$$

where N is a normalization constant. The total beam power W is then

$$W = 2\pi N \int_0^\infty e^{-r^2/a^2}\ r\ dr = \pi a^2 N . \tag{5}$$

Therefore

$$P = \frac{W}{\pi a^2}\, e^{-r^2/a^2} . \tag{6}$$

The Eikonal Equation

The change in refractive index Δn due to a change in density $\Delta \rho$ is

$$\Delta n = (n_0 - 1)\frac{\Delta\rho}{\rho} \tag{7}$$

$$= (n_0 - 1)\frac{\alpha t P}{C_p \theta \rho} \tag{8}$$

$$= (n_0 - 1)\frac{\alpha t}{C_p \theta \rho}\frac{W}{\pi a^2} e^{-r^2/a^2} , \tag{9}$$

where α is the absorption coefficient, C_p is the specific heat at constant pressure, ρ is the density, θ is the ambient temperature, and t is the time.

It will be noted that in Eq. (8)

$$\int_0^t P\, dt$$

has been replaced by Pt. The nature of this approximation may be judged from Fig. 2, which shows a plot of P for $r = a$ as the envelope of a set of Gaussian distributions. For example consider some down-beam point with radial coordinate r, where $a < r$ at $t = 0$ and $a = r$ as the profile ray bends and passes through the point r. It is when $r = a$ that the profile ray solution applies. For definiteness let $r = 15$ cm and let $a = 10$ cm at $t = 0$. From Fig. 2, $P = 1.07$ at $t = 0$ and $P = 1.63$ when $a = r$. For a linear decrease of P with time,

$$\int_0^t P\, dt = P_{av} t = 1.35\ t ,$$

whereas $P_t\, t = 1.63\ t$. Thus the approximation increases the predicted severity of blooming.

With the beam propagating along the z axis the deviation of the beam toward a higher refractive index is expressed in the equation (from Ref. 13) for the radius of curvature R,

$$\frac{1}{R} = \frac{1}{n}\frac{dn}{dr} \approx \frac{dn}{dr} , \tag{10}$$

since $n \approx 1$. The index of refraction n is

$$n = n_0 - \Delta n ,$$

so

$$n = n_0 - (n_0 - 1)\frac{\alpha t}{C_p \theta \rho}\frac{W}{\pi a^2} e^{-r^2/a^2} . \tag{11}$$

Then the radial index gradient is

$$\frac{dn}{dr} = (n_0 - 1)\frac{\alpha t}{C_p \theta \rho}\frac{W}{\pi a^2}\frac{2r}{a^2} e^{-r^2/a^2} . \tag{12}$$

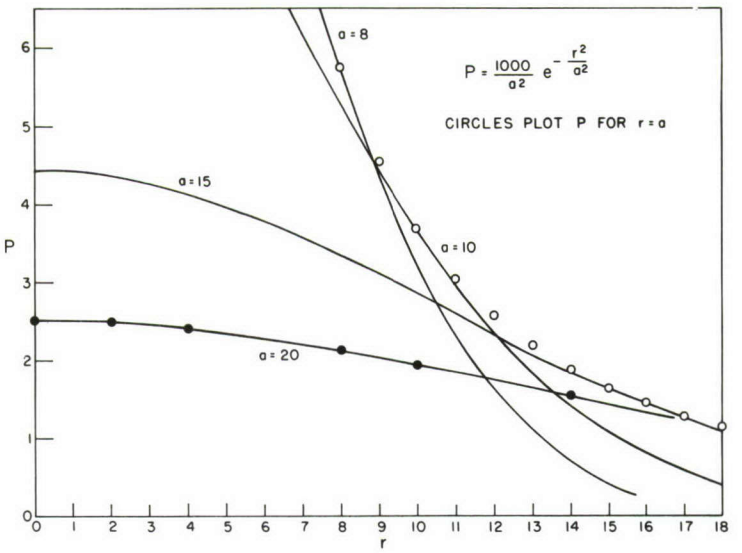

Fig. 2 - Profile power density as an envelope of a set of Gaussian distributions

Combining Eqs. (10) and (12) gives

$$\frac{1}{R} = \frac{2(n_0 - 1)\,\alpha W t r}{\pi C_p \theta \rho a^4}\, e^{-r^2/a^2} , \tag{13}$$

and, at $r = a$,

$$\frac{1}{R} = \frac{2(n_0 - 1)\,\alpha W t}{\pi e C_p \theta \rho a^3} . \tag{14}$$

But

$$\frac{1}{R} \approx \frac{d^2 a}{dz^2} , \tag{15}$$

and Eqs. (14) and (15) combined give the Eikonal equation for the ray $r = a$:

$$\frac{d^2 a}{dz^2} = \frac{2(n_0 - 1)\,\alpha W t}{\pi e C_p \theta \rho a^3} \tag{16}$$

or

$$\frac{d^2 a}{dz^2} = \frac{k^2}{a^3} , \tag{17}$$

where

$$k^2 = \frac{2(n_0 - 1)\alpha W t}{\pi e C_p \theta \rho} .$$

Solution of the Eikonal

If

$$p = \frac{da}{dz} \quad \text{and} \quad \frac{d^2a}{dz^2} = p\frac{dp}{da} , \tag{18}$$

Eq. (17) becomes

$$p\frac{dp}{da} = \frac{k^2}{a^3} . \tag{19}$$

Integration with $p = 0$ at $a = a_0$ gives

$$p^2 = k^2\left(\frac{1}{a_0^2} - \frac{1}{a^2}\right) \tag{20}$$

and

$$p = \frac{da}{dz} = \frac{k}{aa_0}\sqrt{a^2 - a_0^2} . \tag{21}$$

Integration with $a = a_0$ at $z = 0$ gives

$$a^2 = \frac{k^2}{a_0^2} z^2 + a_0^2 , \tag{22}$$

which may be recognized as a hyperbola starting from $r = a_0$ at $z = 0$ with $dr/dz = 0$ at $z = 0$ and asymptotic to the cones

$$r^2 = \frac{k^2}{a_0^2} z^2 . \tag{23}$$

Numerical Applications

Assigning the appropriate numerical values to the atmospheric parameters in Eq. (16) gives

$$\frac{k^2}{a_0^2} = \frac{2(n_0 - 1)\alpha W t}{\pi e C_p \theta \rho a_0^2} = \frac{W t \times 10^{-7}}{513\ a_0^2} , \tag{24}$$

where

$(n_0 - 1) = 3 \times 10^{-4}$,

$\alpha = 8 \times 10^{-7}$ cm^{-1},

$C_p = 0.96$ joule-g^{-1},

$\theta = 300$°K,

$\rho = 10^{-3}$ g-cm^{-3},

W = watts,

t = seconds.

From Eq. (22)

$$a^2 = \frac{Wt\ z^2 \times 10^{-7}}{513\ a_0^2} + a_0^2 \ . \tag{25}$$

For $Wt = 5130$ and $a_0 = 10$ cm Eq. (25) gives

$$a^2 = z^2 \times 10^{-8} + 100 \ , \tag{26}$$

and for $Wt = 51{,}300$ and $a_0 = 10$ cm Eq. (25) gives

$$a^2 = z^2 \times 10^{-7} + 100 \ . \tag{27}$$

If P_m is the power flux at the center of the beam at $z = 0$, then

$$P_m t = \frac{Wt}{\pi a_0^2} \ , \tag{28}$$

and for the preceding cases

$$P_m t = \frac{5130}{100\ \pi} = 16.3 \text{ joule-cm}^{-2} \tag{29}$$

and

$$P_m t = \frac{51300}{100\ \pi} = 163 \text{ joule-cm}^{-2} \ . \tag{30}$$

The beam profiles are plotted in Fig. 3 from Eqs. (26) and (27).

The effect of initial diameter on a constant-energy beam is shown in Fig. 4.

In Fig. 5, the energy density at the beam center is kept constant as the initial beam diameter is varied. In the far field it is seen that the direction and consequently the diameter is set by the energy density of the beam at $z = 0$.

In the far-field approximation when

$$a^2 \approx \frac{Wt\ z^2 \times 10^{-7}}{513\ a_0^2} \tag{31}$$

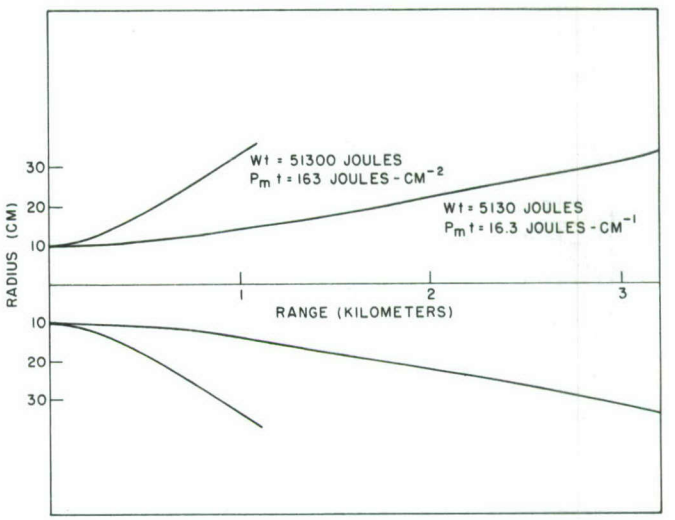

Fig. 3 - Effect of the beam energy on blooming

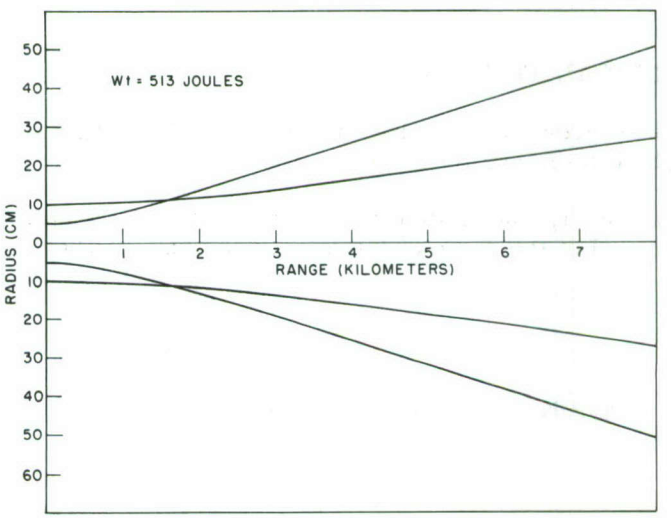

Fig. 4 - Effect of the initial diameter on a constant-energy beam (Wt = 513 joules)

and thermal blooming is dominant, it is seen that delivered energy is independent of beam energy Wt and is determined by the solid angle of the source aperture as seen from the receiver. Thus

$$\frac{Wt}{\pi a^2} \approx \frac{513\ a_0^2}{\pi z^2 \times 10^{-7}}$$

$$\approx 163 \times 10^{-7}\ \omega\ , \tag{32}$$

where $\omega = a_0^2/z^2$ is the solid angle subtended by the source aperture at the receiver.

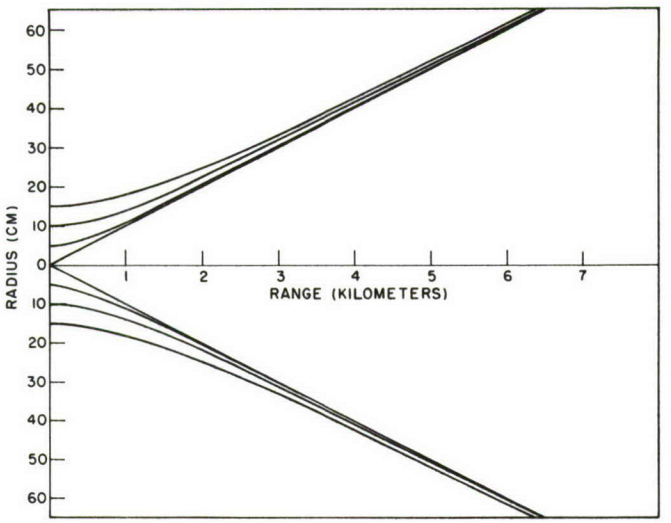

Fig. 5 - Profiles for constant energy density at the center of the initial beam ($P_m\ t$ = 16.3 joule-cm^{-2})

EFFECT OF OPTICAL FOCUSING

It is natural to investigate to what extent optical focusing may be useful in increasing the power density at a distant receiver.

As before, the energy deposited in the atmosphere is assumed to have a Gaussian radial distribution. Let the slope of the profile ray be m. Then Eq. (19) integrates to

$$\frac{p^2}{2} = -\frac{k^2}{2\,a^2} + A \ . \tag{33}$$

Substitution of the boundary conditions $p = m$ at $a = a_0$ gives

$$A = \frac{m^2}{2} + \frac{k^2}{2\,a_0^2} \ . \tag{34}$$

Thus

$$p = \frac{da}{dz} = \sqrt{\frac{L^2}{a_0^2} - \frac{k^2}{a^2}} \ , \tag{35}$$

where $L^2 = k^2 + m^2\,a_0^2$. This can be written

$$\frac{1}{a_0}\int dz = \frac{1}{2L^2}\int \frac{2L^2\,a\,da}{\sqrt{L^2a^2 - k^2a_0^2}} \tag{36}$$

to give

$$\frac{1}{L^2}\sqrt{L^2 a^2 - k^2 a_0^2} = \frac{z}{a_0} + B \ . \tag{37}$$

With $z = 0$ at $a = a_0$, Eq. (37) gives

$$B = \frac{a_0}{L^2}\sqrt{L^2 - k^2} \ , \tag{38}$$

which, when substituted back into Eq. (37) leads to

$$a^2 = \frac{k^2}{a_0^2} z^2 + (mz + a_0)^2 \ . \tag{39}$$

For the atmosphere, Eq. (24) gives

$$\frac{k^2}{a_0^2} = \frac{Wt \times 10^{-7}}{513\ a_0^2} \ ,$$

and Eq. (39) may be written

$$a^2 = \frac{Wt \times 10^{-7}}{513\ a_0^2} z^2 + (mz + a_0)^2 \ . \tag{40}$$

It is immediately obvious from Eq. (39) or Eq. (40) that a is a minimum at a particular range if the beam is focused for that range. Thus a is a minimum at range z when

$$m = -\frac{a_0}{z} \ . \tag{41}$$

As a practical matter the improvement achievable by optical focusing may be trivial. This will be the situation if the spread due to thermal blooming (or other mechanisms) is large compared to the original aperture. In Eq. (39), a is little affected by a_0 if $kz/a \gg a_0$. This will be illustrated by a numerical example. For $Wt = 1850$ joules and $a_0 = 10$ cm, Eq. (40) becomes

$$a^2 = 36 \times 10^{10} z^2 + (10 + mz)^2 \ . \tag{42}$$

This equation is plotted in Fig. 6 for the three slopes $m = 0$, $m = -2.5 \times 10^{-5}$, and $m = -5 \times 10^{-4}$ corresponding to no focusing, a 4-km focal point, and a 0.2-km focal point.

THE FAR FIELD OF A THERMALLY DEFOCUSSED BEAM

The far field refers to the final angular distribution of beam energy relative to the beam axis. In this analysis, diffraction effects are neglected, and the initial beam is assumed to be a plane wave with a Gaussian radial power distribution at the aperture. The assumption of a Gaussian distribution is not necessary but is consistent with the earlier model. (The appendix treats a non-Gaussian, finite distribution.) Because of the cylindrical symmetry, each ray travels in a plane passing through the beam axis, and the refractive index gradient direction lies in this plane. Under these conditions Snell's law for a stratified medium may be applied if the down-beam flaring of the heated region is neglected. Snell's law says that if the direction of the refractive index gradient is

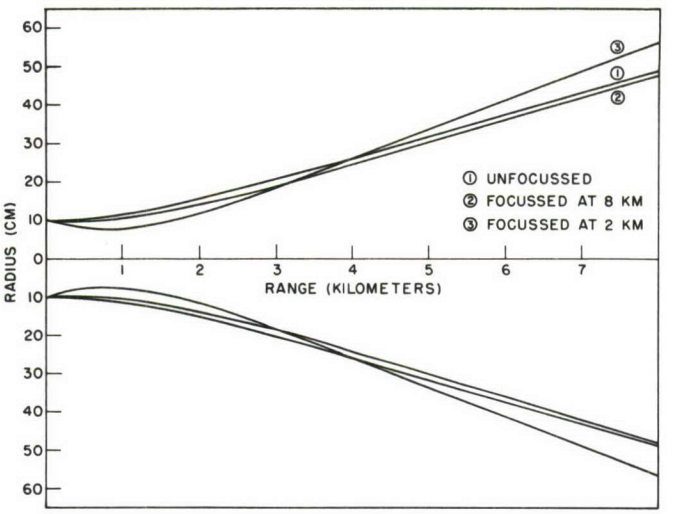

Fig. 6 - Effect of optical focusing on the beam profile

constant for a ray passing through a nonhomogeneous medium, then $n \sin \phi$ is constant, where ϕ is the angle between ray direction and gradient direction and n is the index of refraction of the medium. Let ψ be the angle between a ray and the beam axis in the far field, and let the ray start parallel to the beam axis from a aperture point where the index is n. Applying Snell's law to find the far-field angle in terms of the near-field index gives

$$\cos \psi = \frac{n}{n_0} \cdot \tag{43}$$

From Eq. (11), for small ψ

$$1 - \frac{\psi^2}{2} = \frac{1}{n_0} \left[n_0 - (n_0 - 1) \frac{\alpha t}{C_p \theta \rho} \frac{W}{\pi a_0^2} e^{-r^2/a_0^2} \right] \tag{44}$$

and, with $n_0 \approx 1$,

$$\psi = \left[2 (n_0 - 1) \frac{\alpha t}{C_p \theta \rho} \frac{W}{\pi a_0^2} \right]^{1/2} e^{-r^2/2a_0^2} \cdot \tag{45}$$

Also

$$\frac{d\psi}{dr} = - \frac{r}{a_0^2} \psi \cdot \tag{46}$$

Now if $S(\psi)$ is the far-field radiant intensity,

$$S(\psi)\, 2\pi\psi (-d\psi) = P(r)\, 2\pi r\, dr \tag{47}$$

or

$$\psi S(\psi) \frac{d\psi}{dr} = -P(r)\, r\,, \tag{48}$$

and from Eq. (46)

$$\psi S(\psi) \left(- \frac{r}{a_0^2}\, \psi \right) = -P(r)\, r$$

or

$$S(\psi) = \frac{a_0^2}{\psi^2} P(r)\,. \tag{49}$$

Substituting for P and ψ from Eqs. (6) and (45) gives

$$S(\psi) = \frac{C_p \theta \rho\, a_0^2}{2(n_0 - 1)\, \alpha t} \tag{50}$$

with

$$0 \le \psi \le \left[2(n_0 - 1) \frac{\alpha t}{C_p \theta \rho} \frac{W}{\pi a_0^2} \right]^{1/2}$$

and $S(\psi) = 0$ elsewhere. The upper bound for ψ follows from Eq. (45) with $r = 0$. The rays from the point with greatest index change show the maximum angular deviation.

The far field is described as starting from a point of infinite intensity and spreading as a disk with radius proportional to $t^{1/2}$. The intensity within the disk is spatially uniform but varies with time as t^{-1}. In the far field the beam is radially inverted, or turned inside out. The edge of the beam is formed by the rays from the center of the initial beam, and ray crossing is complete.

When focusing is used, ray crossing may be induced in the near field, and in many situations the far-field equations will allow quick estimates of what to expect. An example is given below of the application of the far-field equations to the situation where the receiving area is smaller than the initial beam. Focusing is assumed.

When the received beam is smaller than the receiving area, the total beam power may be considered to be delivered. Let the receiving area be a disk of angular diameter 2ϕ. From Eq. (45) the beam will expand to the receiving area in time

$$t_1 = \frac{C_p \theta \rho \pi a_0^2 \phi^2}{2(n_0 - 1)\, \alpha W}\,, \tag{51}$$

and the total energy delivered at some subsequent time t will be

$$E = Wt_1 + \pi\phi^2 \int_{t_1}^{t} \frac{C_p \theta \rho a_0^2}{2(n_0 - 1)\alpha} \frac{dt}{t}$$

$$= Wt_1 + Wt_1 \log_e \frac{t}{t_1}, \quad t_1 < t$$

$$= Wt, \quad 0 \le t \le t_1$$

$$= Wt_1 \left(1 + \log_e \frac{t}{t_1}\right), \quad t_1 < t . \tag{52}$$

Letting

a_0 = 100 cm,

d = receiving diameter = 100 cm,

R = range = 10^6 cm, and

t_1 = 1 sec,

one has

$$\phi = 5 \times 10^{-5},$$

$$W = 1.5 \times 10^4 \text{ watts},$$

and

$$\begin{cases} E = 1.5\pi \times 10^4 t, & 0 \le t \le 1, \\ E = 1.5\pi \times 10^4 (1 + \log_e t), & 1 < t . \end{cases} \tag{53}$$

Equations (53) are plotted in Fig. 7. Energy on target increases linearly until the beam area equals the target area at time t_1. After t_1 the effect of thermal blooming slows energy deposition to a logarithmic increase with time.

ASYMPTOTIC BEHAVIOR OF THE MODEL EQUATION

The derivation of Eq. (39) insures that in the near field, i.e., as $z \to 0$, the predicted slopes and curvatures will be correct. It is easily shown that this description is asymptotically valid in the far field, i.e., as $z \to \infty$.

Applying Snell's law for a stratified medium gives

$$n \cos \beta_1 = n_0 \cos \beta_2 , \tag{54}$$

where n is the index at $z = 0$ and $r = a_0$, $\beta_1 = m$ is the initial slope of the profile ray, and β_2 is the far-field slope of the profile ray.

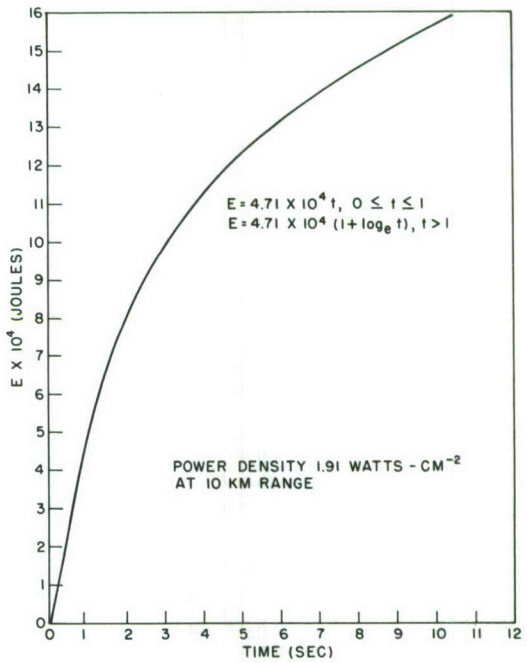

Fig. 7 - Received energy determined from far-field equations (power density of 1.91 watts-cm^{-2} at a 10-km range)

Expanding gives

$$n - \frac{nm^2}{2} = n_0 - \frac{n_0\beta_2^2}{2} \quad . \tag{55}$$

But from Eq. (11) for $r = a = a_0$

$$n_0 - n = \frac{(n_0 - 1)\,\alpha t W}{C_p \theta \rho \pi a_0^2 e} = \frac{k^2}{2\,a_0^2} \quad ; \tag{56}$$

so

$$\frac{n_0\beta_2^2}{2} = \frac{k^2}{2\,a_0^2} + \frac{nm^2}{2} \tag{57}$$

and, since $n_0 \approx n \approx 1$,

$$\beta_2 = \sqrt{\frac{k^2}{a_0^2} + m^2} \quad . \tag{58}$$

This is the asymptotic form of Eq. (39) as $z \to \infty$, i.e.,

$$\beta_2 = \lim_{3\to\infty} \frac{a}{z}$$

$$= \lim \left[\frac{k^2}{a_0^2} + \frac{(mz + a_0)^2}{z^2} \right]^{1/2}$$

$$= \sqrt{\frac{k^2}{a_0^2} + m^2}$$

CONCLUSIONS AND SUMMARY

A model equation (Eq. (39) has been derived to describe the phenomenon of thermal blooming in static air. The equation describes the path of a profile ray with the correct slope and curvature in the near field and the proper direction in the far field. In the intermediate field the solution to the ray path is approximate.

Aside from the approximations made in the derviation of the model equation, which should not invalidate qualitative or rough quantitative predictions, one important environmental assumption is made. This is the assumption of no wind and static air, which represents the worst situation from the standpoint of thermal blooming. The figures obtained for static air will be extreme numbers that can serve as references for the improvement due to wind. The static air solution is a transient solution involving time. When wind is present, it will be more convenient to look for steady state solutions. This will be done in a future report.

REFERENCES

1. J.P. Gordon, R.C.C. Leite, R.S. Moore, S.P.S. Porto, and J.R. Whinnery, Amer. Phys. Soc. Bulletin 9, 501 (1964)

2. R.C.C. Leite, R.S. Moore, and J.R. Whinnery, Appl. Phys. Letters 5, 141 (1964)

3. J.P. Gordon, R.C.C. Leite, R.S. Moore, S.P.S. Porto, and J.R. Whinnery, J. Applied Phys. 36, 3 (1965)

4. K.F. Rieckoff, Applied Physics Letters 9, 87 (1966)

5. R.C. Leite, S.P.S. Porto, and T.C. Damen, Applied Physics Letters 10, 100 (1967)

6. W.R. Callen, B.G. Huth, and R.H. Pantelle, Applied Physics Letters 11, 103 (1967)

7. S.A. Akhamanov, D.P. Krindach, A.P. Sukhorukov, and R.V. Khophlov, Zh ETF Pis. Red. 6, 509 (1967) (JETP Letters 6, 38 (1967)

8. J.R. Whinnery, D.T. Miller, and F. Dabby, J. Quantum Electr. 3, 382 (1967)

9. L.R. Carman and P.L. Kelley, Applied Physics Letters 12, 241 (1968)

10. H. Inaba and H. Ito, J. Quantum Electr. QE-4, 45 (1968)

11. E.A. McLean, L. Sica, and A.J. Glass, Applied Physics Letters 13, 369 (1968)

12. F.G. Gebhardt and D.C. Smith, Applied Physics Letters 14, 52 (1969)

13. Born and Wolf, "Principles of Optics," 1959, p. 123.

Appendix

FAR FIELD WITH FINITE APERTURE

The far-field pattern refers to the directional intensity distribution of the aperture considered as a point source, and, since diffraction is being neglected, it is here generated solely by the geometrical optics of the heated atmosphere. The detailed distribution in the far field is expected to be a function of the radial power distribution at the aperture. The far field for a radial Gaussian distribution has been found to be a disk of uniform spatial intensity but starting as a point and spreading in time. It will be of interest to examine the far field for another functional distribution of power density and in particular for a distribution that sharply defines a finite aperture. Let

$$\begin{cases} P = P_0 \left(1 - \dfrac{r^2}{r_0^2}\right), & r \le r_0 \\ P = 0, & r > r_0 \end{cases} \tag{A1}$$

where r_0 is the radius of a finite aperture.

In place of Eq. (45) we will now have

$$\psi^2 = 2 (n_0 - 1) \frac{\alpha t}{C_p \theta \rho} P_0 \left(1 - \frac{r^2}{r_0^2}\right) \tag{A2}$$

or, with

$$K = \frac{2 (n_0 - 1) \alpha t}{C_p \theta \rho} ,$$

$$\psi^2 = K P_0 \left(1 - \frac{r^2}{r_0^2}\right) = KP , \tag{A3}$$

which, when differentiated with respect to r, gives

$$\psi \frac{d\psi}{dr} = - \frac{K P_0 r}{r_0^2} . \tag{A4}$$

Equation (48) still applies, i.e.,

$$S(\psi) \psi \frac{d\psi}{dr} = -P(r) \, dr ,$$

and making use of Eq. (A4) gives

$$S(\psi)\left(-\frac{KP_0 r}{r_0^2}\right) = -\frac{\psi^2}{K} r \tag{A5}$$

or

$$S(\psi) = \frac{r_0^2}{K^2 P_0}\psi^2 , \tag{A6}$$

where from Eq. (A2)

$$\psi_{max} = (KP_0)^{1/2} .$$

To compare Eqs. (A5) and (A6) with Eq. (50) let a_0 be related to r_0 so that beam power W and maximum power density P_0 are the same for the two distributions. For the finite aperture,

$$W = 2\pi \int_0^{r_0} Pr\, dr$$

$$= 2\pi P_0 \int_0^{r_0} \left(r - \frac{r^2}{r_0^2}\right) dr \tag{A7}$$

or

$$W = \frac{\pi P_0 r_0^2}{2} .$$

For the Gaussian aperture it has been shown that

$$W = \pi P_0 a_0^2 , \tag{A8}$$

and the condition for matching W's and P_0's is that

$$a_0^2 = \frac{r_0^2}{2} . \tag{A9}$$

Rewriting Eq. (50) in terms of K and r_0 gives for the Gaussian distribution

$$\begin{cases} S(\psi) = \dfrac{a_0^2}{K} = \dfrac{r_0^2}{2K} , & 0 \le \psi \le \sqrt{KP_0} \\ S(\psi) = 0 , & \psi > \sqrt{KP_0} \end{cases} \tag{A10}$$

and for the finite aperture

$$\begin{cases} S(\psi) = \dfrac{r_0^2}{K^2 P_0}\,\psi^2 , & 0 \le \psi \le \sqrt{KP_0} , \\ S(\psi) = 0 , & \psi > \sqrt{KP_0} , \end{cases} \tag{A11}$$

where in each case

$$K = \frac{2\,(n_0 - 1)\,\alpha t}{C_p \theta \rho} .$$

At the same instant of time, it is seen that the far-field disks have the same diameters as expected but that the intensity within the disk is not uniform for the finite aperture. It varies as ψ^2 from $S = 0$ for $\psi = 0$ to $S = r_0^2/K$ for $\psi = \sqrt{KP_0}$. The disk edge intensity is thus twice the uniform value of intensity found for the Gaussian distribution.

Appendix C
[Unclassified]

EQUILIBRIUM TEMPERATURES

W. R. Faust
Applications Research Division

INTRODUCTION

Studies have been made of the thermal defocusing and other problems associated with the propagation of intense laser beams through the atmosphere (Appendix B). As is well known a small fraction of the energy is absorbed in the air, which causes local heating and a subsequent change in the refractive index and so alters the propagation. During the initial stages after the beam is turned on the heated air starts to move from the neighborhood of the beam due to the resultant pressure gradient and ultimately will achieve some sort of steady state.

The problem considered here is to calculate the equilibrium temperature of the atmosphere in the beam a long time after the beam has been turned on. To simplify the problem it will be assumed that the beam has a Gaussian shape, e^{-r^2/a^2}. The parameter a, of course, depends on the distance z along the beam. Another simplifying assumption is to neglect convective effects. This is equivalent to setting the volume force $\mathbf{g}$ due to gravity equal to zero in the equations of motion. This procedure, while neglecting an important physical process, provides an estimate of the limiting conditions in the beam.

EQUILIBRIUM CONDITIONS

The general energy equation for a fluid (Ref. C1) is

$$C_p \rho \left(\frac{\partial T}{\partial t} + \mathbf{V} \cdot \nabla T \right) = \nabla \cdot (k \nabla T) + S \ ,$$

where

T = temperature, °K,

ρ = density, g/cm^3,

C_p = specific heat at constant pressure, ergs/g,

V = velocity, cm/sec,

k = coefficient of heat conduction,

$S = \alpha P_0 \ e^{-r^2/a^2}$ = source,

α = absorption coefficient, cm^{-1},

P_0 = watts/πa^2 = peak power flux in the beam, W/cm^2.

As a starting point it will be assumed that the beam is Gaussian in shape at a given point along the beam. If equilibrium is assumed, then

$$\frac{\partial T}{\partial t} = V = 0 ,$$

so that

$$\nabla \cdot (k \nabla T) = -\alpha P_0 \, e^{-r^2/a^2} .$$

Kinetic gas theory yields the result that (Ref. C2)

$$k = \beta \sqrt{T} = 150 \sqrt{T} \text{ ergs/cm}^2\text{-sec (for air)} .$$

If it is assumed that energy is deposited uniformly along the beam, then

$$\frac{\beta}{r} \frac{\partial}{\partial r} \left(r \sqrt{T} \frac{\partial T}{\partial r} \right) = -\alpha P_0 \, e^{-r^2/a^2} .$$

Let $\theta = T^{3/2}$, then

$$\frac{1}{r} \frac{\partial}{\partial r} \left(r \frac{\partial \theta}{\partial r} \right) = - \frac{3 \alpha P_0}{2 \beta} e^{-r^2/a^2} ,$$

from which

$$r \frac{\partial \theta}{\partial r} = \frac{3 \alpha P_0 a^2}{4 \beta} e^{-r^2/a^2} + C_0 .$$

Now

$$r \frac{\partial \theta}{\partial r} = 0 \text{ at } r = 0 ,$$

so that

$$\frac{\partial \theta}{\partial r} = - \frac{3 \alpha P_0 \, a^2}{4 \beta} \frac{1 - e^{-r^2/a^2}}{r}$$

and

$$\theta = \theta_0 + \frac{3 \alpha P_0 \, a^2}{4 \beta} \int_r^\infty \frac{1 - e^{-r^2/a^2}}{r} \, dr ,$$

where $\theta \to \theta_0 = T_0^{3/2}$ as $r \to \infty$, and T_0 is the temperature a great distance from the beam. Then

$$T = T_0 \left[1 + \frac{3\alpha P_0 a^2}{4 T_0^{3/2} \beta} \int_r^\infty 1 - e^{-r^2/a^2} \frac{dr}{r} \right]^{2/3}$$

$$= T_0 \left[1 + \frac{3\alpha P_0 a^2}{8 T_0^{3/2} \beta} \int_{r^2/a^2}^\infty (1 - e^{-y}) \frac{dy}{y} \right]^{2/3} .$$

ULTIMATE TEMPERATURE

It can be shown (Ref. C3) that

$$\int_z^\infty (1 - e^{-y}) \frac{dy}{y} = C - \ln Z + E_i(-z) ,$$

where $C = 0.5772$ is Euler's constant. By comparison of expansion (for small z) of the exponential integral it can be shown that the above integral is C for $z = 0$. It follows that the temperature in the beam is

$$T = T_0 \left(1 + \frac{3\alpha P_0 a^2 C}{8 T_0^{3/2} \beta} \right)^{2/3} .$$

If it is assumed that

$P_0 = 4.77 \times 10^2$ watts/cm^2 $= 4.77 \times 10^9$ ergs/cm^2-sec,

$\alpha = 10^{-6}$ cm^{-1},

$\beta = 150$ ergs/cm^2-sec-°K$^{1/2}$,

$a = 10$ cm^{-1},

the then ultimate temperature is

$T = 297$°K $= 24$°C.

This represents the maximum possible temperature in the beam, or a temperature increase of 24°C as compared with the temperature at infinity ($T_\infty = 0$°C).

REFERENCES

C1. L.D. Landau and E.M. Lipshitz, "Fluid Mechanics," Addison-Wesley, 1959, pp. 183 et seq.

C2. S. Chapman and T.G. Cowling, "Mathematical Theory of Non-Uniform Gases," Cambridge, 1961, p. 241.

C3. H. Jeffreys and B.S. Jeffreys, "Mathematical Physics," 3rd edition, Oxford Press, 1956, p. 470.

Appendix D
[Unclassified]

SUPRESSION OF THERMAL BLOOMING BY WIND

Herbert B. Rosenstock
Solid State Division

Consider a light beam of radius a cm which, on account of absorption, heats the atmosphere it traverses. Let v cm/sec be the velocity component of the wind that is perpendicular to the beam. We want to calculate an upper limit to the temperature increase that results.

Let P cal/sec be the power of the beam, and let α cm^{-1} be the absorption coefficient. Then αP cal/cm-sec will be absorbed in the entire beam, and $\alpha P/\pi a^2$ cal/cm^3-sec will be absorbed by a unit volume, and if ρ g/cm is the density of air, then $\alpha P/\pi a^2 \rho$ cal/g-sec will be absorbed by a unit mass. If C_p cal/g-°C is the specific heat of the gas, this will lead to a temperature increase

$$\Delta T = \alpha P/\pi a^2 \rho C_p \ ^\circ C/sec \ .$$

Now a volume element of air just entering the beam at time zero will have entirely passed through the beam in $\tau = 2a/v$ sec (most air volumes moving with the wind will pass through the beam in less time). The time τ sec is therefore an upper limit to the time during which any heating can actually take place, and the maximum temperature increase is therefore

$$\Delta T = 2\alpha P/\pi a \rho C_p v \ ^\circ C \ .$$

Let us put some numbers into this. For air, we use

$$\alpha = 8 \times 10^{-7} \ cm^{-1} \ ,$$

$$C_p = 0.24 \ cal/^\circ C\text{-}g \ ,$$

$$\rho = 1.3 \times 10^{-3} \ g/cm^3 \ .$$

For the beam radius we take

$$a = 25 \ cm \ ,$$

for the beam power we take 150 kW, which in the desired units becomes

$$P = 3.6 \times 10^4 \ cal/sec \ ,$$

and for the wind velocity we take 10 knots, or

$$v = 5.1 \times 10^2 \ cm/sec \ .$$

This yields for the maximum temperature increase due to heating the beam

$$\Delta T = 4.6 \times 10^{-3} \ ^{\circ}\mathrm{C} \ .$$

This is a very small number, compared, for example, to the natural irregularities in the atmosphere. (For the absence of wind, Faust (Appendix C) has recently obtained a much higher estimate, 24°C.) In preparing a list of factors that might spoil collimation of the beam, atmospheric heating by the beam itself (blooming) would therefore appear to be of secondary or even negligible importance compared to turbulence, and possibly nonlinear optical effects. Conversely, this implies that if wind is present, experimental results, for "low"-power beams should be quite relevant to such "high"-power beams as well.

Appendix E
[Unclassified]

MEASUREMENT OF ATMOSPHERIC METEOROLOGICAL PARAMETERS

E. F. Ditzel and H. Shenker
Optical Sciences Division

INTRODUCTION

The phase of the program reported in this appendix concerns the measurement of various meteorological parameters which are pertinent to the propagation of radiation in the lower atmosphere. The effort to date has been concentrated on the investigation of water vapor concentration along potential optical paths 9 and 18.5 feet above the water surface. These paths are in the Chesapeake Bay and are 2.0, 2.5, and 9.0 statute miles in length.

METHODS

Two methods to measure the water vapor content of the atmosphere have been investigated. One is based on the psychrometer method of measuring wet and dry bulb temperatures. In this case the sensors are platinum resistance thermometers, where the wet bulb is moistened by a water-wick arrangement and the other sensor measures the ambient dry bulb temperature. A blower maintains an air-flow velocity of 900 ft/min over the sensors, which are mounted in an over and under configuration. A shipboard psychrometer consisting of the sensors and blower and an 18.5-foot-high intake stack has been mounted on a small boat. The intake stack may be partially dismounted to provide a 9-foot intake level. The readout for the psychrometer is a multipoint Leeds and Northrup Speedomax A Recorder calibrated to read temperature. A portion of the output signal is fed to a Varian Recorder to produce an expanded running profile of the difference between the wet and dry bulb temperatures.

The other method is the dew point determination of the water vapor content of the atmosphere. We have used a model 137-C3 hygrometer manufactured by Cambridge Systems. This device contains a thermoelectrically cooled mirror, a light source, a sensor for measuring the mirror temperature, sensors for measuring the scattered light intensity, and a feedback system for maintaining a constant thickness of dew on the sensing mirror. The output of the hygrometer is fed to a strip chart recorder producing a convenient readout of the dew point temperature. This equipment has been recalibrated by the manufacturer and has been installed on the boat adjacent to the psychrometer equipment. Because of operational difficulties such as maintaining the proper air flow, the equipment is not yet operational. The experimental data reported here was obtained by the psychrometer method only.

Figure E1 is a view of the psychrometer mounted on the deck of the NRL J-boat. On its base plate is mounted the control unit of the hygrometer, whose sensor is located at the top of the intake stack of the psychrometer.

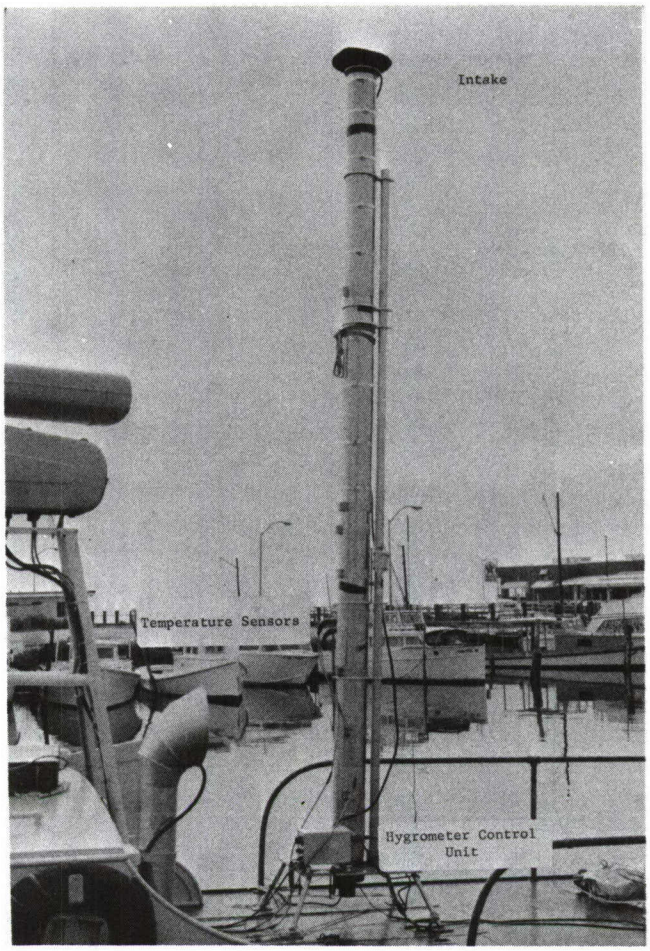

Fig. E1 - Psychrometer equipment mounted on NRL J-boat

RESULTS

The humidity was monitored over three paths. The actual path lengths traveled by the boat were: a 9.0-mile path between Building 5, CBD, and Tilghman Island; a 2.5-mile path between Building 5, CBD, and Clark's platform; and a 2.0-mile path from the boathouse about 0.5 mile south of Building 5, CBD, to Clark's platform.

Figure E2 shows the data from a run made on 11 September 1969 over a path beginning at a point 0.5 mile offshore near Building 5 and terminating 0.25 mile offshore opposite the NRL tower at Tilghman Island. Weather conditions were fair with a 4 to 10 knot easterly breeze. The solid line is the record for the west-to-east pass across the Chesapeake Bay using the 18.5-foot sampling level. The dashed curve represents the data for the east-to-west run using the 9.0-foot sensing level. The average water vapor content for the 9.0-foot level was about 7.0 $\mu g/cm^3$, while at the 18.5-foot level the average value is about 14 percent higher, 8.0 $\mu g/cm^3$. Ambient temperatures are plotted at the top of the figure; it is noted that the temperature for the 18.5-foot level is more uniform and lower than for the 9.0-foot level.

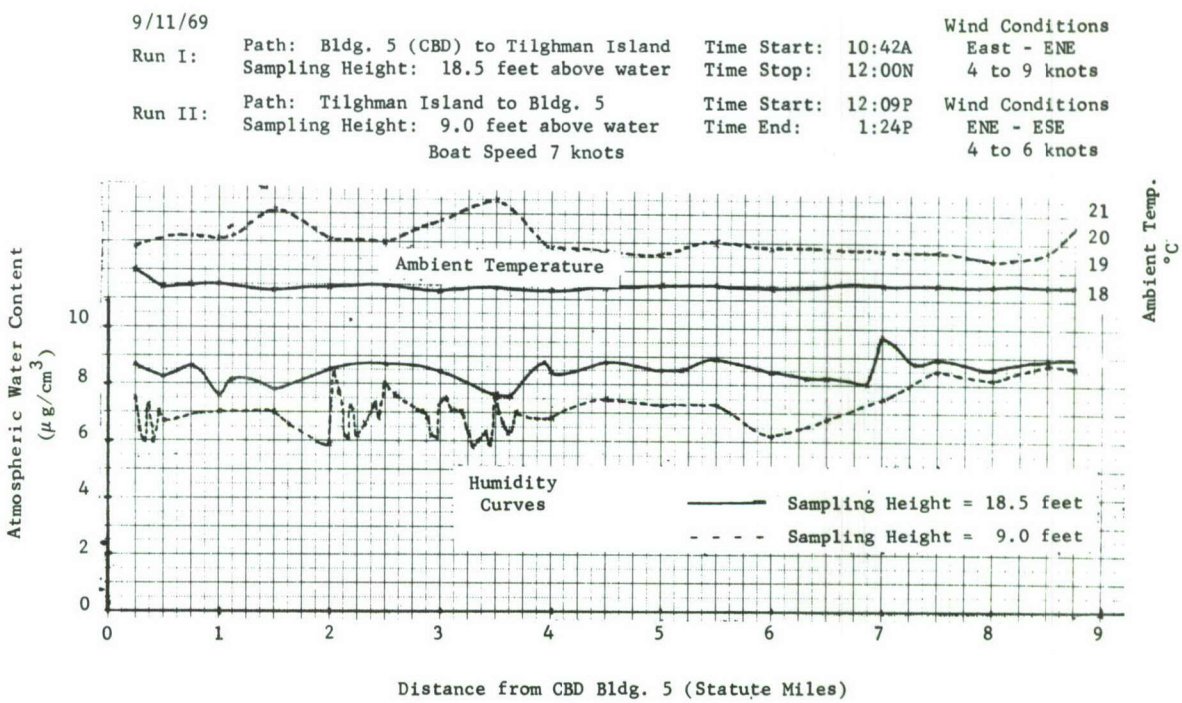

Fig. E2 - Humidity and temperature data from a run made on 11 September 1969, Building 5, CBD, to Tilghman Island, with an east wind of 4 to 10 knots

Figure E3 shows the water vapor and ambient temperature profile between Building 5 and Tilghman Island under a brisk northeast wind of 6 to 12 knots on 25 September 1969. At the 18.5-foot level the water content averages about 14 $\mu g/cm^3$. This is 75 percent greater than the 8.0 $\mu g/cm^3$ obtained under the mild condition of a 4-knot wind shown in Fig. E2. Both sampling levels in Fig. E3 show a relatively constant value for the humidity, with the 9.0-foot level being slightly higher than the 18.5-foot level. This represents an inversion of the results shown in the previous figure. The ambient temperatures are relatively uniform, where again, as in Fig. E2, the 9.0-foot level is slightly warmer.

Figure E4 shows a run made on 7 October 1969 between Clark's platform and Building 5, CBD. A brisk wind, 8 to 16 knots, was blowing from the south up the Bay, providing a rough water condition. The solid line shows the water-content profile at the 18.5-foot level when the run was into the wind. The less stable dashed curve is from the downwind run, where the intake was at the 9.0-foot level. The water content was high, averaging about 16.0 $\mu g/cm^3$ at the 18.5-foot sampling level.

Figure E5 shows a record of humidity versus time made during relatively calm conditions when the boat was anchored at Clark's platform. In this situation the 18.5-foot sampling height shows greater temporal variations of water vapor content, although the average for 15 minutes seems to be the same for the two intake heights.

CONCLUSIONS

In general, data from the higher sampling level show a more constant humidity profile over a given path. Motion of the boat into the wind produces a more stable humidity profile, particularly under conditions of strong wind and high humidity.

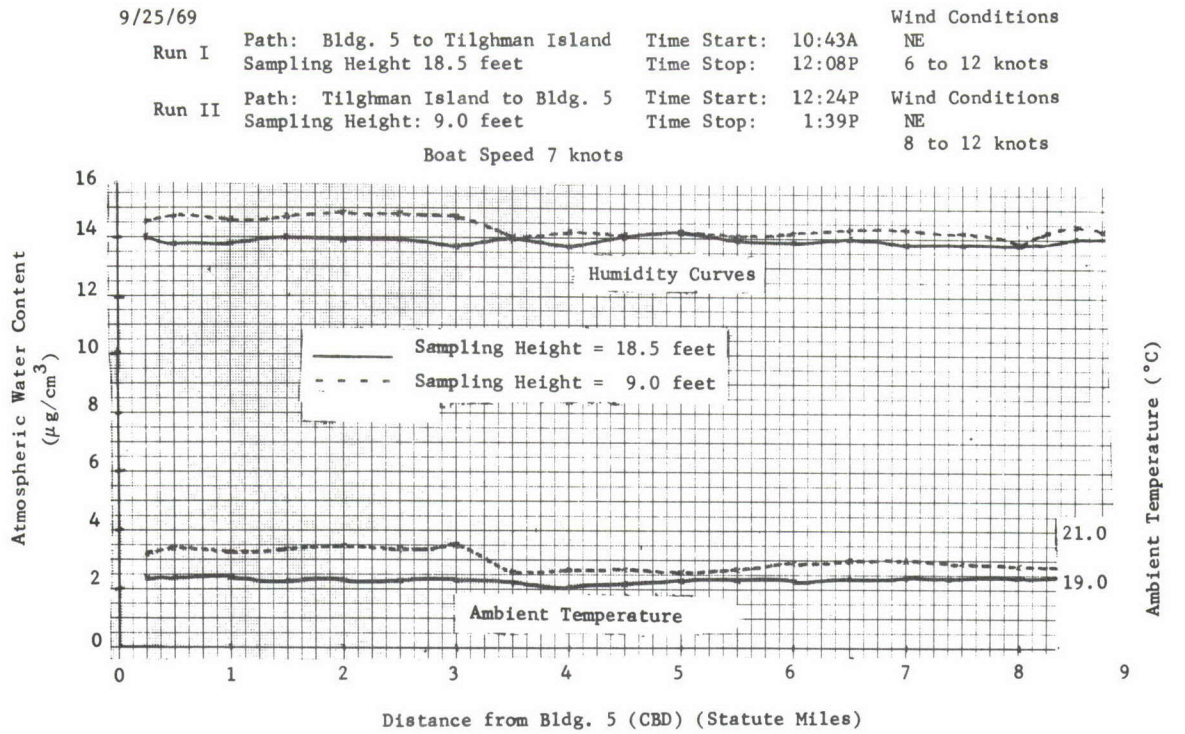

Fig. E3 - Humidity and temperature data from a run made on 25 September 1969, Building 5, CBD, to Tilghman Island, with a northeast wind of 6 to 12 knots

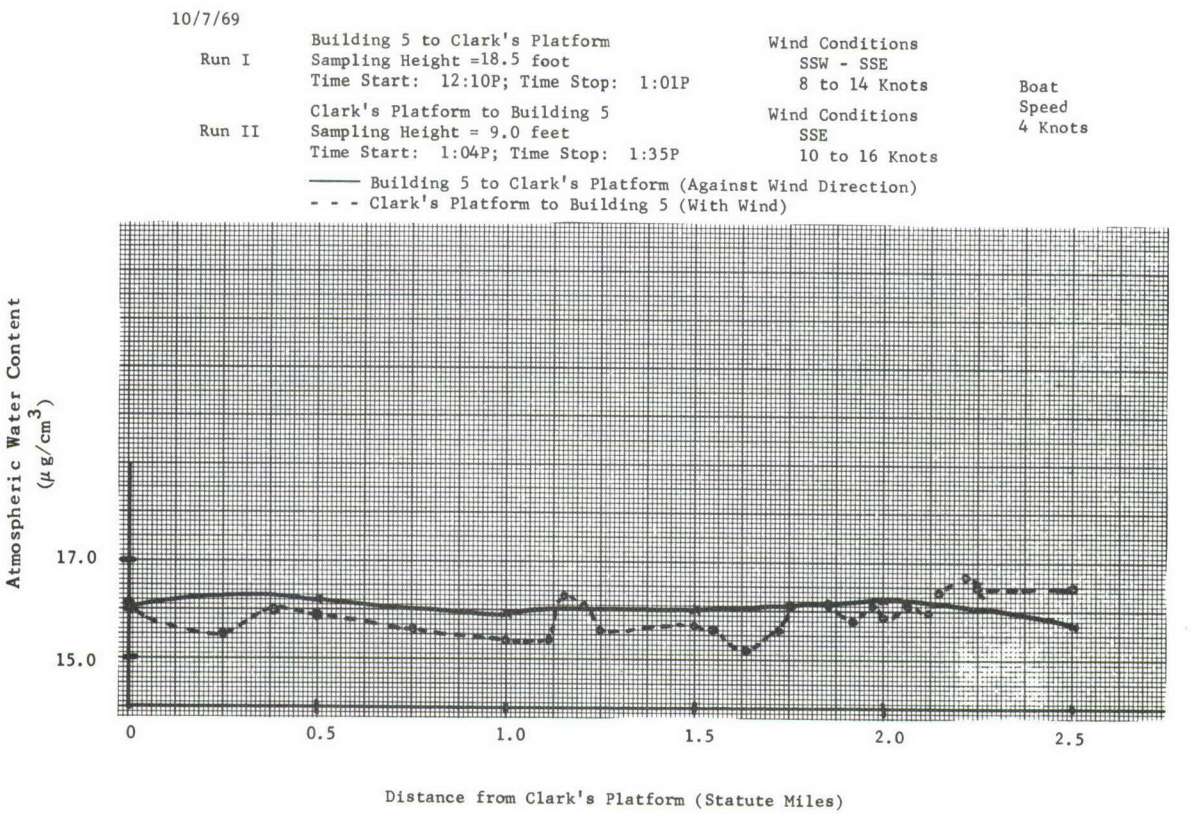

Fig. E4 - Humidity and temperature data from a run on 7 October 1969 between Clark's platform and Building 5, CBD, with a southerly wind of 5 to 16 knots

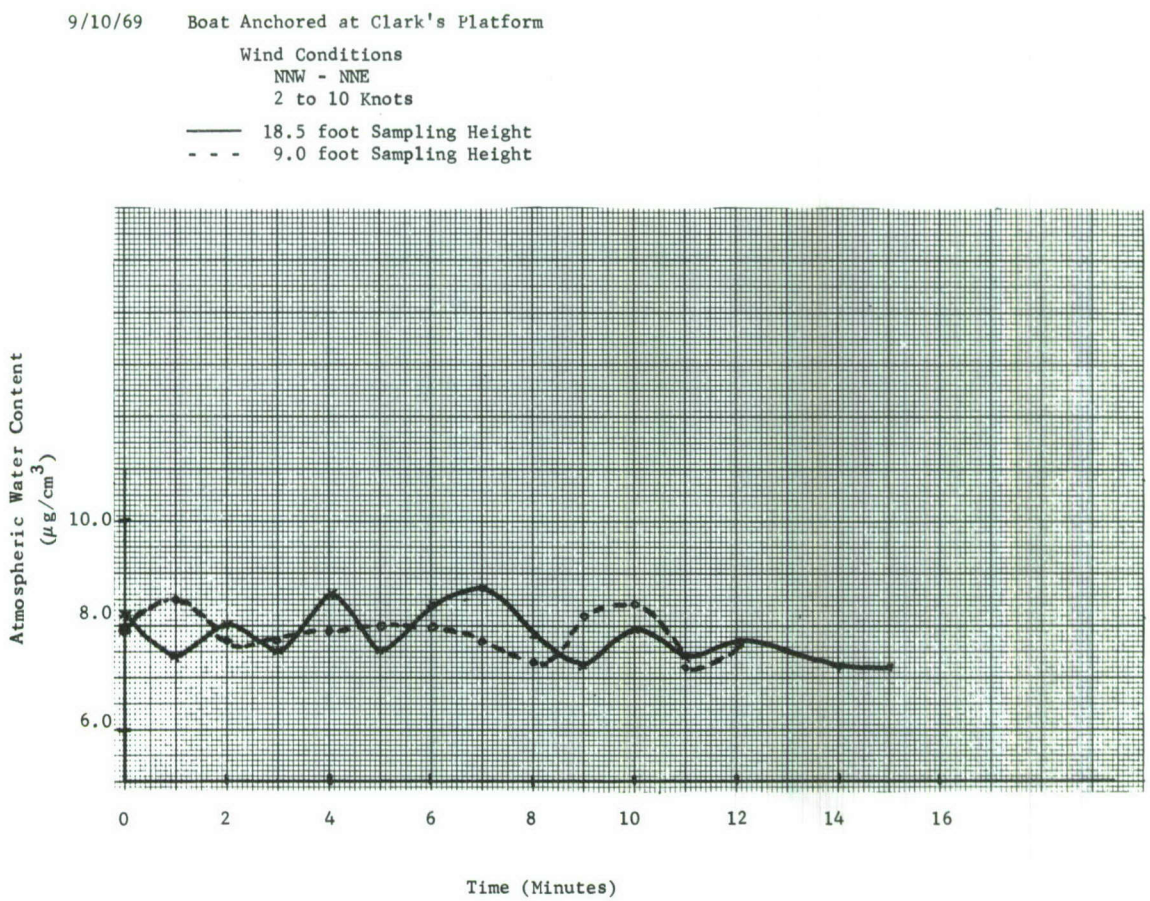

Fig. E5 - Humidity as a function of time recorded while anchored at Clark's platform under calm conditions

It seems probable that some of the data taken at the 9.0-foot level have been affected by possible heating and water vapor contributions from the wooden boat deck and from the engine exhaust spray, which may account in part for the higher temperatures observed at the 9.0-foot level. As a consequence of this possibility, the experimental arrangement is being modified so that the air intake will be ahead of the boat, well removed from any possible spray or thermal influence by the boat.

FUTURE PLANS AND ACTIVITY FOR MEASUREMENT OF ATMOSPHERIC METEOROLOGICAL PARAMETERS

To remove any humidity and temperature contributions from the boat deck and engine exhaust the sampling instrumentation is being redesigned so that samping will occur at a point 20 to 30 feet ahead of the boat. Provision will be made to make humidity profiles up to 30 feet above the water surface. Humidity profile runs will be concurrent with laser propagation measurements over any of the overwater paths. A rapid response microthermometer system for sensing instantaneous temperature differences in the atmosphere has been purchased and is currently undergoing acceptance tests. This instrument will be used to directly measure the strength of atmospheric turbulence along the paths being used for laser propagation studies.

Appendix F
[Unclassified]

ATMOSPHERIC LASER PROPAGATION MEASUREMENTS

J. A. Dowling, J. A. Curcio, and H. Shenker
Optical Sciences Division

PROCEDURE

A propagation test range has been set up at CBD to study the effects of atmospheric turbulence on laser beam transmission. This facility consists of an environmentally controlled building housing both the laser transmitter and receiver in addition to signal processing and analysis equipment. A 16 by 24 inch plane mirror on a precision mount supported on a concrete pedestal is located at the opposite end of the range. The mirror is enclosed by hinged doors when experiments are not in progress. This range is illustrated in Fig. F1. The atmospheric path available is approximately 2200 feet. As shown in Fig. F1 the maximum variation of beam height above the underlying surface is approximately 2 percent of the path length. The line of sight crosses grassy terrain with the exception of a road and concrete test pit near the return mirror. Two monitoring stations are used to record air temperature, humidity, wind velocity, and direction and are located adjacent to the path as shown in Fig. F1.

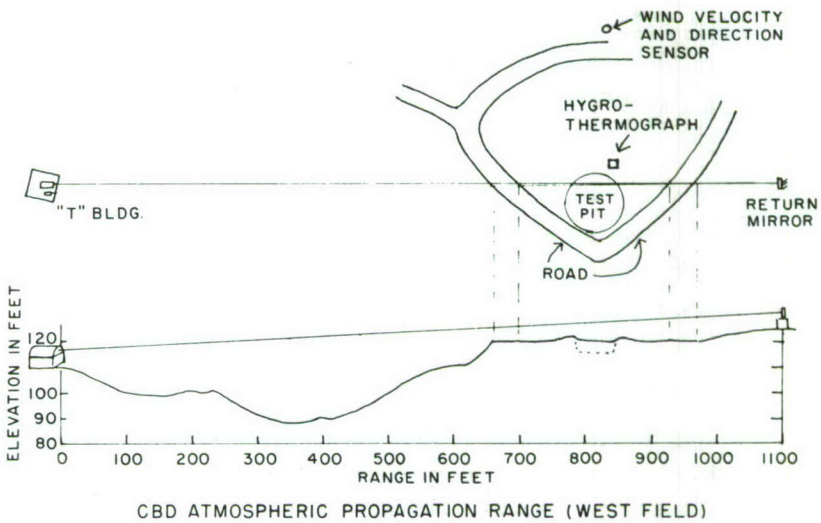

Fig. F1 - CBD laser propagation range

A 633.-nm He-Ne laser has been used during initial experiments over this range. The laser output (nominally 3 mW) is focused, spatially filtered, and recollimated using a telescope in front of the laser. The exit beam is roughly 2.0 inches in diameter with a divergence of approximately 0.2 milliradian or about 2.5 inches for each half of the

2200-foot folded path. At times when there is a temperature difference between the outside air and the air inside the laser-receiver building (T building), appreciable turbulent activity may be anticipated immediately in the vicinity of the laser beam exit port in the side of the building. Although no quantitative determination of these effects has been made, nevertheless a window of optical quality has been installed in this port. The receiver port is used just as an uncovered opening. Any effects at the transmitter port would be exaggerated by the lever arm of the entire path, while beam direction changes at the receiver port are multiplied by only a 4-foot lever arm.

The receiver used during the initial experiments over this path is illustrated in Fig. F2. The main components are: an f/4 objective lens of 50 cm focal length, a field stop located at the paraxial focus of the lens which limits the receiver field of view to 6 milliradians, a narrow bandpass interference filter of approximately 1 nm spectral bandpass slightly inclined to the telescope axis so as to center its bandpass at the laser wavelength, and an S-20 2-inch-end-window photomultiplier detector. The receiver as well as the laser transmitter are mounted on precision-screw-actuated tables, providing precise adjustments for azimuth and elevation.

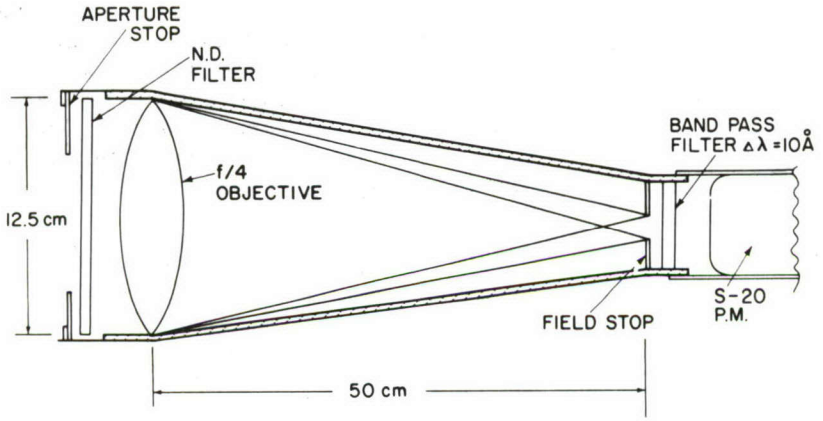

RECEIVER OPTICS

Fig. F2 - Laser receiver

The signal processing and recording electronics used during initial experiments are illustrated in block diagram form in Fig. F3 and consist of: a logarithmic converter directly connected to the photomultiplier detector, an analog instrumental tape recorder used in the FM mode at 7-1/2-inch/second record and playback, an averaging voltmeter, and an 0.1 to 500 kHz rms voltmeter. The response of the logarithmic converter has been checked by inserting a series of calibrated test currents (10^{-9} to 10^{-5} amperes) at the input. The output voltage was within 1 percent of the expected nominal value for a 1-percent tolerance on the input current, where the nominal output voltage e_o is obtained from the relationship

$$e_o = -2 \log_{10} \frac{i_{in}}{10^{-8} \text{ amp}} \text{volts} .$$

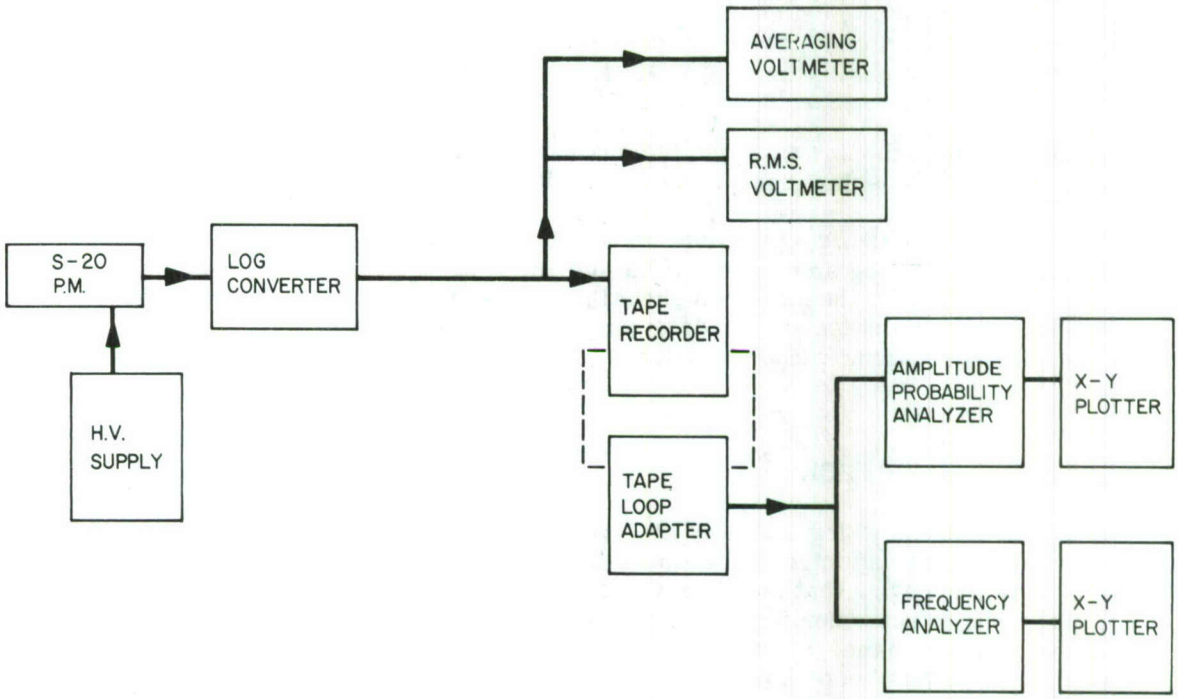

Fig. F 3 - Signal processing

Initial investigations of the amplitude and frequency statistics of the time-varying receiver signal have been made. A series of aperture stops have been used to investigate the dependence of the signal statistics on receiver aperture. A set of five stops having diameters of 1, 5, 10, 50, and 100 mm was used. These were compensated by including neutral-density filters whose optical density increased as the ratio of the aperture area so that the average signal level remained approximately constant.

A signal history of 60 seconds was recorded on tape for each aperture. The time required to change apertures and record sufficient data on tape for the series of five apertures was approximately 7 minutes. It is assumed that the atmospheric statistics were fairly constant during this time. The portion of tape corresponding to each aperture was then cut and formed into a loop. Each loop consisted of 30 seconds of signal. The loop was then played back continuously, using a loop adapter on the tape recorder, and analyzed. The amplitude probability analysis was performed by playing the tape loop record for each aperture into a Quan Tech Model 317B probability analyzer. This device provides an output proportional to the amount of time that the signal amplitude exceeds a slowly increasing threshold level. The analyzer output of cumulative probability versus log intensity was then displayed on an xy recorder.

The frequency analysis of the data was made by playing the same tape loop into a Quan Tech Model 304 frequency analyzer. The output of this instrument was similarly displayed on an xy recorder as a record of relative log intensity versus frequency.

The intensity distribution data have been plotted on probability paper. This paper has one nonlinear axis, symmetrical about the point $y = 0.5$ and scaled such that the quantity

$$y = \frac{1}{\sigma\sqrt{\pi}} \int_{-\infty}^{z} e^{-z^2/\sigma^2}\, dz$$

will graph as a straight line when plotted against z on the other linear axis. Thus, a normally distributed (Gaussian) random variable will plot as a straight line.

Due to the logarithmic operation the waveform being analyzed is an analog of the log intensity or twice the log amplitude. If the log amplitude is a normally distributed random variable (Refs. F1-F3), then the data should plot as a straight line on probability paper. In addition, electrical noise and/or detector nonlinearities, if present, are made apparent by deviations from straight line plots at the low and high signal amplitude extremes respectively.

RESULTS AND DISCUSSION

The distributions of log intensity (2 × log amplitude) versus cumulative probability for different receiver apertures are shown in Figs. F4 and F5. The results plot as straight lines, indicating that the observed scintillations are log-normal and that electrical noise and detector nonlinearities are not serious. No systematic dependence of the log amplitude variance σ_ℓ (which is proportional to the slopes of these lines) upon receiver aperture has been observed in these data. The data in Fig. F4 yield values of 0.2 to 0.4 for σ_ℓ, with the maximum values occurring for the 5 and 10 mm apertures. The data in Fig. F5 yield values for σ_ℓ between 0.02 and 0.1 and are generally independent of aperture size.

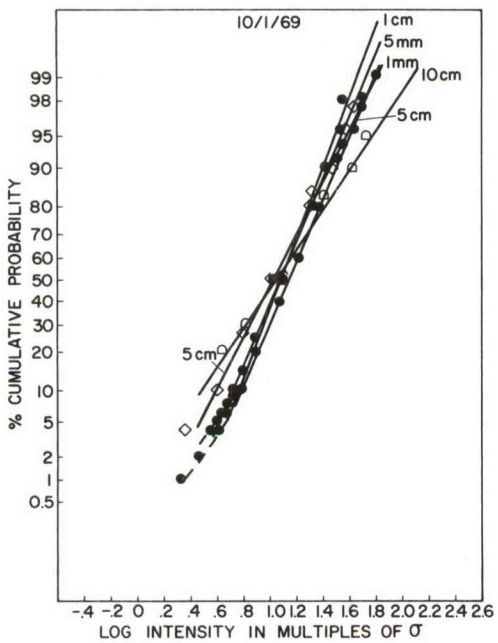

Fig. F4 - Cumulative probability versus log intensity for received laser signal, 12 September 1969

We plan to calibrate the rms voltmeter readout using test signals with known variance in order to have an independent determination of σ_ℓ during future measurements. It is felt that a second control receiver with fixed aperture would be very useful in

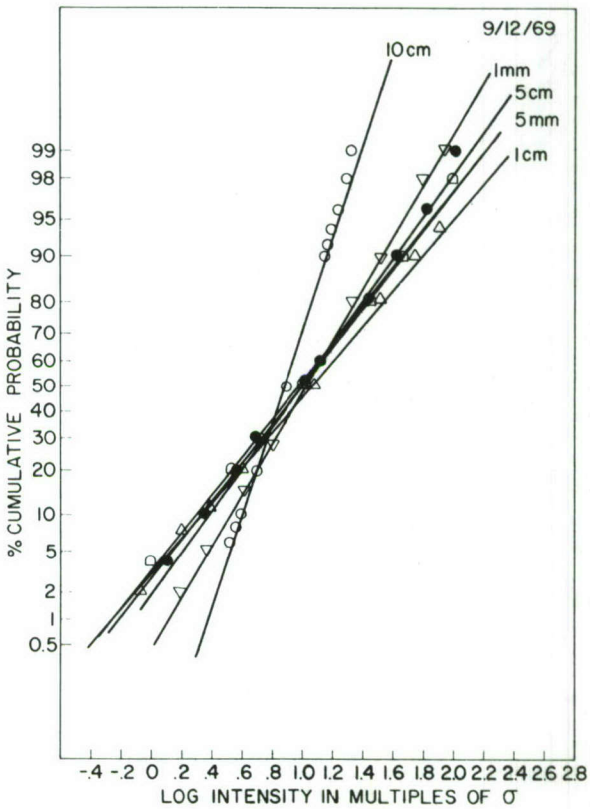

Fig. F5 - Cumulative probability versus log intensity for received laser signal, 1 October 1969

normalizing results such as those shown in Figs. F4 and F5 so that the nonstationary behavior of the atmospheric statistics may be taken into account.

The amplitude distribution data obtained thus far are considered insufficient insofar as specifying the dependence of σ_ℓ upon receiver aperture; however, the data do indicate that the dynamic range in the detection electronics is adequate.

Typical frequency spectra are illustrated in Figs. F6 through F8. The data have been plotted as relative log intensity versus frequency on log-linear coordinates. For frequencies $\gtrsim 10$ Hz the data are well fitted by the functional dependence $\ln I/I_0 \approx e^{-\alpha f}$ with two exceptions, namely, the curve for the 5-cm aperture in Fig. F7 and the data shown in Fig. 8. These two spectra were taken under conditions of relatively low scintillation. An exponential decay constant α has been determined for each of the remaining curves which do agree with the above expression. This empirically derived quantity is plotted as a function of aperture diameter in Fig. F9. This plot shows a systematic increase of α with increasing aperture, although the functional dependence upon aperture size is not consistent for the two sets of data. Some attempts will be made to compare these observations to theoretical predictions of scintillation spectra (Ref. F1); however more data should be taken before any conclusions are inferred from these results.

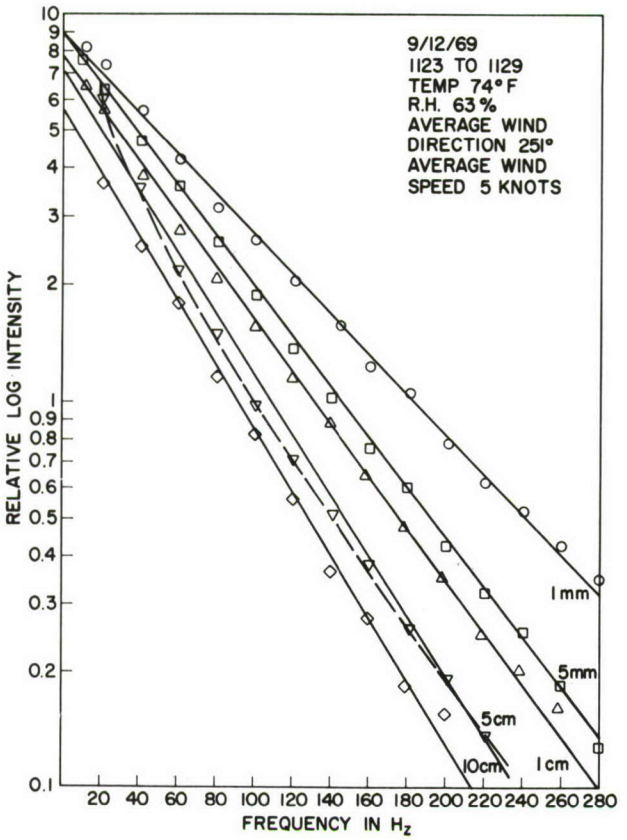

Fig. F6 - Relative log intensity versus frequency for received laser signal, 12 September 1969

STATUS AND PLANS FOR LASER PROPAGATION MEASUREMENTS

With our present experimental program we are developing a capability and familiarity with measurement and analysis of intensity fluctuations in laser beams propagated through atmospheric turbulence. The dependence of these phenomena upon atmospheric conditions and the particular features imposed by a maritime atmosphere are subjects of investigation.

This work has been started using a visible laser and an overland path. The effort will be shifted to overwater measurements at 10.6 μm as soon as is practical. A sensitive, fast-response HgCdTe infrared detector is available for measurements using a 100-watt multimode CO_2 laser. A stable, single-mode CO_2 laser will soon be available.

Additional measurements planned for the immediate future using the visible laser include rapid sequential photographs of the entire beam incident on a reflecting screen or collector mirror. We plan to make simultaneous spatial frequency measurements from the photographs and photoelectric correlation measurements, thereby establishing the equivalence of these two types of information. The two-point correlation measurements can then be carried over into the infrared with confidence.

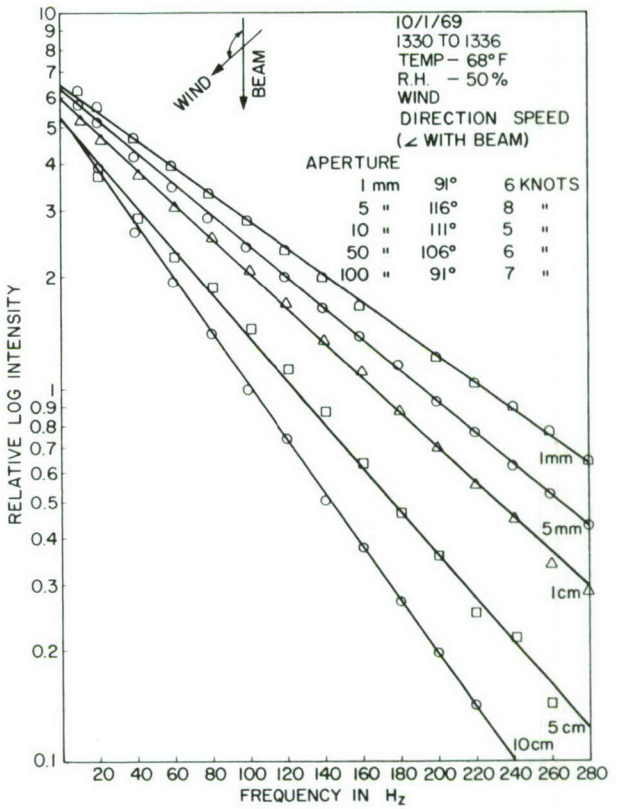

Fig. F7 - Relative log intensity versus frequency for received laser signal, 1 October 1969

Serious consideration is now being given to experimental measurements which will be sensitive to phase differences between different portions of an impinging wavefront and also to wavefront tilt from which information about beam wander may be obtained. We are presently planning experiments to measure beam motion directly and thereby obtain a measurement of the phase structure function. Simultaneous combined measurements of intensity and phase statistics will be most useful in categorizing the atmospheric medium (Ref. F4), and it seems that this is the approach which we should adopt at this time. A stable platform to be erected soon at CBD will permit intensity and phase measurements at 10.6 μm over a 2-mile path in a maritime environment. A high-speed thermometer will be used in addition to the meteorological sensors now being used on the overwater paths. We will be able to monitor these paths concurrent with laser propagation studies in the near future.

REFERENCES

F1. V.I. Tatarski, "Wave Propagation in a Turbulent Medium," McGraw-Hill, New York, 1961

F2. D.H. Höhn, Applied Optics 5(No. 9), 1427 (1966)

F3. G.R. Ochs, R.R. Bergman, and J.R. Snyder, J. Opt. Soc. Am. 59(No. 2), 231

F4. P.M. Livingston, private communication

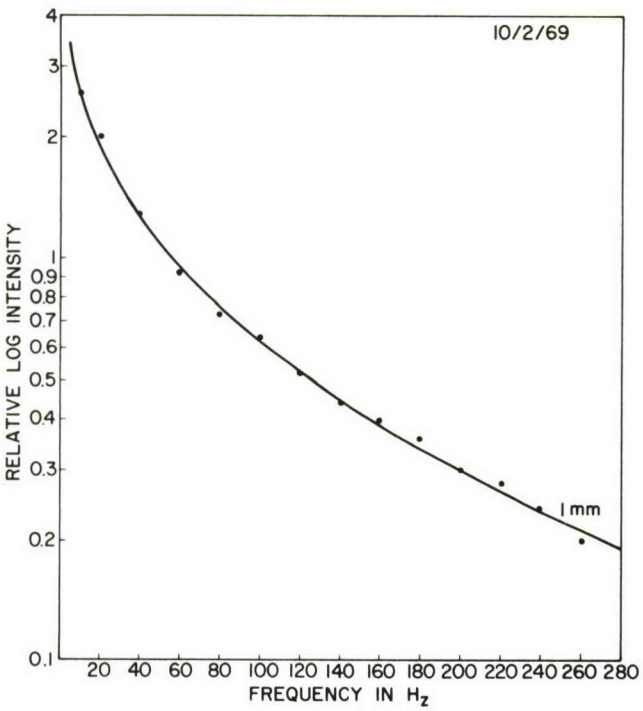

Fig. F8 - Relative log intensity versus frequency for received laser signal, 2 October 1969

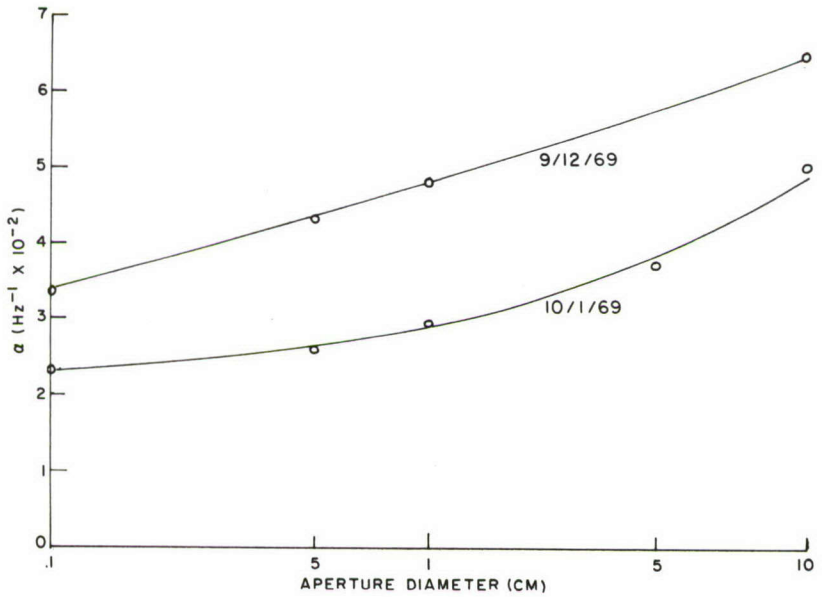

Fig. F9 - Empirical logarithmic decrement versus aperture diameter obtained from frequency spectra

Appendix G
(Confidential)

BEAM PROPAGATION IN AIR DOPED WITH SF_6

Louis Sica and E. A. McLean
Plasma Physics Division

(C) In this appendix we will present a laboratory study of thermal defocusing in air using a CO_2 laser beam. Our philosophy in undertaking a small-scale experiment is to gain sufficient understanding of the phenomena to aid in predicting results of larger scale experiments and to indicate the areas where the efforts with the larger and more expensive experiments should be concentrated. There are several advantages to performing a laboratory experiment rather than a field experiment if one wants to gain an understanding of the field situation. For example, beam quality, absorption coefficient, path length, wind velocity, and the homogeneity of the medium can be controlled. The medium itself can be varied as well as the beam diameter so as to change the time constants for conduction and convection. Since one can limit the number of interactions in the phenomenon, a theoretical description of the effects of each independent variable taken separately becomes feasible. Approximate theories for limiting cases may be more easily tested and generated. These separate analyses may then enable one to understand the more complex situation for which a purely mathematical analysis might be very difficult.

(U) The observations which we are reporting here are of two different types designed to supplement each other. The first is the observation of the intensity profile of the defocusing beam as a function of time. The second is the observation versus time of the integrated index of refraction perpendicular to the defocusing beam. This exposes to view the processes of conduction and convection along the beam.

(U) Figure G1 shows the experimental arrangement used to observe the intensity profile of the defocusing beam. The CO_2 laser beam had a power of 3.2 watts and a power density at the center of 21 watts/cm^2. It passed through a cell 16 cm long which contained 1 atmosphere of air and enough SF_6 (less than 5 Torr) to provide an absorption coefficient of 0.087 cm^{-1}. This is not enough to alter the bulk properties of the medium from those

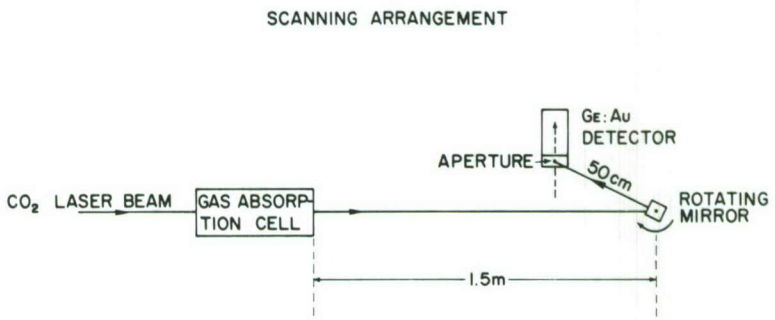

Fig. G1 - Apparatus for determining the beam profile

of air. The beam was then swept in a vertical plane past a gold-doped germanium detector by a four-sided rotating mirror moving at 1800 rpm.

(U) The rotating mirror and detector were also used to measure the Gaussian parameter of the laser beam as it entered the absorption cell. (The Gaussian parameter is defined here as the half width of the intensity profile at 1/e.) Figure G2 shows the measured laser intensity profile scaled to fit a Gaussian function. The good fit ensures that the laser was operating in the TEM_{00} mode. The Gaussian parameter β for the laser beam was found to be 0.22 cm.

(U) Figure G3 shows oscillograms of the defocusing beam profile at the indicated times measured from the moment of opening of an electromechanical shutter. A pulse from the shutter triggered the upper sweep of the oscilloscope, that is, the upper trace in each picture. Each spike on the upper trace corresponds to one sweep of the defocusing beam across the detector. After a variable time delay a brightened spike occurs which is magnified by the faster speed of the lower sweep. One can see from the upper-trace spikes on the first oscillogram that the defocusing reaches a maximum (or the peak intensities reach a minimum) at about 0.05 sec. After attaining its maximum diameter the beam contracts somewhat but not to its original width. This is shown by the increase in amplitude of the spikes of the upper trace in the last frame at 0.44 sec. It is also shown clearly by the increase in height and decrease in width of the pattern in the lower trace of that oscillogram compared to the beam profile shown in the immediately preceding oscillograms. This lessening of defocusing is caused by increasing convection which brings unheated air into the beam path, thus increasing the refractive index. It has been observed previously in thermal defocusing in liquids by Carman and Kelley (Ref. G1). The defocusing overshoot observed here is unaffected by possible beam motion into the convective wind due to the vertical plane of the scan across the detector face. This also accounts for the fact that one does not observe the two humps of the half-moon rim. We have observed this feature however in the defocused pattern as seen using a liquid-crystal image screen detector.

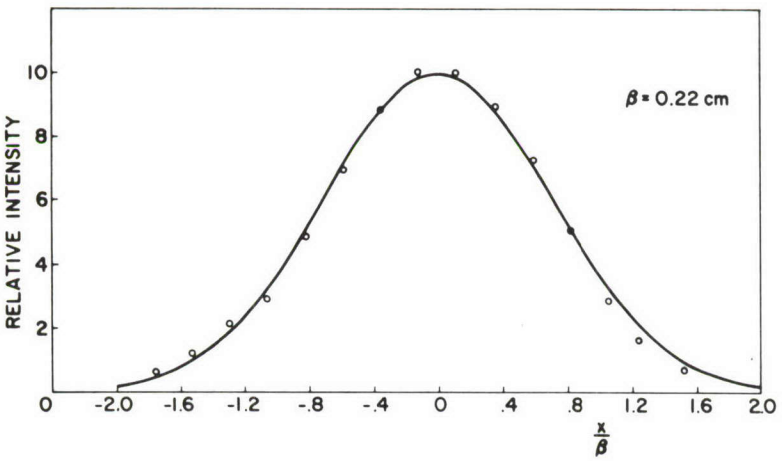

Fig. G2 - Laser intensity profile at 3.8 watts. The data points are experimental measurements and the curve is a theoretical Gaussian (e^{-x^2/β^2}).

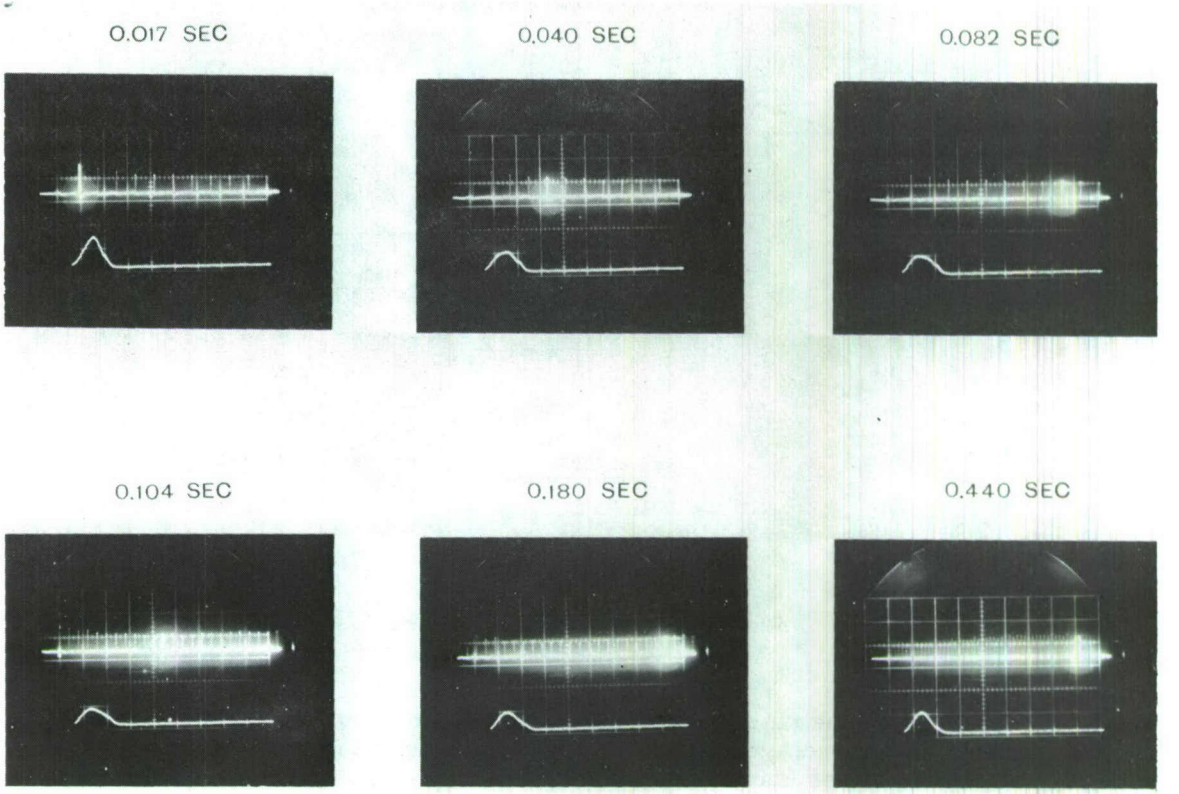

Fig. G3 - Defocusing laser beam intensity scans. Times shown indicate elapsed time since opening the shutter.

(U) We turn now to the observation of the index changes which cause the defocusing. The arrangement of the apparatus is shown in Fig. G4. The CO_2 laser beam is incident on a beam expander, which for the present experiment was operated one-to-one; i.e., both mirrors had equal focal lengths. They were adjusted so that there was slight focusing of the beam to reduce its diameter somewhat at the cell entrance window located 4 m from the laser. The dotted pattern after the beam expander indicates the position of a mirror used to deflect the beam to the rotating mirror and the detector for measurement of its profile. The distance from the mirror to the detector equaled that from the mirror to the cell. The timing reference laser sent a beam into the field of view of the movie camera when the shutter opened, thus marking the zero of time. The power meter was used to monitor the power continuously during each filming run. The 5-mW He-Ne laser in the upper-right-hand corner of Fig. G4 served as the light source for the interferometer.

(U) Before considering the movie data of the fringes formed during defocusing in air, it is useful for purposes of comparison to review briefly the evolution of the fringes accompanying defocusing in liquid carbon tetrachloride doped with iodine. This is shown in Fig. G5. The defocusing beam itself is shown at the right of the fringes at corresponding times. Notice that at 0.5 and 0.9 sec the fringes and the defocusing beam are essentially symmetrical. At 2.5 sec the beam spot has almost reached its steady state asymmetry, but the fringe asymmetry is perceptible only in the very first fringe at the left. In the bottom frame a cylinder of fluid is rising in the cell, but the defocusing spot has not changed appreciably.

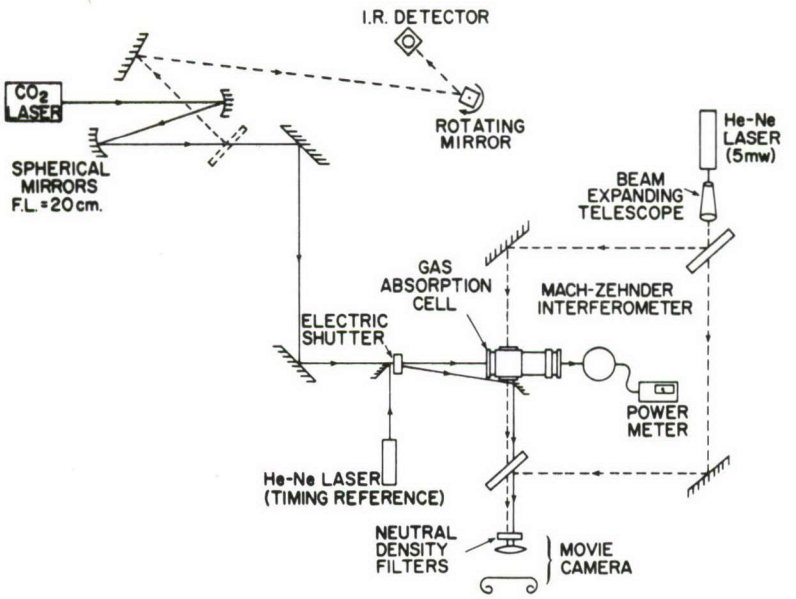

Fig. G4 - Experimental arrangement for interferometer fringes

(U) A movie for the air case was taken at 500 frames per second, but, except for the faster rate of development, evolution of the fringes was observed to be similar to that described above. Three frames from this movie, representing states corresponding to the last three frames shown in Fig. G5 for liquid CCl_4, are shown in Fig. G6. The defocusing beam is incident from the left in the region of the notch. The early time symmetry of the fringes gives way to gradually increasing asymmetry as the fringes move upward in the field under the action of the bouyant force. A cylinder of fluid then rises in the field, and there is a decrease in the amplitude of fringe deflection in the neighborhood of the notch.

(U) We have exploited the similarity between the liquid and gas cases by fitting fringe shapes occurring at early times to contours computed from the thermal diffusion equation alone, under the assumption of a Gaussian heating source (Ref. G2). Figure G7 shows such a fit for a fringe approximately 1 cm from the entrance window at 0.042 sec. The dotted line in this figure indicates the shape of the Gaussian heat source used to compute the shape of the outer curve. The reasonable fit of the data is consistent with the general indication that convection is a small influence at this time.

(U) Figure G8 is a composite of the shapes assumed by the fringe at a set of different times. These times are listed on the upper portion of each curve. It is pertinent to consider the shape of the fringe at significant times in the evolution of the defocusing as indicated by our rotating mirror intensity data. The thermal conduction time constant $\beta^2/4K$ (where K is the heat diffusivity) equals 0.056 sec for our beam radius. The conduction time is the time it takes for a heat impulse to spread over the beam area, and in the convectionless case it corresponds to the time at which the beam has defocused to about 1/2 its maximum size. In the present case it corresponds to maximum defocusing, since perceptible upward fringe motion is beginning to occur at that time which limits the amplitude of the fringe deflection. Contraction of the defocusing beam has been completed by about 0.29 sec, so that this fringe corresponds to a steady state for the propagation process. The fringes in the region of the heating beam have essentially reached their

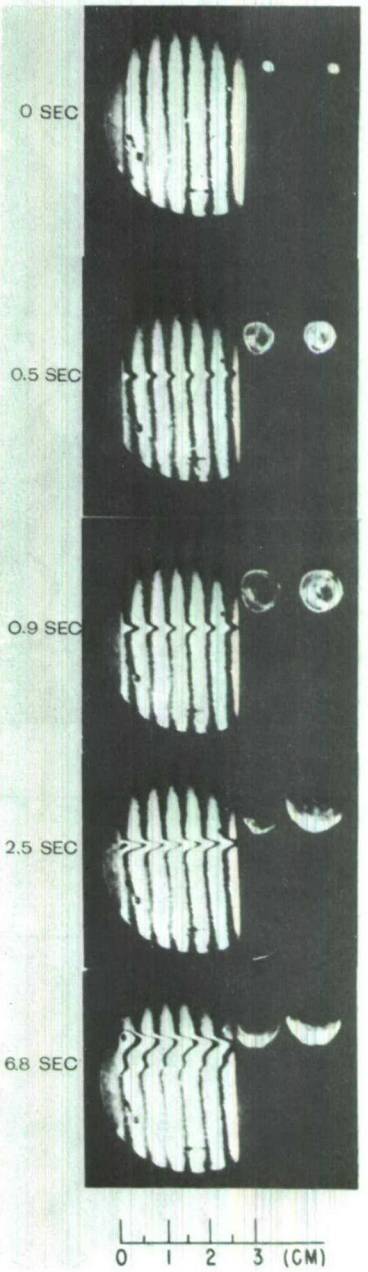

Fig. G5 - Interference fringe deflection due to the heating of CCl_4 by the absorption of He-Ne laser light (6328 Å). The heating beam passes through the cell horizontally from left to right. The time indicated on the left of each photograph is the elapsed time after turning on the laser beam. The two small patterns at the right show the thermally defocused laser beam as viewed 55 cm from the exit window of the liquid cell. (Two patterns are produced due to reflections from the two surfaces of the beam splitter.)

final shape. Consequently, the fluid motion need be accounted for theoretically only during a limited time and over the limited region of the heating beam.

(U) Another indication of the nature of the fluid motion is shown in Fig. G9. This is a plot of the vertical displacement of the fringe peak versus time. The plot indicates that although fluid motion begins at t = 0, the displacement has been less than 25 percent of the Gaussian parameter up to about 0.05 sec. As we have seen, the defocusing stops increasing after this time because of the increase in the fluid motion. The shape of the

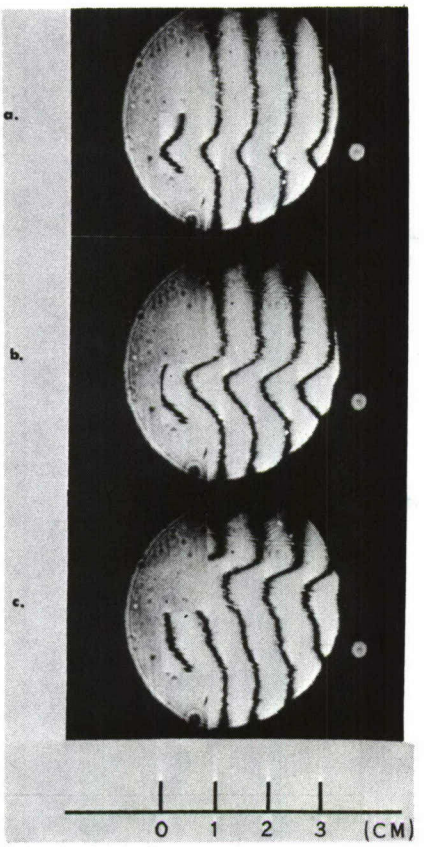

Fig. G6 - Selected frames taken from a movie showing the interference fringe deflection due to heating of air (doped with SF_6) by the absorption of CO_2 laser light (10.6 μm). The elapsed times after turning on the laser beam is (a) 0.041 sec, (b) 0.159 sec, and (c) 0.275 sec. The heating laser beam enters the absorption cell through a window at the base of the notch to the left and passes horizontally through the cell. (The dot in the lower-right-hand corner of the frames is from the timing reference laser.)

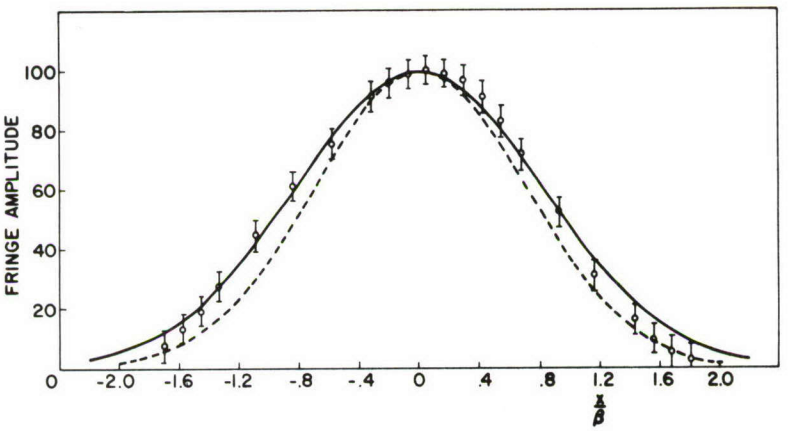

Fig. G7 - Fringe shape in air doped with SF_6. The time $\tau_c = \beta^2/4k = 0.0576$ sec and $t = 0.042$ sec. The plotted points are measured values with estimated error brackets. The solid line is a theoretical curve. The dashed line is the Gaussian source.

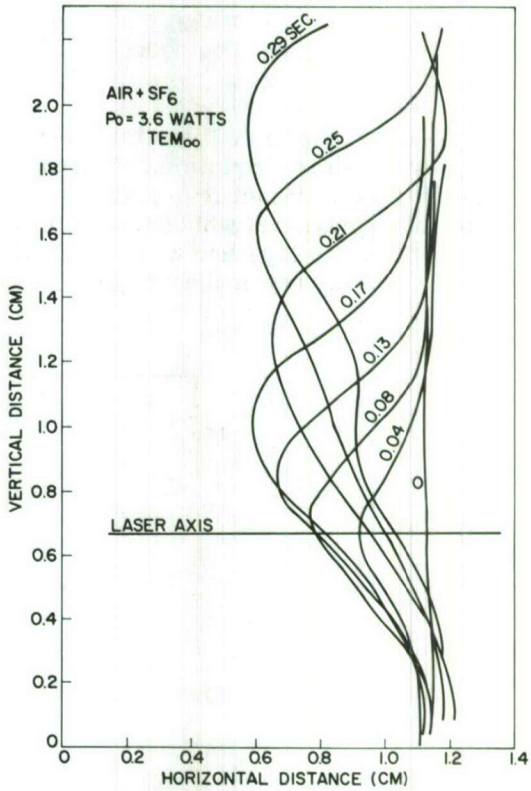

Fig. G8 - Composite fringe shapes at different times during thermal defocusing in air doped with SF_6

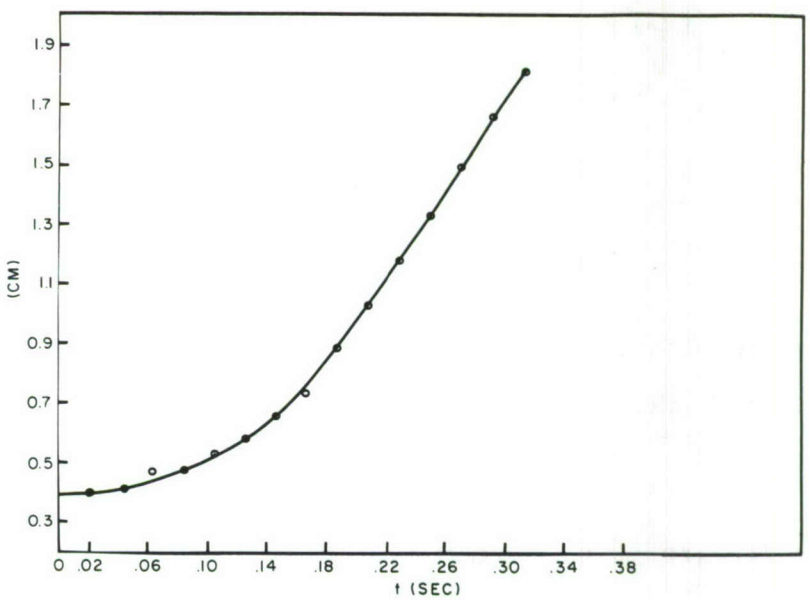

Fig. G9 - Vertical displacement of the fringe peak as a function of time

graph appears to be roughly parabolic, and the log-log plot of Fig. G10 shows that this is indeed the case. The equation of the curve of best fit is shown in the upper-left-hand corner.

We have computed the fluid position versus time given by an approximate solution to the Navier-Stokes equation. It initially has a cubic dependence on time and contains a scaling time constant β^2/ν = 0.3 sec. Here β is the Gaussian parameter and ν is the kinematic viscosity, which equals 0.15 cm^2/sec in the case of air. We are currently using this expression together with the conduction equation to see if it is possible to account for the asymmetry of the fringes at early times.

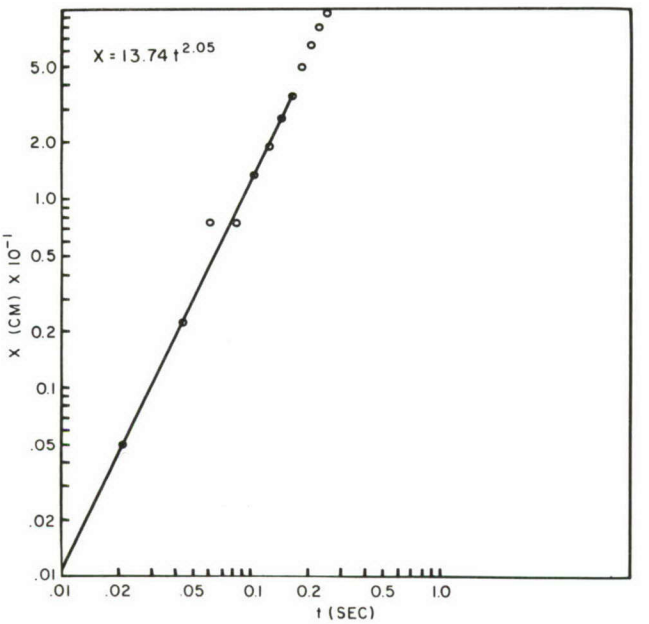

Fig. 10 - Same as Fig. 8 except plotted on log-log scale

REFERENCES

G1. R.L. Carman and P.L. Kelley, Appl. Phys. Letters 12, 241 (1968)

G2. E.A. McLean, L. Sica, and A.J. Glass, Appl. Phys. Letters 13, 369 (1968)

Appendix H
(Secret)

TARGET AND MATERIALS DAMAGE ANALYSIS

Bruce J. Faraday, Carmine A. Carosella, and Francis J. Campbell
Solid State Division

METHOD OF ANALYSIS

This appendix will fall into four principal subdivisions. First, a comprehensive list of enemy threats to the Navy as compiled from intelligence sources (Refs. H1-H5) will be presented. Special emphasis will be placed on missiles, since these are presumed to be the primary current and future threat. From this tabulation, one missile, the SS-N-2 (Styx), will be selected and analyzed from the point of view of its components, materials, and structure. Next, one material, an aluminum alloy, will be surveyed for an examination of those parameters that could be relevant from the point of view of Eighth Card damage studies. Finally, an actual experiment will be described to illustrate the experimental approach to determine quantitatively a parameter which could be important to materials damage, namely, the absorption of 10.6-μm radiation in aluminum alloy. The general plan of approach, then, is to follow a systems analysis beginning with an operational threat, e.g., a missile, to actual materials damage experiments which can be performed at the radiation facility to be set up at NRL in building A69 by Code 6460, and in due time, lead to target damage experiments to be carried out at the GDL installation at CBD.

THE THREAT TO THE NAVY

The current threat picture is indeed imposing, as shown in Fig. H1. The threat is subdivided according to type in the first column. Some types of threat, e.g., aircraft, may fulfill a multiplicity of functions. An aircraft may serve as a platform for a standoff air-to-surface missile and as such would be too far distant for an Eighth Card attack.

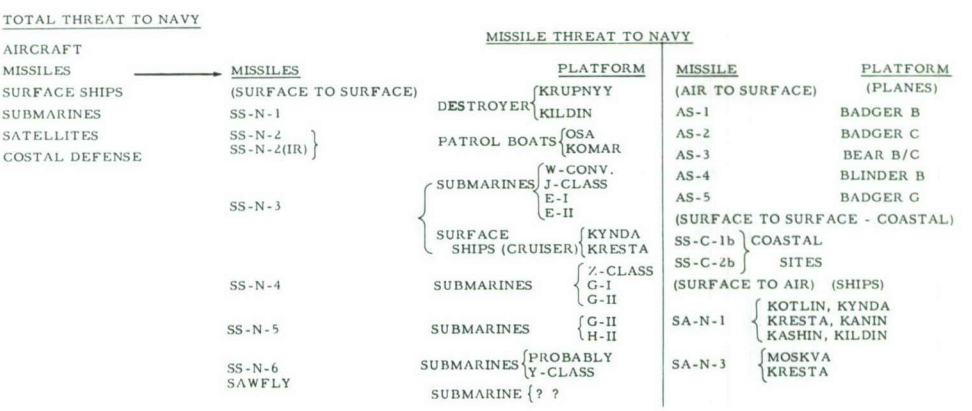

Fig. H1 - The total threat to the Navy and an analysis of the missile threat with appropriate launch platforms

Variants of the same aircraft may serve a reconnaissance function and thereby become a legitimate Eight Card objective.

In the second and fourth columns of Fig. H1 are seen a catalogue of various missiles, together with their respective platforms in the third and fifth columns. The tabulation shows the scope of the enemy missile arsenal – from subsonic missiles, such as the SS-N-1 or SS-N-2 to high-speed missiles (mach 3 or 4) with 1-ton nuclear warheads, such as the AS-4 (Kitchen) missile. It also points out the wide range of launch platforms (patrol boats, destroyers, aircraft, submarines, etc.) for the various missiles. The SS-N-3 is a particularly versatile weapon, having the capability of being launched by a variety of platforms (submarines or destroyers) and in a slightly modified version called the SSC-1-b (Shaddock) can be launched from mobile coastal defense sites.

The growing importance of missiles in the enemy's offensive plans may be inferred from the fact that on 1 October 1967 the U.S.S.R. was credited with having 187 surface ships, 370 submarines, and 3000 minor ships and craft. Among this number were 32 guided-missile cruisers and destroyers, 55 cruise-missile submarines, and 144 guided-missile patrol boats.

THE SS-N-2 MISSILE

The missile chosen for a more detailed treatment is the SS-N-2 (Styx). This weapon was chosen because it constitutes an important current threat to the Navy and because of the relatively complete state of knowledge according to intelligence sources (Refs. 4 and 5). This is not to imply that it will be the chief target of the Eighth Card program. By the anticipated time of the initial operational capability of the Eighth Card program, other missiles listed in Fig. H1 or future variants of these may be of primary interest. However, the relatively comprehensive level of information available on the SS-N-2 provides a guide for the analysis of other threat systems and for the location and identification of knowledge deficiencies in these.

The SS-N-2 missile is described to be a part of "a surface-guided missile system for use against naval ships whose relative size, importance, or disposition requires accurate delivery of an 1100-lb high-explosive warhead." There is no U.S. counterpart to the SS-N-2, although it represents essentially a physical combination of the Regulus I and the Lacrosse missile systems.

An analysis of the SS-N-2 missile according to function, configuration, and components is shown in Fig. H2. An evaluation of the location and function of components from the point of view of vulnerability of the SS-N-2 to Eighth Card attack can be summarized in the following list:

1. Thin aluminum alloy skin sections (as low as 0.047 in.).
2. Fiberglass nose section (thickness 6.3 mm); possible IR window (3 to 5 μm).
3. Electrical and fuel lines relatively exposed on the ventral surface of the missile.
4. Fuel tank that is an integral part of the fuselage.
5. Use of flush rivets on the skin.

SS-N-2 (STYX)

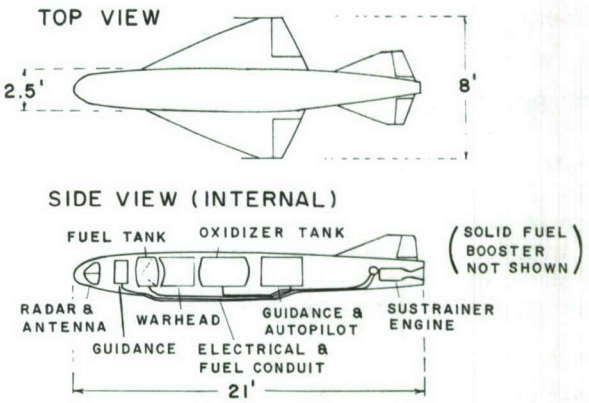

DESCRIPTION OF SS-N-2

GENERAL:

TYPE:	CRUISE
SPEED:	0.9 MACH (TERMINAL) SKIN TEMP = 100°C
RANGE:	4.5 TO 22 NM; TIME = 36 SEC -150 SEC
ENVIRONMENT:	LOW ALTITUDE - NAUTICAL (330-1000 FT)
LAUNCH PLATFORM:	OSA, KOMAR PATROL BOATS
WEIGHT:	TOTAL = 4600 LB; BURNOUT = 2600 LB

CONFIGURATION:

NOSE SECTION: BLUNT; 1.4' LONG × 2.0' WIDE; FIBERGLASS (6.3 MM)
(POSSIBLE I.R. WINDOW (3-5μ))

GUIDANCE: PREPROGRAMMED AUTOPILOT, X-BAND RADAR ACTIVE SEEKER
(POSSIBLE I.R. PASSIVE (3-5μ))

PROPULSION: SOLID FUEL BOOSTER (1.3 SEC) - (K ClO_4/C_2H_4O)

LIQUID FUEL ROCKET SUSTAINER (STAINLESS STEEL) – {AMINE FUEL / FUMING NITRIC ACID OXIDIZER}

WARHEAD: 1120 LB, SHAPED CHARGE WITH FORWARD STEEL CAVITY; IMPACT FUZES

{WINGS: / FUSELAGE:}
- MOSTLY REL. LOW STRENGTH AL-2024; SKIN THICKNESS .04"-.10"
- SEMI-MONOCOQUE CONSTRUCTION; DESIGN LOADS SAFETY FACTOR: {1.05 FOR YIELD / 1.3 FOR FAILURE}
- FLUSH RIVETRY; SWEPT WINGS (66°), WING WT. 68 LB (EACH) {LEADING EDGE .047" THICK / TOP .0985" / BOTTOM .0787"}
- WINGS BOLTED TO FUSELAGE AT 13 POINTS

Fig. H2 - The SS-N-2 (Styx) missile

6. Relatively long wing and fin roots.

7. Relatively low design factor (1.05 for yield).

MATERIAL PARAMETERS OF ALUMINUM ALLOY

The material selected for a detailed examination of parameters relevant to Eighth Card damage studies is aluminum alloy 2024. It is not being suggested at this time that the aluminum alloy skin is the most vulnerable material or component of the SS-N-2 so far as the Eighth Card program is concerned. However, the fact that it comprises by far the major fraction of the exterior area and that it is adjacent to components which are certainly vulnerable (fuel tank and lines, electrical wiring, etc.) makes it advisable to consider it.

It is pointed out that this particular alloy is a relatively-low-strength metal, which thereby lessens the likelihood of crack propagation. It is in common use in the Soviet Aircraft industry and thus may have application as a structural material on aircraft, satellites, and other missiles.

A list of materials parameters which may be relevant from the point of view of the Eighth Card program is shown in Fig. H3. The first parameter, the absorption coefficient α in aluminum alloy 2024 at 10.6 μm is a measure of the extent to which the laser beam couples with the surface of the aluminum alloy. The accurate measurement of α of aluminum alloy at 10.6 μm under carefully controlled laboratory conditions is an experiment of more than routine difficulty in that about 98 percent of the incident energy is reflected at this wavelength. To be relevant to the Eighth Card program α should be determined as a function of (a) the temperature to simulate the ambient temperature of an aerodynamically heated missile surface, (b) the angle of incidence of the radiation to the surface, (c) the actual marine environment (moving salty moist air), and (d) surface roughness.

An intensive test program is indicated in each of the above categories. Such tests may point to the relative importance of the various conditions on the value of α; the tests may also reveal conditions which have been overlooked by the present analysis.

Once the laser beam impinges on the metallic surface, the rate of transfer of thermal energy from the surface to the interior regions of the metal is important. This can be evaluated by a measurement of the thermal diffusivity K of the aluminum alloy. A determination of the value of K as a function of temperature cannot be made by the use of handbook values of the thermal conductivity and the heat capacity. These values represent static values measured under ideal controlled laboratory conditions. In the present situation, a high intensity laser beam will couple with the electrons and the lattice of the metal and may modify the materials parameters. Changes in the bulk properties of the metal will occur precisely where the laser beam is being delivered to the metal. Thus, measurements of the thermal diffusivity should be made not only as a function of temperature but also as a function of the power density delivered by the laser beam and the actual area of the beam.

The third subsection of Fig. H3, Strength of Materials, incorporates some of the suggested mechanisms of damage of the aluminum alloy skin by a Eighth Card weapon. These reflect the point of view that the primary mechanism of damage should not necessarily be considered to be melting or vaporization. It is suggested that a modest decrease in strength, ductility, stiffness, etc. can lead to structural failures which may cuase a missile to abort its primary mission.

AL-2024

AREAS OF STUDY

① ABSORPTION (REFLECTION) COEFF. AT 10.6μ

T

θ inc

ENVIRONMENT (VACUUM, MOVING AIR, WATER VAPOR, ETC.)

SURFACE PREPARATION (ROUGHNESS, PAINTS, ETC.)

ACTUAL CONFIGURATIONS (RIVETS, JOINTS, WING ROOTS, ETC.)

} MICROANALYSIS (CHEMICAL, METALLURGICAL)

② THERMAL DIFFUSIVITY $KC \frac{k}{\rho_c} \left(\frac{cm^2}{sec}\right)$

T

POWER DENSITY

AREA OF BEAM

ACTUAL CONFIGURATIONS

③ STRENGTH OF MATERIALS

STRESS-STRAIN VS. TEMPERATURE

CRYSTALLINE PHASE CHANGES

RESISTANCE TO CRACK PROPAGATION

CRACK FORMATION IN THERMALLY SOFTENED REGIONS

ACTUAL CONFIGURATIONS

Fig. H3 - Experimental material parameters of aluminum alloy 2024 relevant to Eighth Card damage studies

As pointed out earlier the SS-N-2 (in common with most aerodynamic systems) is not overdesigned for its mission – having the safety factor of 1.05 for yield and 1.30 for failure. It is not unreasonable to expect that a localized high-energy laser beam by its heating action may bring about phase changes in the crystal structure (below the melting point) which will change the material properties of the metal. For example, a localized area of the skin may become more brittle during the course of a solid-state phase change. This would greatly increase the probability of incipient embryo cracks in this region to propagate, because the resulting stress intensity may exceed the design stress level. For higher temperatures, the possibility of the formation of cracks in a thermally softened region should be examined.

In the determination of all three types of parameters above, actual configurations (riveted sections, butt joints, welds, wing roots, etc.) should be studied in parallel with standard laboratory samples.

EXPERIMENT DESIGN

A relevant experiment will now be given for illustrative purposes. It is designed to measure the absorption coefficient of aluminum alloy 2024 at 10.6 μm. In particular it is suggested as a way to study α as a function of ambient metal temperature as well as surface preparation (high polish, roughness, paints, welds, etc). The experiment is designed as a survey or test type which can serve as a prototype for more detailed experiments to relate changes in α caused by different surface preparations.

The classical heat flow equation, with a source term, is given by

$$\frac{\partial T}{\partial t} = K\nabla^2 T + \frac{Q_o \alpha}{\rho C} .$$

Here Q_o is the optical power per cm^2 incident on the sample, α is the absorption coefficient in cm^{-1}, T is the temperature (°C), t is the time, ρ is the density, C is the specific heat, and K is the thermal diffusivity in cm^2/sec.

The equation as it stands neglects convection and radiation terms. If there is no heat flow from the sample and if the sample is sufficiently small (about 7 cm^2 in area and 1 mm thick) and uniformly heated by a laser beam, then the diffusion term $K\nabla^2 T$ may be neglected. Thus

$$T = \frac{Q_o \alpha}{\rho C} t.$$

The temperature of the sample is measured as a function of irradiation time, and the slope of the temperature rise of the aluminum alloy versus time allows the determination of the value of α. The quantity Q_o would be measured with a radiation thermopile; ρ and C would be taken from handbook values.

The experimental arrangement is shown in Fig. H4. The experiment would initially be conducted in vacuum to eliminate conduction and convection losses. A radiation shield made of the aluminum alloy heated to suitable temperatures would minimize sample radiation losses. The experimental procedure would consist of heating the sample with the laser beam to the temperature where radiation losses are minimized and recording the incremental temperature rise versus time (using a thermocouple and a suitable recorder).

Calculations show that for the worse case expected (98-percent reflection and normal incidence) the temperature rise for a 300-watt CO_2 laser beam on the Al alloy sample would be 2.5°C/sec. For a 100-percent absorbing surface the temperature rise would be 125°C/sec. Within the range of these values, the experimental measurement of temperature should be routine.

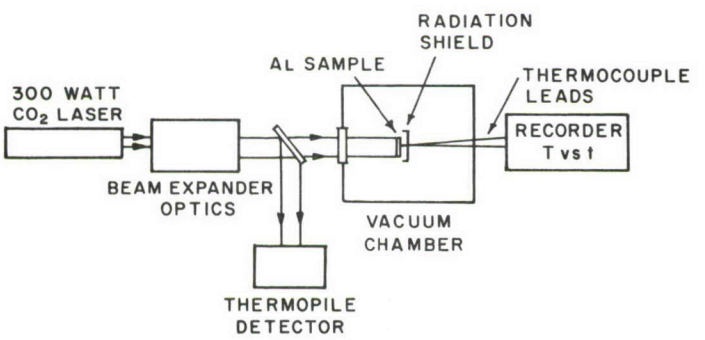

Fig. H4 - Experimental arrangement for measurements of absorption coefficients of aluminum alloy 2025 at 10.6 μm

ACKNOWLEDGMENTS

The authors wish to acknowledge the technical assistance of personnel at the Naval Weapons Laboratory, Naval Reconnaissance and Technical Support Center, Naval Scientific and Technical Intelligence Center, and at the Naval Research Laboratory.

REFERENCES

H1. Letter from Naval Scientific and Technical Intelligence Center, "Update of Naval Threat List (U)," STIC Ser. 16.002493, 2 Oct. 1969 (Secret Noforn)

H2. "Antiship Missile Defense," CNO Publication NWP-31 (Secret Noforn)

H3. "Missile-Threat Ship Defense Study," Appendix A, "Description of Threats and Their Vulnerabilities (U)," MSDS Group, Alan Berman, Chairman, 27 Nov. 1968 (Secret Noforn)

H4. S.R. Garrison, "Vulnerability of the Soviet SS-N-2 (STYX) Missile to Selected Kill Mechanisms (C)," NWL Report to be published (Secret Noforn)

H5. "Ship-Launched Cruise Missile System (SS-N-2)-U.S.S.R. (U)," STIC-CS-10-2-65 with Change 1 incorporated, 1 Oct. 1967 (Secret Noforn)

Appendix I

CONFIDENTIAL

NRL Report 6985

A Theoretical Study of Heat Conduction Associated with Laser-Irradiated Solids

[Unclassified Title]

J. E. ROGERSON, W. R. FAUST, AND A. D. ANDERSON

Applied Physics Branch
Applications Research Division

December 31, 1969

NAVAL RESEARCH LABORATORY
Washington, D.C.

CONFIDENTIAL

CONTENTS

Abstract	ii
Problem Status	ii
Authorization	ii
INTRODUCTION	1
STATEMENT OF THE PROBLEM	1
ONE-DIMENSIONAL CASE	2
THREE-DIMENSIONAL CASE	7
CONCLUSIONS	24
REFERENCES	25

ABSTRACT
[Unclassified]

Interest in the problem of the heating which occurs in materials irradiated by intense laser beams has been stimulated by the continued development of lasers with high power output. The present classical analysis, unlike most of the literature published to date, includes the blackbody reradiation by the material and its effect on the final equilibrium temperature, as well as the changes in temperature with time. Only the simple heating problem is considered; effects such as melting or plasma blowoff are ignored.

PROBLEM STATUS

This is an interim report; work on this problem is continuing.

AUTHORIZATION

NRL Problem R05-31
Project ORD 0832-129/173-1/U 1754 P.A. No. 1

Manuscript submitted September 16, 1969.

A THEORETICAL STUDY OF HEAT CONDUCTION ASSOCIATED WITH LASER-IRRADIATED SOLIDS
[Unclassified Title]

INTRODUCTION

(U) The continuing development of lasers with high power output has stimulated interest in the problem of material heating due to irradiation with high-energy laser beams. In addition to heating, high-power beams may vaporize some of the material through the "blowoff" phenomenon and subsequent shock waves. Studies of these high-power-density effects have been reported in the literature (1-4). However, all the reported work either ignores the material's blackbody reradiation and its effect upon the final temperature, as well as the rate of change of the temperature, or the problem is presented without a solution. In this report, only the heat conduction problem with a fourth-power radiation law at the boundary is considered. This corresponds to the case where the energy flux is not sufficient to produce a plasma or shock waves, or to the case where the target is moving and the beam is not focused on the material long enough to produce these more spectacular effects. This report presents a purely classical treatment of the problem.

STATEMENT OF THE PROBLEM

(U) The problem under consideration is depicted in Fig. 1. A laser beam with a spatial power distribution given by $P(\mathbf{r})$ is incident from the left on the plane boundary of a semi-infinite solid. A cylindrical coordinate system is chosen with its origin at the center of the beam and lying in the plane boundary of the solid. The z-axis is chosen normal to the boundary of the solid, and the r and θ corrdinates lie in the plane of the boundary.

(U) The heat conduction equation is

$$\nabla^2 T(\mathbf{r}, t) = \frac{1}{\kappa} \frac{\partial}{\partial t} T(\mathbf{r}, t) \tag{1}$$

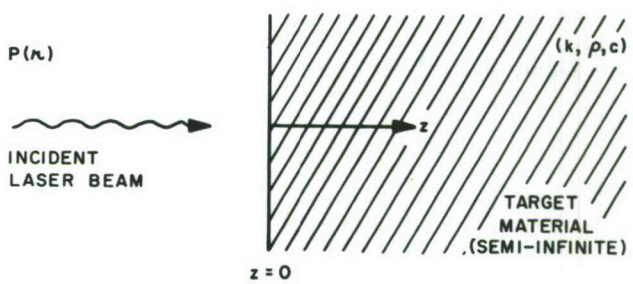

Fig. 1 - A laser beam with spatial power distribution $P(\mathbf{r})$ is incident on a semi-infinite solid characterized by its thermal conductivity k, density ρ, and specific heat c

where

$$\kappa = k/\rho c \tag{2}$$

and $T(\mathbf{r}, t)$ is the temperature in the solid, k is the thermal conductivity of the solid, ρ is the density of the solid, and c is the specific heat of the solid. This form of the equation implies the assumption that κ, and hence ρ, k, and c, are constants.

(U) The boundary condition at $z = 0$ is taken to be

$$-k \frac{\partial T}{\partial z} = \alpha P(\mathbf{r}) - \sigma E (T^4 - T_i^4) \tag{3}$$

where E is the emissivity of the surface, α is the absorption coefficient for the appropriate frequency, and σ is the Stefan-Boltzmann constant. The term $\sigma E T^4$ represents the blackbody reradiation at the surface, and T_i is the initial temperature at the surface. It is assumed that the target and its environment are initially at the same temperature (thermal equilibrium).

(U) In an idealized situation where no melting or other changes of state occur, the temperature in the material becomes uniform as time becomes increasingly large. In this case $\partial T/\partial z$ vanishes in Eq. (3), and a final equilibrium situation is achieved:

$$\alpha P(\mathbf{r}) = \sigma E (T^4 - T_i^4) \ . \tag{4}$$

This concept makes it possible to define a final equilibrium temperature T_f as

$$T_f^4 = \frac{\alpha P_0}{\sigma} + T_i^4 \tag{5}$$

where E has been taken as unity in order to estimate a lower limit for T_f. T_f represents the maximum temperature that can be obtained in the solid; $P(0) \equiv P_0$ is the power density at the center of the beam which is assumed to be a maximum at this point.

ONE-DIMENSIONAL CASE

(U) As a first approach to the problem, a solution to Eq. (1) will be attempted for the one-dimensional case. For this situation, $P(\mathbf{r}) \equiv P_0 = \text{constant}$, and $T_i \equiv T_a$ (the ambient temperature). Equation (1) becomes

$$\frac{\partial^2 T}{\partial z^2} = \frac{1}{\kappa} \frac{\partial T}{\partial t} \ , \tag{6}$$

and the boundary condition (Eq. (3)) at $z = 0$ is

$$-k \frac{\partial T}{\partial z} = \alpha P_0 - \sigma (T^4 - T_a^4) \tag{7}$$

where the emissivity E has been taken as unity.

(U) The Laplace transform of Eq. (6) is now taken; this gives

$$\frac{\partial^2 \tilde{T}}{\partial z^2} = \frac{s}{\kappa}\,\tilde{T} - \frac{T_a}{\kappa} \tag{8}$$

where

$$\tilde{T}(z,s) = \int_0^\infty e^{-st} T(z,t)\, dt \ ,$$

and $T(z,o) = T_a$, with s being a complex variable. Equation (8) has the solution

$$\tilde{T}(z,s) = A(s)\, e^{-z\sqrt{\frac{s}{\kappa}}} + T_a/s \ , \tag{9}$$

where $A(s)$ will be chosen to satisfy the boundary condition, which gives,

$$T(z,t) = T_a + \frac{1}{2\pi i} \oint A(s)\, e^{-z\sqrt{\frac{s}{\kappa}}}\, e^{st}\, ds \tag{10}$$

where $\oint$ indicates the Bromwich integral. Thus Eq. (10) is the inverse Laplace transform of Eq. (9).*

(U) Substituting $T(z,t)$ from Eq. (10) into Eq. (7) gives

$$\frac{k}{2\pi i} \oint \sqrt{\frac{s}{\kappa}}\, A(s)\, e^{st}\, ds = \alpha P_0 - \sigma \left(T_a + \frac{1}{2\pi i} \oint A(s)\, e^{st}\, ds \right)^4 + \sigma T_a^4 \tag{11}$$

for the boundary condition at $z = 0$. This may be rewritten as

$$\begin{aligned} T_a + \frac{1}{2\pi i} \oint A(s)\, e^{st}\, ds &= \left(\frac{\alpha P_0}{\sigma} - \left(\frac{k}{\sigma} \frac{1}{2\pi i} \oint \sqrt{\frac{s}{\kappa}}\, A(s)\, e^{st}\, ds \right) + T_a^4 \right)^{1/4} \\ &= \left[(T_f^4 - T_a^4) - \left(\frac{k}{\sigma} \frac{1}{2\pi i} \oint \sqrt{\frac{s}{\kappa}}\, A(s)\, e^{st}\, ds \right) + T_a^4 \right]^{1/4} \\ &= T_f \left(1 - \frac{k}{\sigma T_f^4} \frac{1}{2\pi i} \oint \sqrt{\frac{s}{\kappa}}\, A(s)\, e^{st}\, ds \right)^{1/4} \end{aligned} \tag{12}$$

*The Laplace transform theorem must be applied to the transforms for the semiclosed region $z \geq 0$. If it were applied to the transform of $e^{-z\sqrt{s/\kappa}}$, for example, which is valid only for the open region $z > 0$, the limiting case of the boundary $z = 0$ would not be available. Hence the theorem must be applied to functions $f(s)$ of the type that are valid for $z \geq 0$.

with the aid of Eq. (5). If it is assumed that the second term in the bracket is much less than unity because of the T_f^{-4} factor, this expression may be expanded approximately as

$$T_a + \frac{1}{2\pi i}\oint A(s)\, e^{st}\, ds \approx T_f - \frac{k}{4\sigma T_f^3}\,\frac{1}{2\pi i}\oint \sqrt{\frac{s}{\kappa}}\, A(s)\, e^{st}\, ds + \ldots . \tag{13}$$

Therefore,

$$\frac{1}{2\pi i}\oint e^{st}\, ds \left[\left(1 + \frac{k}{4\sigma T_f^3}\sqrt{\frac{s}{\kappa}}\right)A(s) - \frac{(T_f - T_a)}{s} \cdots\right] \approx 0 . \tag{14}$$

By equating the integrand to zero, the following expression for $A(s)$ is obtained:

$$A(s) = \frac{T_f - T_a}{s\left(1 + \dfrac{k}{4\sigma T_f^3}\sqrt{\dfrac{s}{\kappa}}\right)} = \frac{\gamma(T_f - T_a)}{s(\sqrt{s} + \gamma)} \tag{15}$$

where

$$\gamma = \frac{4\sigma\sqrt{\kappa}\, T_f^3}{k} . \tag{16}$$

Using this result in Eq. (10) gives

$$T(z,t) = T_a + (T_f - T_a)\,\frac{\gamma}{2\pi i}\oint \frac{e^{-z\sqrt{\frac{s}{\kappa}}}}{s\left[\sqrt{s} + \gamma\right]}\, e^{st}\, ds . \tag{17}$$

Now since

$$\frac{1}{s(\sqrt{s} + \gamma)} = \frac{1}{\gamma s} - \frac{1}{\gamma\sqrt{s}(\sqrt{s} + \gamma)} , \tag{18}$$

The integral in Eq. (17) can be written

$$\frac{\gamma}{2\pi i}\oint \frac{e^{-z\sqrt{\frac{s}{\kappa}}}}{s(\sqrt{s} + \gamma)}\, e^{st}\, ds = \frac{1}{2\pi i}\oint \frac{e^{-z\sqrt{\frac{s}{\kappa}}}}{s} e^{st}\, ds - \frac{1}{2\pi i}\oint \frac{e^{-z\sqrt{\frac{s}{\kappa}}}}{\sqrt{s}(\sqrt{s} + \gamma)}\, e^{st}\, ds . \tag{19}$$

(U) From standard tables of Laplace transforms (for example, Spiegel (5)), the two terms on the right in Eq. (19) can be written in terms of error functions. Then Eq. (17) becomes

$$T(z,t) = (T_f - T_a)\left[\operatorname{erfc}\left(\frac{z}{2\sqrt{\kappa t}}\right) - e^{\frac{\gamma z}{\sqrt{\kappa}} + \gamma^2 t}\operatorname{erfc}\left(\gamma\sqrt{t} + \frac{z}{2\sqrt{\kappa t}}\right)\right] + T_a . \tag{20}$$

At the boundary ($z = 0$) Eq. (20) becomes

$$T(0,t) = (T_f - T_a)\left[1 - e^{\gamma^2 t}\ \mathrm{erfc}(\gamma\sqrt{t})\right] + T_a\ , \tag{21a}$$

or using Eqs. (4) and (5)

$$T(0,t) = \left[\left(\frac{\alpha P_0}{\sigma E} + T_a^4\right)^{1/4} - T_a\right]\left[1 - e^{\gamma^2 t}\ \mathrm{erfc}(\gamma\sqrt{t})\right] + T_a\ . \tag{21b}$$

Now $\mathrm{erfc}(x) = 1$ for $x = 0$, and $\mathrm{erfc}(x) \to 0$ as $x \to \infty$. Therefore, at the boundary, for $t = 0$ Eq. (21a) becomes

$$T(0,0) = (T_f - T_a)(1 - 1) + T_a = T_a\ ,$$

and in the limit as $t \to \infty$

$$\lim_{t\to\infty} T(0,t) \to (T_f - T_a)(1) - T_a = T_f\ .$$

As the time t gets very large, the temperature T of the material goes asymptotically to T_f at the boundary ($z = 0$), as is expected from physical arguments. The same arguments applied to any finite value of z give the same results.

(U) The solution to the one-dimensional problem is presented because it is obtained without too much difficulty, and because it is of some physical interest. It also serves as a guide in treating the three-dimensional case. This solution does not take into account any changes of state in the material or any temperature-dependent variation of the thermal parameters of the material. If melting or vaporization occurs, the validity of the solution is questionable. However, Eq. (21b) may be of some value as an initial estimate of the time required for a given incident power density to initiate melting in a given material.

(C) Figure 2 presents some calculations based on this solution using zinc as the target material. The values of the parameters for zinc are taken from the *Handbook of Chemistry and Physics* and are given in Table 1. The incident power density P_0 is taken as 30 kW/cm^2. Table 2 presents a similar computation for a power density of 1 MW/cm^2, again using zinc as the target material.

Table 1 (U)
Values* of the Thermal Parameters of Zinc

Parameter	Value
Thermal Conductivity	$k = 1.13\times10^7$ erg cm^{-1} deg^{-1} sec^{-1}
$k/\rho c\ (=\kappa)$	$\kappa \simeq 0.5$ cm^2 sec^{-1}
Absorption Coefficient	$\alpha \simeq 0.15$
Stefan-Boltzmann Constant	$\sigma = 5.67\times10^{-5}$ erg cm^{-2} sec^{-1} deg^{-4}

*Taken from *The Handbook of Chemistry and Physics*, Chemical Rubber Publishing Co., Cleveland, Ohio, 34th Ed.

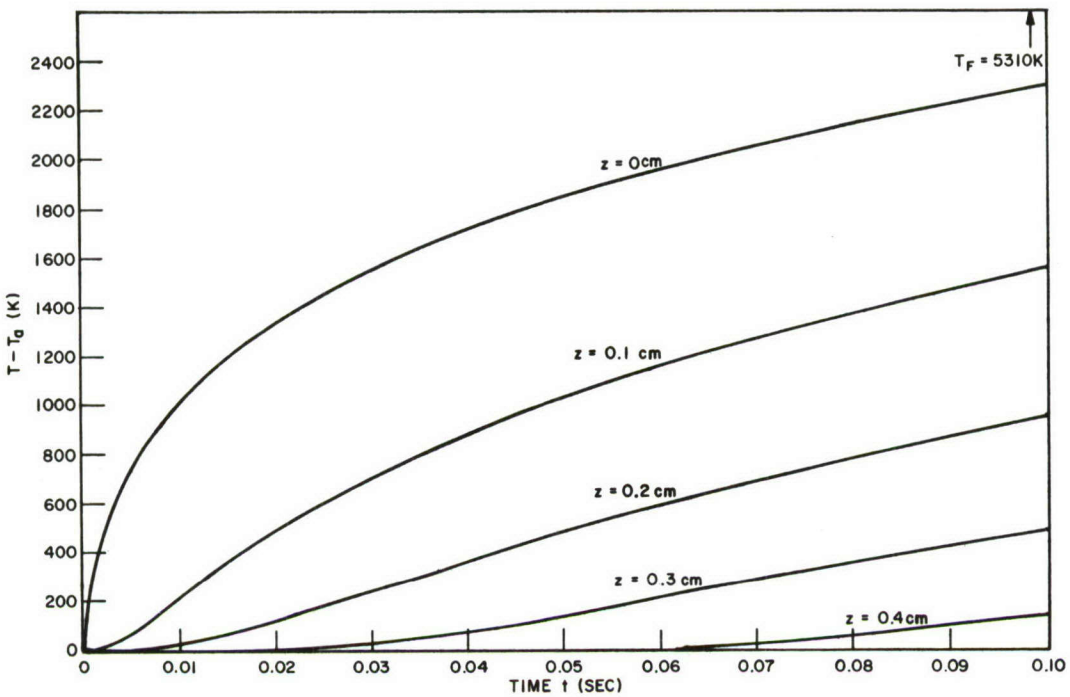

Fig. 2 - Theoretical temperature distribution for a zinc target irradiated by a laser beam. Each curve shows the variation of temperature with time for that particular location (or value of z) within the target; z is measured in the direction of the laser beam (normal to the target surface). The incident beam's power density P_0 is 30 kW/cm^2, and a is 0 in the power distribution relation $P = P_0\ e^{-4ar^2} = P_0$ = constant. T_f is the final equilibrium temperature of the target, toward which all the curves are asymptotic; T_a is the initial ambient temperature of the target. The case considered here is one dimensional, i.e., $T = T(z, t)$.

Table 2 (C)
Time Variation of Temperature at the Surface of Zinc for the One-Dimensional Case for an Incident Power Density P_0 of 1 MW/cm^{-2} and a Final Equilibrium Temperature T_f of 1.245×10^4 K

Surface Temperature (10^4 K)	Time (sec)
0	0
0.0128	1×10^{-7}
0.0284	5×10^{-7}
0.0398	1×10^{-6}
0.0862	5×10^{-6}
0.1195	1×10^{-5}
0.2445	5×10^{-5}
0.3266	1×10^{-4}
0.5660	5×10^{-4}
0.6634	1×10^{-3}
0.9184	5×10^{-3}
1.0029	1×10^{-2}
1.1303	5×10^{-2}
1.1618	1×10^{-1}

THREE-DIMENSIONAL CASE

(U) The three-dimensional problem is treated in the same coordinate system as the one-dimensional case. It is assumed that the power distribution in the incident beam is a function of the radial coordinate r only, and that the target material is homogeneous and isotropic; then the problem has axial symmetry. Under these assumptions, the power distribution can be written as

$$P(r) = P_0 g(r) \tag{22}$$

and the heat conduction equation becomes

$$\frac{1}{r}\frac{\partial}{\partial r}\left(r\frac{\partial T}{\partial r}\right) + \frac{\partial^2 T}{\partial z^2} = \frac{1}{\kappa}\frac{\partial T}{\partial t} . \tag{23}$$

Taking the Laplace transform of Eq. (23) gives

$$\frac{1}{r}\frac{\partial}{\partial r}\left(r\frac{\partial \tilde{T}}{\partial r}\right) + \frac{\partial^2 T}{\partial z^2} - \frac{s}{\kappa}\tilde{T} = -\frac{T_i}{\kappa} . \tag{24}$$

Here it is assumed that the initial temperature distribution T_i is given by

$$T_i = T_a \, e^{-\epsilon r^2} \tag{25}$$

where T_a is the ambient temperature, and ϵ is a very small parameter. The factor $e^{-\epsilon r^2}$ is introduced to insure convergence in some of the resulting integrals, and the limit as ϵ becomes vanishingly small will be taken in the final results, so that the initial temperature is then effectively T_a.

(U) Using Eq. (25) for T_i, Eq. (24) becomes

$$\frac{1}{r}\frac{\partial}{\partial r}\left(r\frac{\partial \tilde{T}}{\partial r}\right) + \frac{\partial^2 \tilde{T}}{\partial z^2} - \frac{s}{\kappa}\tilde{T} = -\frac{T_a}{\kappa}\, e^{-\epsilon r^2} \, . \tag{26}$$

The homogeneous equation is first solved by separation of variables. Let

$$\tilde{T}(r,z) = R(r)\, Z(z) \, . \tag{27}$$

Then

$$\frac{1}{r}\frac{d}{dr}\left(r\frac{dR(r)}{dr}\right) Z(z) + R(r)\frac{d^2 Z(z)}{dz^2} = \frac{s}{\kappa} R(r)\, Z(z) \, ,$$

from which

$$\frac{1}{R(r)}\left[\frac{1}{r}\frac{d}{dr}\left(r\frac{dR(r)}{dr}\right)\right] = -\left[\frac{1}{Z(z)}\frac{d^2 Z(z)}{dz^2} - \frac{s}{\kappa}\right]. \tag{28}$$

Setting both sides of Eq. (28) equal to $-\lambda^2$ gives

$$\left.\begin{aligned} &\frac{1}{r}\frac{d}{dr}\left(r\frac{dR(r)}{dr}\right) + \lambda^2 R(r) = 0 \Longrightarrow R(r) = J_0(\lambda r) \\ &\text{and} \\ &\frac{d^2 Z(z)}{dz^2} - \left(\lambda^2 + \frac{s}{\kappa}\right) Z(z) = 0 \Longrightarrow Z(z) = e^{-z\sqrt{\lambda^2 + \frac{s}{\kappa}}} \end{aligned}\right\} \tag{29}$$

where λ is the separation constant. Since exponentially growing solutions of $\tilde{T}$ for $z > 0$ are rejected on physical grounds, only the exponentially decaying solution for $Z(z)$ was retained in Eq. (29). Therefore, a solution of the homogeneous equation is

$$\tilde{T}(r,z,s) = J_0(\lambda r)\, e^{-z\sqrt{\lambda^2 + \frac{s}{\kappa}}} \tag{30}$$

where $J_0(\lambda r)$ is the Bessel function of the first kind.

(U) For a solution to Eq. (26), assume

$$\tilde{T}(r,z,s) = J_0(\lambda r)\, e^{-z\sqrt{\lambda^2+\frac{s}{\kappa}}} + A(s)\,\frac{T_a}{s}\, e^{-\epsilon r^2} \tag{31}$$

where $A(s)$ is to be determined. Then the relation

$$\frac{1}{r}\frac{d}{dr}\left(r\frac{d\tilde{T}}{dr}\right) = -\lambda^2 J_0(\lambda r)\, e^{-z\sqrt{\lambda^2+\frac{s}{\kappa}}} - 4\epsilon(1-\epsilon r^2)\, A(s)\,\frac{T_a}{s}\, e^{-\epsilon r^2}$$

results from Eq. (31). Since terms of the order of ϵ^2 are assumed to be negligible, then substituting into Eq. (26) gives

$$-\lambda^2 J_0(\lambda r)\, e^{-z\sqrt{\lambda^2+\frac{s}{\kappa}}} - 4\epsilon A(s)\,\frac{T_a}{s}\, e^{-\epsilon r^2} + \left(\frac{s}{\kappa}+\lambda^2\right) J_0(\lambda r)\, e^{-z\sqrt{\lambda^2+\frac{s}{\kappa}}}$$

$$= \frac{s}{\kappa}\left(J_0(\lambda r)\, e^{-z\sqrt{\lambda^2+\frac{s}{\kappa}}} + A(s)\,\frac{T_a}{s}\, e^{-\epsilon r^2}\right) - \frac{T_a}{s}\, e^{-\epsilon r^2}\,.$$

Solving this equation for $A(s)$ gives

$$A(s) = \frac{s}{s+4\kappa\epsilon}\,. \tag{32}$$

Therefore,

$$\tilde{T}(r,z,s) = J_0(\lambda r)\, e^{-z\sqrt{\lambda^2+\frac{s}{\kappa}}} + \frac{T_a}{s+4\kappa\epsilon}\, e^{-\epsilon r^2}\,. \tag{33}$$

(U) The above solution contains the parameter λ. A more general solution can be defined by

$$\tilde{T}(r,z,s) = \int_0^\infty J_0(\lambda r)\, e^{-z\sqrt{\lambda^2+\frac{s}{\kappa}}} f(\lambda)\,\lambda d\lambda + \frac{T_a}{s+4\kappa\epsilon}\, e^{-\epsilon r^2} \tag{34}$$

which then gives

$$T(r,z,t) = \frac{1}{2\pi i}\oint e^{st}\, ds \int_0^\infty f(\lambda) J_0(\lambda r)\, e^{-z\sqrt{\lambda^2+\frac{s}{\kappa}}}\,\lambda d\lambda + \frac{1}{2\pi i}\oint \frac{T_a\, e^{-\epsilon r^2}}{s+4\kappa\epsilon}\, e^{st}\, ds\,. \tag{35}$$

The function $f(\lambda)$ is to be chosen so that the boundary condition is satisfied. Substituting this solution into the boundary condition (Eq. (3)) gives

$$\frac{k}{2\pi i}\oint e^{st}\,ds\int_0^\infty \sqrt{\frac{s}{\kappa}+\lambda^2}\;J_0(\lambda r)\,f(\lambda)\,\lambda\,d\lambda = \alpha P(r)$$

$$-\sigma\left(\frac{1}{2\pi i}\oint e^{st}\,ds\int_0^\infty J_0(\lambda r)\,f(\lambda)\,\lambda\,d\lambda+\frac{1}{2\pi i}\oint\frac{T_a\,e^{-\epsilon r^2}}{s+4\kappa\epsilon}\,e^{st}\,ds\right)^4+\sigma T_a^4\,e^{-4\epsilon r^2}. \tag{36}$$

(U) As a first-order approximation, the term $\partial T/\partial z$ is set equal to zero, and $f(\lambda)\to f_0(\lambda)$, the "first-guess" solution. Then

$$\frac{1}{2\pi i}\oint e^{st}\,ds\int_0^\infty J_0(\lambda r)\,f_0(\lambda)\,\lambda\,d\lambda+\frac{1}{2\pi i}\oint\frac{e^{st}T_a}{s+4\kappa\epsilon}\,e^{-\epsilon r^2}\,ds=\left(\frac{\alpha P(r)}{\sigma}+T_a^4\,e^{-4\epsilon r^2}\right)^{1/4}. \tag{37}$$

From the expressions $P(r)=P_0\,g(r)$ and $\alpha P_0/\sigma = T_f^4 - T_a^4$ (from the one-dimensional case), Eq. (37) can be written

$$\frac{1}{2\pi i}\oint e^{st}\,ds\int_0^\infty J_0(\lambda r)\,f_0(\lambda)\,\lambda\,d\lambda+\frac{1}{2\pi i}\oint\frac{e^{st}T_a}{s+4\kappa\epsilon}\,e^{-\epsilon r^2}\,ds$$

$$=\left[\left(T_f^4-T_a^4\right)g(r)+T_a^4\,e^{-4\epsilon r^2}\right]^{1/4}. \tag{38}$$

Since $T_a/T_f \le 10^{-1}$, normally, the right-hand side of Eq. (38) becomes

$$\left[\left(T_f^4-T_a^4\right)g(r)+T_a^4\,e^{-4\epsilon r^2}\right]^{1/4}=T_f\left[\left(1-\frac{T_a^4}{T_f^4}\right)g(r)+\frac{T_a^4}{T_f^4}\,e^{-4\epsilon r^2}\right]^{1/4}$$

$$\approx T_f\,g(r)^{1/4}. \tag{39}$$

Therefore,

$$\int_0^\infty J_0(\lambda r)\,f_0(\lambda)\,\lambda\,d\lambda\approx\frac{T_f}{s}\,g(r)^{1/4}-\frac{T_a}{s+4\kappa\epsilon}\,e^{-\epsilon r^2}. \tag{40}$$

(U) In order to obtain $f_0(\lambda)$, multiply both sides of Eq. (40) by $J_0(\mu r)\,r\,dr$ and integrate from $r=0$ to $r=\infty$; this eliminates the r dependence and makes a solution for f_0 possible:

$$\int_0^\infty f_0(\lambda)\,J_0(\lambda r)\,\lambda\,d\lambda\int_0^\infty J_0(\mu r)\,r\,dr\approx\frac{T_f}{s}\int_0^\infty g(r)^{1/4}\,J_0(\mu r)\,r\,dr$$

$$-\frac{T_a}{s+4\kappa\epsilon}\int_0^\infty e^{-\epsilon r^2}\,J_0(\mu r)\,r\,dr. \tag{41}$$

The left-hand side of Eq. (40) is just the Fourier-Bessel integral; its value is $f_0(\mu)$. (See, for example, Ditkin and Prudnikov (6).)

(U) So far, $g(r)$ has not been specified. To get a specific result, a Gaussian distribution of the laser power is assumed, i.e.,

$$g(r) = e^{-4ar^2} . \tag{42}$$

Then, from Gradshteyn and Ryzhik (7) (hereafter referred to as G.R.),

$$f_0(\lambda) = \frac{T_f}{2as} e^{-\lambda^2/4a} - \frac{T_a}{2\epsilon(s + 4\kappa\epsilon)} e^{-\lambda^2/4\epsilon} \tag{43}$$

where μ has been replaced by λ.

(U) Again, assuming that terms of the order of ϵ^2 can be neglected, Eq. (43) gives as a first-guess solution the expression (from Eq. (35))

$$T^{(1)}(r,z,t) = \frac{1}{2\pi i} \oint e^{st}\, ds \int_0^\infty \left(\frac{T_f}{2as} e^{-\lambda^2/4a} - \frac{T_a}{2\epsilon s} e^{-\lambda^2/4\epsilon} \right) J_0(\lambda r)\, e^{-z\sqrt{\lambda^2 + \frac{s}{\kappa}}}\, \lambda d\lambda$$

$$+ T_a\, e^{-\epsilon(r^2 + 4\kappa t)} \tag{44}$$

where the inverse Laplace transform of the last term has been taken. Since the terms in the brackets inside the integrals are very similar, the integrations can be performed in detail for one term, and the other can be written down by analogy. Taking the first term and interchanging the order of integrations gives

$$T_1^{(1)} = \frac{T_f}{2a} \int_0^\infty e^{-\lambda^2/4a}\, J_0(\lambda r)\, \lambda d\lambda \left(\frac{1}{2\pi i}\right) \oint \frac{e^{-z\sqrt{\frac{s}{\kappa} + \lambda^2}}}{s} e^{st}\, ds . \tag{45}$$

Now

$$\frac{e^{-z\sqrt{\frac{s}{\kappa} + \lambda^2}}}{s} = \frac{e^{-z\sqrt{\frac{s}{\kappa} + \lambda^2}}}{(s + \kappa\lambda^2)} \frac{(s + \kappa\lambda^2)}{s} = \frac{e^{-z\sqrt{\frac{s}{\kappa} + \lambda^2}}}{s + \kappa\lambda^2} + \frac{\kappa\lambda^2}{s} \frac{e^{-z\sqrt{\frac{s}{\kappa} + \lambda^2}}}{(s + \kappa\lambda^2)} . \tag{46}$$

By the "Shift Theorem"

$$\mathcal{L}^{-1}\left(\frac{e^{-\frac{z}{\sqrt{\kappa}}\sqrt{s + \kappa\lambda^2}}}{s + \kappa\lambda^2} \right) = e^{-\kappa\lambda^2 t}\, \mathcal{L}^{-1}\left(\frac{e^{-\frac{z}{\sqrt{\kappa}}\sqrt{s}}}{s} \right)$$

$$= e^{-\kappa\lambda^2 t}\, \operatorname{erfc}\left(\frac{z}{2\sqrt{\kappa t}} \right) \tag{47}$$

where $\mathcal{L}^{-1}$ denotes the inverse Laplace transform.

(U) The second term on the right-hand side of Eq. (46) can be handled by a convolution integral:

$$\mathcal{L}^{-1}(f(s)\,g(s)) = \int_0^t F(t')\,G(t-t')\,dt' \,. \tag{48}$$

Let

$$f(s) = \frac{e^{-\frac{z}{\sqrt{\kappa}}\sqrt{s+\kappa\lambda^2}}}{s+\kappa\lambda^2} \,;$$

then

$$F(t') = e^{-\kappa\lambda^2 t'}\ \mathrm{erfc}\left(\frac{z}{2\sqrt{\kappa t'}}\right) . \tag{49}$$

Let

$$g(s) = 1/s \,;$$

then

$$G(t-t') = 1 = \text{constant} \,. \tag{50}$$

Substituting these results into Eq. (45) gives

$$T_1^{(1)} = \frac{T_f}{2a}\left[\int_0^\infty e^{-\lambda^2/4a}\,J_0(\lambda r)\,\lambda\,d\lambda\left(e^{-\kappa\lambda^2 t}\ \mathrm{erfc}\left(\frac{z}{2\sqrt{\kappa t}}\right)\right.\right.$$

$$\left.\left. + \kappa\lambda^2\int_0^t e^{-\kappa\lambda^2 t'}\ \mathrm{erfc}\left(\frac{z}{2\sqrt{\kappa t'}}\right)\,dt'\right)\right] \,. \tag{51}$$

The first term of Eq. (51) will be identified as

$$I_1 \equiv \mathrm{erfc}\left(\frac{z}{2\sqrt{\kappa t}}\right)\int_0^\infty \frac{\lambda\,e^{-\lambda^2\left(\kappa t+\frac{1}{4a}\right)}}{2a}\,J_0(\lambda r)\,d\lambda \,. \tag{52}$$

From G.R. (7),

$$I_1 = \frac{1}{2a}\,\mathrm{erfc}\left(\frac{z}{2\sqrt{\kappa t}}\right)\frac{1}{2\left(\kappa t+\frac{1}{4a}\right)}\,\exp\left(\frac{-r^2}{4\left(\kappa t+\frac{1}{4a}\right)}\right)$$

$$= \frac{e^{-\frac{r^2 a}{4\kappa a t+1}}}{4\kappa a t+1}\,\mathrm{erfc}\left(\frac{z}{2\sqrt{\kappa t}}\right) . \tag{53}$$

Assuming that the order of the integrations can be changed in the second term in Eq. (51), this term can be rewritten as

$$T_f \kappa \int_0^t \operatorname{erfc}\left(\frac{z}{2\sqrt{\kappa t'}}\right) dt' \int_0^\infty \frac{\lambda^3}{2a}\, e^{-\lambda^2\left(\kappa t' + \frac{1}{4a}\right)} J_0(\lambda r)\, d\lambda$$

$$= T_f \kappa \int_0^t \operatorname{erfc}\left(\frac{z}{2\sqrt{\kappa t'}}\right) dt'\, I_2$$

where, from G.R. (7),

$$I_2 \equiv \int_0^\infty \frac{\lambda^3}{2a}\, e^{-\lambda^2\left(\kappa t' + \frac{1}{4a}\right)} J_0(\lambda r)\, d\lambda$$

$$= \frac{\Gamma(2)\, e^{\frac{-r^2}{8\left(\kappa t' + \frac{1}{4a}\right)}}}{2ar\left[\kappa t' + \frac{1}{4a}\right]^{3/2}} M_{\frac{3}{2},0}\left(\frac{r^2}{4\left(\kappa t' + \frac{1}{4a}\right)}\right). \tag{54}$$

Now

$$M_{n+\mu+\frac{1}{2},\mu}(x) = \frac{x^{1/2-\mu}\, e^{x/2}}{(2\mu+1)(2\mu+2)\cdots(2\mu+n)} \frac{d^n}{dx^n}\left(x^{n+2\mu}\, e^{-x}\right).$$

Here $\mu = 0$, $n = 1$, so

$$M_{\frac{3}{2},0}(x) = x^{1/2}\, e^{x/2} \frac{d}{dx}\left(xe^{-x}\right) = x^{1/2}\, e^{x/2}\left(e^{-x} - xe^{-x}\right)$$

$$= e^{-x/2}\left(x^{1/2} - x^{3/2}\right).$$

Therefore, since $\Gamma(2) = 1$,

$$I_2 = \frac{e^{\frac{-r^2 a}{2(4\kappa a t'+1)}}}{\frac{2ar}{8a^{3/2}}\left[4\kappa a t' + 1\right]^{3/2}} \left\{ e^{-\frac{r^2 a}{2(4\kappa a t'+1)}} \left[\left(\frac{r^2 a}{4\kappa a t' + 1}\right)^{1/2} - \left(\frac{r^2 a}{4\kappa a t' + 1}\right)^{3/2} \right] \right\}$$

$$= 4a\, e^{-\frac{r^2 a}{4\kappa a t'+1}} \left(\frac{1}{(4\kappa a t' + 1)^2} - \frac{r^2 a}{(4\kappa a t' + 1)^3} \right). \tag{55}$$

Substitution of Eqs. (53) and (55) into Eq. (51) gives

$$T_1^{(1)} = T_f \left[\frac{e^{-\frac{r^2 a}{4\kappa a t + 1}}}{4\kappa a t + 1} \operatorname{erfc}\left(\frac{z}{2\sqrt{\kappa t'}}\right) \right.$$

$$\left. + 4\kappa a \int_0^t dt' \, e^{-\frac{r^2 a}{4\kappa a t' + 1}} \operatorname{erfc}\left(\frac{z}{2\sqrt{\kappa t'}}\right)\left(\frac{1}{(4\kappa a t' + 1)^2} - \frac{r^2 a}{(4\kappa a t' + 1)^3}\right)\right] . \tag{56}$$

(U) Finally, by going back to Eq. (44) and writing down the analogous integral for the expression involving T_a, λ, and ϵ, the final first-guess solution can be written:

$$T^{(1)}(r, z, t) = T_f \left[\frac{e^{-\frac{r^2 a}{4\kappa a t + 1}}}{4\kappa a t + 1} \operatorname{erfc}\left(\frac{z}{2\sqrt{\kappa t}}\right) \right.$$

$$\left. + 4\kappa a \int_0^t dt' \, e^{-\frac{r^2 a}{4\kappa a t' + 1}} \operatorname{erfc}\left(\frac{z}{2\sqrt{\kappa t'}}\right)\left(\frac{1}{(4\kappa a t' + 1)^2} - \frac{r^2 a}{(4\kappa a t' + 1)^3}\right)\right]$$

$$- T_a \left[\frac{e^{-\frac{r^2 \epsilon}{4\kappa \epsilon t + 1}}}{4\kappa \epsilon t + 1} \operatorname{erfc}\left(\frac{z}{2\sqrt{\kappa t}}\right) \right.$$

$$\left. + 4\kappa \epsilon \int_0^t dt' \, e^{-\frac{r^2 \epsilon}{4\kappa \epsilon t' + 1}} \operatorname{erfc}\left(\frac{z}{2\sqrt{\kappa t'}}\right)\left(\frac{1}{(4\kappa \epsilon t' + 1)^2} - \frac{r^2 \epsilon}{(4\kappa \epsilon t' + 1)^3}\right)\right]$$

$$+ T_a \, e^{-\epsilon(r^2 + 4\kappa t)} . \tag{57}$$

Taking the limit as $\epsilon \to 0$ gives

$$T^{(1)}(r, z, t) = T_f \left[\frac{e^{-\frac{r^2 a}{4\kappa a t + 1}}}{4\kappa a t + 1} \operatorname{erfc}\left(\frac{z}{2\sqrt{\kappa t}}\right) \right.$$

$$\left. + 4\kappa a \int_0^t dt' \, e^{-\frac{r^2 a}{4\kappa a t' + 1}} \operatorname{erfc} \frac{z}{2\sqrt{\kappa t'}} \left(\frac{1}{(4\kappa a t' + 1)^2} - \frac{r^2 a}{(4\kappa a t' + 1)^3}\right)\right]$$

$$+ T_a \left[1 - \operatorname{erfc}\left(\frac{z}{2\sqrt{\kappa t}}\right)\right] . \tag{58}$$

For $t \to 0$, Eq. (58) becomes

$$T^{(1)}(r, z, t) \underset{t \to 0}{\longrightarrow} T_a \ .$$

(U) Now for $t \to \infty$, the coefficient of T_a vanishes, and the first term of the coefficient of T_a vanishes. So for $z = 0$, and $t \to \infty$,

$$T^{(1)}(r, o, t) \underset{t \to \infty}{\longrightarrow} 4\kappa a T_f \int_0^\infty dt' \, e^{-\frac{r^2 a}{4\kappa a t' + 1}} \left(\frac{1}{(4\kappa a t' + 1)^2} - \frac{r^2 a}{(4\kappa a t' + 1)^3} \right) . \tag{59}$$

The integrals involved in Eq. (59) are of the form

$$I(n) = \int_0^\infty e^{-\frac{r^2 a}{4\kappa a t' + 1}} \frac{1}{(4\kappa a t' + 1)^n} \, dt' \ . \tag{60}$$

Let

$$x = \frac{1}{4\kappa a t' + 1}$$

so that

$$dx = - \frac{4\kappa a \, dt'}{(4\kappa a t' + 1)^2} = -4\kappa a x^2 \, dt' \ ,$$

from which

$$dt' = - \frac{dx}{4\kappa a x^2} \ .$$

When $t' = 0$, $x = 1$, and when $t' = \infty$, $x = 0$. With these relations Eq. (60) can be written

$$I(n) \longrightarrow \int_1^0 e^{-r^2 a x} \, x^n \left(- \frac{dx}{4\kappa a x^2} \right)$$

$$= \frac{1}{4\kappa a} \int_0^1 e^{-r^2 a x} \, x^{n-2} \, dx \ . \tag{61}$$

(U) For the first integral in Eq. (59), $n = 2$. Therefore

$$I(2) = \frac{1}{4\kappa a} \int_0^1 e^{-r^2 a x} \, dx = - \frac{e^{-r^2 a x}}{4\kappa r^2 a^2} \Bigg|_0^1$$

$$= \frac{1}{4\kappa r^2 a^2} \left(1 - e^{-r^2 a}\right) \ . \tag{62}$$

(U) For the second integral in Eq. (59), $n = 3$. Therefore

$$I(3) = \frac{1}{4\kappa a} \int_0^1 e^{-r^2 a x}\, x(-r^2 a)\, dx \,.$$

To integrate by parts let

$$u = x \quad , \quad dv = e^{-r^2 a x}(-r^2 a\, dx) \,,$$

so that

$$du = dx \,, \qquad v = e^{-r^2 a x} \,.$$

Thus,

$$I(3) = \frac{1}{4\kappa a}\left(x\, e^{-r^2 a x}\right)\Bigg|_0^1 - \frac{1}{4\kappa a}\int_0^1 e^{-r^2 a x}\, dx$$

$$= \frac{1}{4\kappa a}\left[e^{-r^2 a} - \frac{1}{r^2 a}\left(1 - e^{-r^2 a}\right)\right]. \tag{63}$$

(U) Substituting Eqs. (62) and (63) into Eq. (59) gives

$$T^{(1)}(r, o, t) \xrightarrow[t\to\infty]{} T_f\left[\left(\frac{1 - e^{-r^2 a}}{r^2 a}\right) + e^{-r^2 a} - \left(\frac{1 - e^{-r^2 a}}{r^2 a}\right)\right]$$

$$= T_f\, e^{-r^2 a} \,. \tag{64}$$

For $r \to 0$, Eq. (64) becomes $T(0,0,\infty) \to T_f$ in agreement with the one-dimensional case.

(U) For $a = 0$ (a Gaussian of infinite width or a constant power density), Eq. (58) reduces to

$$T^{(1)}(o, z, t) = T_a + (T_f - T_a)\ \mathrm{erfc}\left(\frac{z}{2\sqrt{\kappa t}}\right). \tag{65}$$

By comparison with Eq. (20), it may be seen that this first approximate solution does not agree with the previously obtained one-dimensional solution; hence a better approximation is necessary.

(U) This second approximation can be obtained by letting

$$f(\lambda) = f_0(\lambda) + \delta(\lambda) \tag{66}$$

and substituting into the boundary condition (Eq. (36)). The resulting expression is

$$\frac{k}{2\pi i}\oint e^{st}\,ds\int_0^\infty \sqrt{\frac{s}{\kappa}+\lambda^2}\;J_0(\lambda r)\,(f_0+\delta)\,\lambda d\lambda$$

$$= \alpha P(r) - \sigma\left(\frac{1}{2\pi i}\oint e^{st}\,ds\int_0^\infty J_0(\lambda r)\,(f_0+\delta)\,\lambda d\lambda + \frac{1}{2\pi i}\oint \frac{e^{st}\,ds\;T_a\;e^{-\epsilon r^2}}{s+4\kappa\epsilon}\right)^4$$

$$+ \sigma T_a^4\; e^{-4\epsilon r^2}$$

$$= \alpha P(r) - \sigma\left[\left(\frac{1}{2\pi i}\oint e^{st}\,ds\int_0^\infty J_0(\lambda r)\,f_0\,\lambda d\lambda + \frac{T_a\;e^{-\epsilon r^2}}{2\pi i}\oint\frac{e^{st}\,ds}{s+4\kappa\epsilon}\right)\right.$$

$$\left. + \frac{1}{2\pi i}\oint e^{st}\,ds\int_0^\infty J_0(\lambda r)\,\delta\,\lambda d\lambda\right]^4$$

$$+ \sigma T_a^4\; e^{-4\epsilon r^2}\;. \qquad (67)$$

(U) At this point, use is made of the "first-guess" solution, and this expression (Eq. (37)) is substituted for the term inside the parentheses on the right-hand side of Eq. (67). The boundary condition becomes

$$\frac{k}{2\pi i}\oint e^{st}\,ds\int_0^\infty \sqrt{\frac{s}{\kappa}+\lambda^2}\;J_0(\lambda r)\,(f_0+\delta)\,\lambda d\lambda$$

$$= \alpha P(r) - \sigma\left[\left(\frac{\alpha P(r)}{\sigma} + T_a^4\;e^{-4\epsilon r^2}\right)^{1/4} + \frac{1}{2\pi i}\oint e^{st}\,ds\int_0^\infty J_0(\lambda r)\,\delta\lambda d\lambda\right]^4$$

$$+ \sigma T_a^4\; e^{-4\epsilon r^2}$$

$$\approx \alpha P(r) - \alpha P(r) - \sigma T_a^4\; e^{-4\epsilon r^2}$$

$$-4\sigma\left[\left(\frac{\alpha P(r)}{\sigma} + T_a\;e^{-4\epsilon r^2}\right)^{3/4}\frac{1}{2\pi i}\oint e^{st}\,ds\int_0^\infty J_0(\lambda r)\,\delta\lambda d\lambda\right] + \sigma T_a^4\;e^{-4\epsilon r^2}\;.$$

Therefore,

$$\frac{k}{2\pi i}\oint e^{st}\,ds\int_0^\infty \sqrt{\frac{s}{\kappa}+\lambda^2}\;J_0(\lambda r)\,(f_0+\delta)\;\lambda\,d\lambda$$

$$\approx -4\sigma T_f^3\,g(r)^{3/4}\,\frac{1}{2\pi i}\oint e^{st}\,ds\int_0^\infty J_0(\lambda r)\;\delta(\lambda)\;\lambda\,d\lambda\;\ldots \tag{68}$$

by using Eq. (39).

(U) Both sides of Eq. (68) are multiplied by $J_0(\mu r)\,r\,dr$ and integrated from $r = 0$ to $r = \infty$. Then

$$\int_0^\infty k\sqrt{\frac{s}{\kappa}+\lambda^2}\;(f_0(\lambda)+\delta(\lambda))\;J_0(\lambda r)\;\lambda\,d\lambda\int_0^\infty J_0(\mu r)\;r\,dr = k\sqrt{\frac{s}{\kappa}+\mu^2}\;\left[f_0(\mu)+\delta(\mu)\right] \tag{69}$$

since this is just the Fourier-Bessel integral. It may be seen that an integral equation for $\delta(\lambda)$ will result after the integration over r is performed on the right side. For $g(r) = e^{-4ar^2}$, most of the contribution to the integration over r comes near $r \approx 0$. If it is assumed that $3ar^2 \ll 1$ or $r \ll (3a)^{-1/2}$, then $e^{-3ar^2} \approx 1$, and the expression on the right of Eq. (68) is greatly simplified; it just becomes a Fourier-Bessel integral. Hence,

$$k\sqrt{\frac{s}{\kappa}+\lambda^2}\;\left[f_0(\lambda)+\delta(\lambda)\right] = -4\sigma T_f^3\,\delta(\lambda)\;,$$

from which

$$\delta(\lambda) = -\frac{\sqrt{s+\kappa\lambda^2}}{\sqrt{s+\kappa\lambda^2}+\gamma}\,f_0(\lambda) \tag{70}$$

where γ is defined by Eq. (16) as before. Therefore,

$$f(\lambda) \equiv f_0(\lambda)+\delta(\lambda) = \frac{\gamma\,f_0(\lambda)}{\sqrt{s+\kappa\lambda^2}+\gamma}$$

$$= \frac{\gamma}{\sqrt{s+\kappa\lambda^2}+\gamma}\left(\frac{T_f\,e^{-\lambda^2/4a}}{2as}-\frac{T_a\,e^{-\lambda^2/4\epsilon}}{2\epsilon s}\right) \tag{71}$$

using Eqs. (43) and (66), again ignoring terms of the order of ϵ^2. Substituting Eq. (71) into Eq. (35), the "second-guess" solution becomes

$$T^{(2)}(r,z,t) = \frac{1}{2\pi i}\oint e^{st}\,ds\int_0^\infty J_0(\lambda r)\;e^{-z\sqrt{\frac{s}{\kappa}+\lambda^2}}\left(\frac{T_f\,e^{-\lambda^2/4\epsilon}}{2as}-\frac{T_a\,e^{-\lambda^2/4\epsilon}}{2\epsilon s}\right)$$

$$\frac{\gamma\,\lambda\,d\lambda}{\sqrt{s+\kappa\lambda^2}+\gamma}+T_a\,e^{-\epsilon(r^2+4\kappa t)}\;. \tag{72}$$

(U) Since the integrals inside the parentheses are again similar, it is only necessary to calculate one of them, and the other one can be written down by analogy. By interchanging the order of the integration, the first term may be written

$$T_1^{(2)} = \frac{\gamma T_f}{2a} \int_0^\infty e^{-\lambda^2/4a} J_0(\lambda r)\, \lambda d\lambda \left(\frac{1}{2\pi i}\right) \oint e^{st}\, ds \frac{e^{-\frac{z}{\sqrt{\kappa}}\sqrt{s+\kappa\lambda^2}}}{s\left(\sqrt{s+\kappa\lambda^2}+\gamma\right)} \quad . \tag{73}$$

Now

$$\frac{1}{s\left(\sqrt{s+\kappa\lambda^2}+\gamma\right)} = \frac{1}{(s+\kappa\lambda^2)\left(\sqrt{s+\kappa\lambda^2}+\gamma\right)} \left(\frac{s+\kappa\lambda^2}{s}\right)$$

$$= \frac{1}{(s+\kappa\lambda^2)\left(\sqrt{s+\kappa\lambda^2}+\gamma\right)} + \frac{\kappa\lambda^2}{s(s+\kappa\lambda^2)\left(\sqrt{s+\kappa\lambda^2}+\gamma\right)} \quad . \tag{74}$$

From the Shift Theorem for Laplace transforms, and from Eqs. (18)-(20), it may be seen that

$$\frac{1}{2\pi i} \oint \frac{e^{st}\, e^{-\frac{z}{\sqrt{\kappa}}\sqrt{s+\kappa\lambda^2}}}{(s+\kappa\lambda^2)\left(\sqrt{s+\kappa\lambda^2}+\gamma\right)}\, ds = \frac{e^{-\kappa\lambda^2 t}}{\gamma}\left[\operatorname{erfc}\left(\frac{z}{2\sqrt{\kappa t}}\right) - e^{\frac{\gamma z}{\sqrt{\kappa}}+\gamma^2 t} \operatorname{erfc}\left(\gamma\sqrt{t}+\frac{z}{2\sqrt{\kappa t}}\right)\right]. \tag{75}$$

The second term may be done as a convolution integral by letting

$$f(s) = \frac{e^{-\frac{z}{\sqrt{\kappa}}\sqrt{s+\kappa\lambda^2}}}{\left(\sqrt{s+\kappa\lambda^2}+\gamma\right)(s+\kappa\lambda^2)}$$

and (76)

$$g(s) = \frac{1}{s} \Longrightarrow G(t-t') = 1 = \text{constant} \quad .$$

Then Eq. (73) becomes

$$T_1^{(2)} = T_f\left[\operatorname{erfc}\left(\frac{z}{2\sqrt{\kappa t}}\right) - e^{\frac{\gamma z}{\sqrt{\kappa}}+\gamma^2 t} \operatorname{erfc}\left(\gamma\sqrt{t}+\frac{z}{2\sqrt{\kappa t}}\right)\right]\int_0^\infty \frac{J_0(\lambda r)}{2a}\, e^{-\lambda^2\left(\kappa t+\frac{1}{4a}\right)} \lambda d\lambda$$

$$+ \kappa T_f \int_0^t dt' \left[\operatorname{erfc}\left(\frac{z}{2\sqrt{\kappa t'}}\right)\right.$$

$$\left. - e^{\frac{\gamma z}{\sqrt{\kappa}}+\gamma^2 t'} \operatorname{erfc}\left(\gamma\sqrt{t'}+\frac{z}{2\sqrt{\kappa t'}}\right)\right]\int_0^\infty \frac{J_0(\lambda r)}{2a}\, e^{-\lambda^2\left(\kappa t'+\frac{1}{4a}\right)} \lambda^3 d\lambda \quad . \tag{77}$$

The λ-integrals have been calculated previously (Eqs. (52)-(55)); making use of these results gives

$$T_1^{(2)} = T_f \left[\operatorname{erfc}\left(\frac{z}{2\sqrt{\kappa t}}\right) - e^{\frac{\gamma z}{\sqrt{\kappa}} + \gamma^2 t} \operatorname{erfc}\left(\gamma\sqrt{t} + \frac{z}{2\sqrt{\kappa t}}\right)\right] \frac{e^{-\frac{r^2 a}{4\kappa a t + 1}}}{4\kappa a t + 1}$$

$$+ 4\kappa a\, T_f \int_0^t dt'\, e^{-\frac{r^2 a}{4\kappa a t' + 1}} \left[\frac{1}{(4\kappa a t' + 1)^2} - \frac{r^2 a}{(4\kappa a t' + 1)^3}\right]$$

$$\times \left[\operatorname{erfc}\left(\frac{z}{2\sqrt{\kappa t'}}\right) - e^{\frac{\gamma z}{\sqrt{\kappa}} + \gamma^2 t'} \operatorname{erfc}\left(\gamma\sqrt{t'} + \frac{z}{2\sqrt{\kappa t'}}\right)\right] . \tag{78}$$

(U) By replacing a by ϵ, the second bracketed term in Eq. (72) can be written now, and the final result for the "second-guess" solution is

$$T^{(2)}(r, z, t) = T_f \left\{ \left[\operatorname{erfc}\left(\frac{z}{2\sqrt{\kappa t}}\right) - e^{\frac{\gamma z}{\sqrt{\kappa}} + \gamma^2 t} \operatorname{erfc}\left(\gamma\sqrt{t} + \frac{z}{2\sqrt{\kappa t}}\right)\right] \frac{e^{-\frac{r^2 a}{4\kappa a t + 1}}}{4\kappa a t + 1} \right.$$

$$+ 4\kappa a \int_0^t dt'\, e^{-\frac{r^2 a}{4\kappa a t' + 1}} \left[\frac{1}{(4\kappa a t' + 1)^2} - \frac{r^2 a}{(4\kappa a t' + 1)^3}\right]$$

$$\left. \times \left[\operatorname{erfc}\left(\frac{z}{2\sqrt{\kappa t'}}\right) - e^{\frac{\gamma z}{\sqrt{\kappa}} + \gamma^2 t'} \operatorname{erfc}\left(\gamma\sqrt{t'} + \frac{z}{2\sqrt{\kappa t'}}\right)\right] \right\}$$

$$- T_a \left\{ \left[\operatorname{erfc}\left(\frac{z}{2\sqrt{\kappa t}}\right) - e^{\frac{\gamma z}{\sqrt{\kappa}} + \gamma^2 t} \operatorname{erfc}\left(\gamma\sqrt{t} + \frac{z}{2\sqrt{\kappa t}}\right)\right] \frac{e^{-\frac{r^2 \epsilon}{4\kappa \epsilon t + 1}}}{4\kappa \epsilon t + 1} \right.$$

$$+ 4\kappa\epsilon \int_0^t dt'\, e^{-\frac{r^2 \epsilon}{4\kappa \epsilon t' + 1}} \left[\frac{1}{(4\kappa\epsilon t' + 1)^2} - \frac{r^2 \epsilon}{(4\kappa\epsilon t' + 1)^3}\right]$$

$$\left. \times \left[\operatorname{erfc}\left(\frac{z}{2\sqrt{\kappa t'}}\right) - e^{\frac{\gamma z}{\sqrt{\kappa}} + \gamma^2 t'} \operatorname{erfc}\left(\gamma\sqrt{t'} + \frac{z}{2\sqrt{\kappa t'}}\right)\right] \right\}$$

$$+ T_a\, e^{-\epsilon(r^2 + 4\kappa t)} . \tag{79}$$

In the limit as $\epsilon \to 0$ there is obtained

$$T^{(2)}(r,z,t) = T_f \left\{ \frac{e^{-\frac{r^2 a}{4\kappa a t+1}}}{4\kappa a t + 1} \left[\operatorname{erfc}\left(\frac{z}{2\sqrt{\kappa t}}\right) - e^{\frac{\gamma z}{\sqrt{\kappa}} + \gamma^2 t} \operatorname{erfc}\left(\gamma\sqrt{t} + \frac{z}{2\sqrt{\kappa t}}\right) \right] \right.$$

$$+ 4\kappa a \int_0^t dt' \, e^{-\frac{r^2 a}{4\kappa a t'+1}} \left[\frac{1}{(4\kappa a t' + 1)^2} - \frac{r^2 a}{(4\kappa a t' + 1)^3} \right]$$

$$\left. \times \left[\operatorname{erfc}\left(\frac{z}{2\sqrt{\kappa t'}}\right) - e^{\frac{\gamma z}{\sqrt{\kappa}} + \gamma^2 t'} \operatorname{erfc}\left(\gamma\sqrt{t'} + \frac{z}{2\sqrt{\kappa t'}}\right) \right] \right\}$$

$$+ T_a \left\{ 1 - \left[\operatorname{erfc}\left(\frac{z}{2\sqrt{\kappa t}}\right) - e^{\frac{\gamma z}{\sqrt{\kappa}} + \gamma^2 t} \operatorname{erfc}\left(\gamma\sqrt{t} + \frac{z}{2\sqrt{\kappa t}}\right) \right] \right\}. \tag{80}$$

For $t \to 0$, Eq. (80) becomes $T(r,z,t) \to T_a$. For $t \to \infty$,

$$T(r,z,t) \longrightarrow 4\kappa a T_f \int_0^\infty dt' \, e^{-\frac{r^2 a}{4\kappa a t'+1}} \left[\frac{1}{(4\kappa a t' + 1)^2} - \frac{r^2 a}{(4\kappa a t' + 1)^3} \right]$$

$$\times \left[\operatorname{erfc}\left(\frac{z}{2\sqrt{\kappa t'}}\right) - e^{\frac{\gamma z}{\sqrt{\kappa}} + \gamma^2 t'} \operatorname{erfc}\left(\gamma\sqrt{t'} + \frac{z}{2\sqrt{\kappa t'}}\right) \right]. \tag{81}$$

For $z = 0$ and $t \to \infty$,

$$T(r,o,\infty) \longrightarrow 4\kappa a T_f \int_0^\infty dt' \, e^{-\frac{r^2 a}{4\kappa a t'+1}} \left[\frac{1}{(4\kappa a t' + 1)^2} - \frac{r^2 a}{(4\kappa a t' + 1)^3} \right] \left[1 - e^{\gamma^2 t'} \operatorname{erfc}\left(\gamma\sqrt{t'}\right) \right]. \tag{82}$$

(U) Near $t' = 0$, the quantity $1 - e^{\gamma^2 t'} \operatorname{erfc}(\gamma\sqrt{t'}) \approx 0$. The contributions from this term are for large t'; as $t' \to \infty$, $1 - e^{\gamma^2 t'} \operatorname{erfc}(\gamma\sqrt{t'}) \to 1$. Therefore, from Eqs. (60)-(64), $T(r,o,t) \to T_f \, e^{-r^2 a}$ as $t \to \infty$; for $r = 0$, $T(o,o,t) \to T_f$ as $t \to \infty$ in agreement with the one-dimensional case. For $a = 0$ (constant beam power), Eq. (80) becomes

$$T(r,z,t) = (T_f - T_a) \left[\operatorname{erfc}\left(\frac{z}{2\sqrt{\kappa t}}\right) - e^{\frac{\gamma z}{\sqrt{\kappa}} + \gamma^2 t} \operatorname{erfc}\left(\gamma\sqrt{t} + \frac{z}{2\sqrt{\kappa t}}\right) \right] + T_a \tag{83}$$

which is identical to the one-dimensional solution already obtained (Eq. (20)); thus, the three-dimensional and the one-dimensional solutions are consistent.

(C) Equation (80) has been programmed for a digital computer, and calculations have been made using values of the thermal parameters for zinc as given in Table 1. The calculations were made assuming a total laser power P_t of 150 kW. A Gaussian power distribution is chosen with $a = 0.157\ \text{cm}^{-2}$, which corresponds to a $1/e$ point of about 1.25 cm. This gives a peak power density P_0 of 30 kW/cm^2.

(U) Figure 3 shows the computed variations of the temperature as a function of z and t. In Fig. 3, r is taken as zero; thus, this is the temperature distribution along the axis of the beam. At the surface, the temperature rises sharply from zero as expected. For $z > 0$, the temperature rises more slowly; this is due to the finite time it takes the material to conduct heat from the surface to the inner regions of the solid. All the curves are asymptotic to the final equilibrium temperature T_f.

(U) Figures 4 and 5 show the behavior of the temperature as a function of r and t for two planes in the material — the $z = 0$ plane (Fig. 4) and the $z = 0.1$ cm plane (Fig. 5). These curves are presented to indicate the calculated temperature distributions at a given constant distance from the surface.

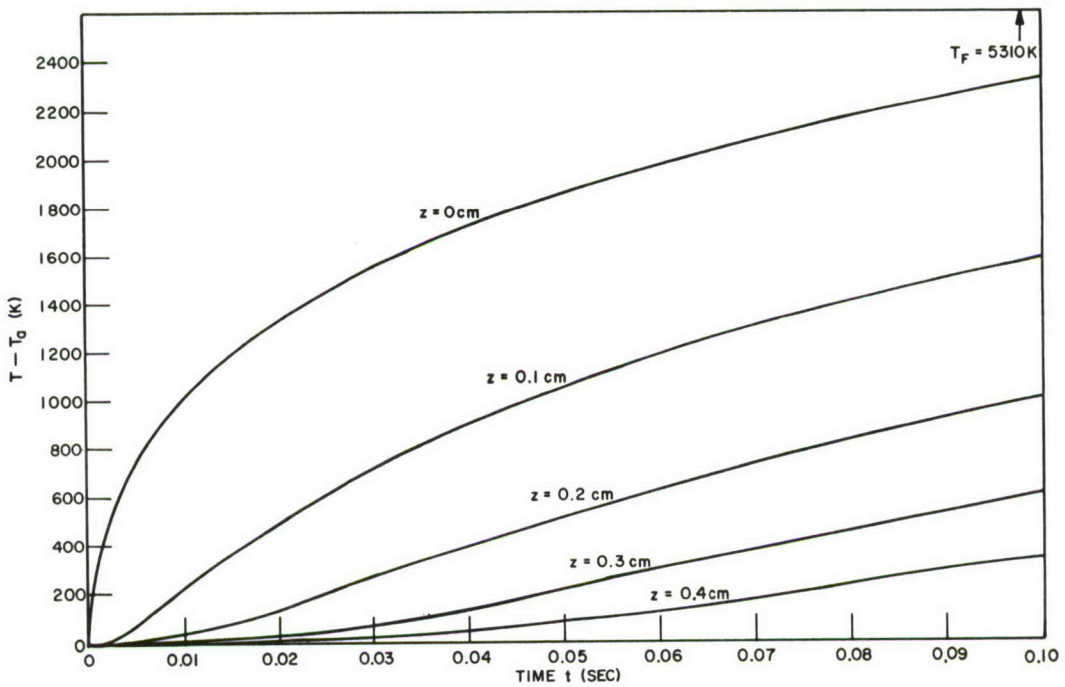

Fig. 3 - Theoretical temperature distribution for a zinc target irradiated by a laser beam. Each curve shows the variation of temperature with time for that particular location (or value of z) within the target; z is measured in the direction of the laser beam (normal to the target surface). The incident beam's peak power density P_0 is 30 kW/cm^2, its total power P_t is 150 kW, and a is 0.157 cm^{-2} in the power distribution relation $P = P_0\, e^{-4ar^2}$. The case considered here is three dimensional, i.e., $T = T(r = o, z, t)$.

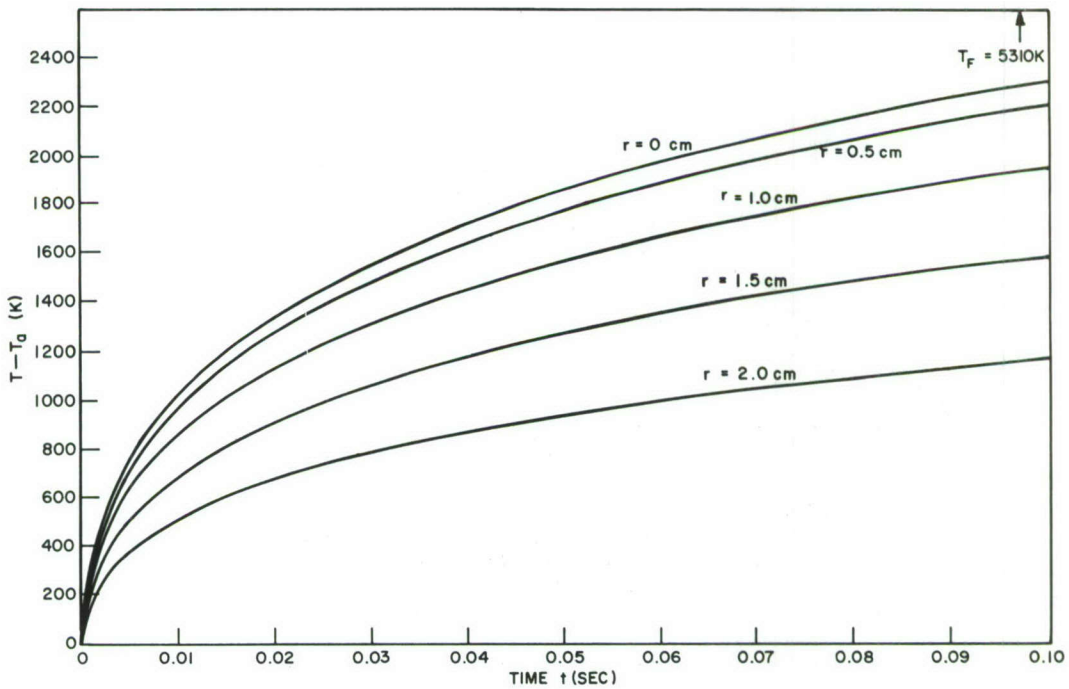

Fig. 4 - Theoretical temperature distribution for a zinc target irradiated by a laser beam. Each curve shows the variation of temperature with time at a given distance r measured perpendicular to the axis of the laser beam. The distances r are located on the target's surface (z = 0 cm plane). The incident beam's peak power density P_0 is 30 kW/cm^2, its total power P_t is 150 kW, and a is 0.157 cm^{-2} in the power distribution relation $P = P_0\ e^{-4ar^2}$. The case considered here is three dimensional, i.e., $T = T(r, z = o, t)$.

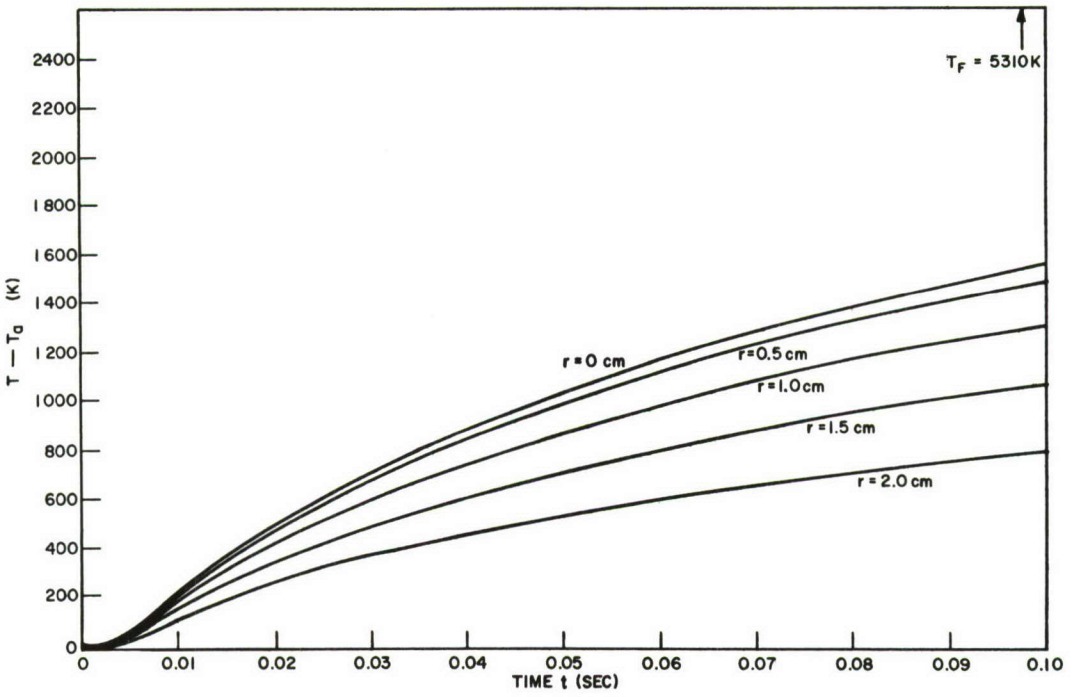

Fig. 5 - Theoretical temperature distribution for a zinc target irradiated by a laser beam. Each curve shows the variation of temperature with time at a given distance r measured perpendicular to the axis of the laser beam. The distances r are located at a depth of 0.1 cm beneath the target's surface (z = 0.1 cm plane). The incident beam's peak power density P_0 is 30 kW/cm^2, its total power P_t is 150 kW, and a is 0.157 cm^{-2} in the power distribution relation $P = P_0\ e^{-4ar^2}$. The case considered here is three dimensional, i.e., $T = T(r, z = 0.1, t)$.

(U) A comparison of Figs. 2 and 3 is interesting because they correspond to the same incident power density at the same point on the surface. However, it can be seen that the temperatures are higher for the constant power case (Fig. 2), and the difference gets greater for larger z values. This is due to the fact that the power densities, and hence the temperatures, are lower away from the center of the beam for the Gaussian distribution case, and therefore heat is conducted away from the center more readily than in the constant power case.

CONCLUSIONS

(U) Figure 2 indicates the type of behavior that might be expected intuitively for this problem; in that respect, the results seem physically reasonable.

(U) However, there are obvious shortcomings in the theory. Because of the nonlinearity of the boundary condition, it was necessary to make assumptions and approximations in the development of the solution; hence the solution is not rigorous. Moreover, neither melting of the material nor plasma formation due to vaporization is treated; these may certainly occur for sufficiently high power densities. In this sense also, the theory is incomplete.

(U) In spite of these faults, the theory should be of some practical value. For instance, it should be possible to make a reasonable estimate of the time required to cause surface melting for a given material and a given power distribution.

(U) In summary, then, this result is to be taken as merely a first approximation to the problem; it is not presented as a complete solution. It is anticipated that improvements or complete revisions will come in the future. For example, the next step is to include temperature-dependent parameters. Changes of state of the material could be included later.

REFERENCES

1. Pyatt, K.D., Jr., "Interaction of the Radiation Produced by a Laser with a Solid Target," Journal of Missile Defense Research, Vol. II, No. 1, Institute for Defense Analysis, Alexandria, Va., Summer 1964 (Secret Report, Unclassified Title)

2. Allen, F.J., and Lyman, O.R., "Studies of the Effects Produced by Laser Beam Bombardment of Surfaces," Report No. 1373, U.S. Army Materiel Command, Ballistic Research Laboratories, Aberdeen Proving Ground, Maryland, August 1967 (Confidential Report, Unclassified Title)

3. Skeen, C.H., and York, C.M., "Laser-Induced 'Blow-Off' Phenomena," Appl. Phys. Letters, 12 (No. 11):369 (June 1968)

4. Sooy, W.R., Air Force Weapons Laboratory, Technical Report 66-158, June 1967 (Secret Report)

5. Spiegel, M.R., "Theory and Problems of Laplace Transforms," New York:Schaum, 1965

6. Ditkin, V.A., and Prudnikov, A.P., "Integral Transforms and Operational Calculus," p. 71, London:Pergamon, 1965

7. Gradshteyn, I.S., and Ryzhik, I.M., "Table of Integrals, Series, and Products," 4th ed., New York:Academic, 1965

Appendix J
[Unclassified]

HIGH-ENERGY LOADING ON MIRROR DEVICES AT 10.6 μm

Michael H. Reilly and Raymond A. Patten
Optical Sciences Division

INTRODUCTION

Present high-energy lasers employ several mirrors in the beam-folding optics. Three mirrors are employed in the amplifier cavity. The laser beam exits from the amplifier at full strength through a windowless aperture onto a folding mirror which directs it to other steering mirrors. The mirror presently used is evaporated copper or silver on a thick copper substrate, imbedded in which is an elaborate system of water cooling channels and Invar supporting rods. On top of the evaporated copper or silver film is a very thin protective fluoride film to prevent environmental attack. The rated reflectances of these mirrors are 99.2 to 99.5 percent. The part which is not reflected is absorbed in the mirror, which thus heats up the mirror, and the resulting mirror distortion (from thermal expansion) has destructive optical consequences. It is the function of water cooling to minimize temperature rise of the loaded mirror surface and the function of Invar supporting rods to minimize the surface distortion. Another technique is to make the laser beam and mirror area large enough to reduce the loading per unit area on the mirror.

The fabrication of these mirrors is necessarily a complex and expensive process, and it should be much more so for the higher energy laser devices of the future. Evidently, a small improvement in mirror reflectance (e.g., by a few tenths of a percent) would result in substantially less mirror absorptance, and this latter reduction should be passed on to the size, design complexity, and expense of the mirrors and water cooling support system. This is the object of the present study.

In the next section a theoretical calculation shows that the use of reflective film coatings on the metal mirror surface is capable of reducing mirror absorptance by orders of magnitude and so appears very worthwhile indeed. Coordinated with theoretical mirror design is the measurement of actual mirror absorptance, and this is accomplished by a relatively simple and accurate optical experiment, as described in the third section. In the last section these results and future work are discussed.

REFLECTION COATINGS

Appropriate materials for use in reflection coatings at 10.6 μm should have small absorptivities. Some of the more outstanding low-index (of refraction) materials for this purpose are the alkali halides (KCl, KBr, NaCl), uranium fluoride, and several others (Ref. J1). Their absorptivities at 10.6 μm are generally smaller by far than those of other materials, but they are hygroscopic and have poor mechanical properties. This is not a serious drawback for present purposes if they are evaporated in high vacuum, relatively free of H_2O, and then overcoated with a nonreactive material. This would generally be a high-index material in reflection coatings, and many semiconductors are

probably suitable for this purpose, such as Ge, GaAs, CdS, CdTe, and ZnSe (Ref. J1). Some glasses are probably suitable materials as well.

What may be called a standard composition of reflection coatings by now is a stack of quarter-wavelength optical thicknesses of adjacent layers of a high-index material (H) and a low index material (L). The layer arrangement within the reflection coating to be deposited on the substrate, in this case a metal surface, is HLHL . . . HL = $(HL)^m$ if m HL pairs are to be used in the stack. To demonstrate the advantage of using such a reflection coating we have calculated the absorptance of a silver mirror overcoated with a quarter-wavelength stack consisting of m HL pairs vs m, where the H material is Ge and the L material is KCl. The results are shown in Fig. J1. The solid line includes absorptivity of the reflection coating; the dashed line neglects it. The indices of refraction (n) and extinction coefficients (k) given in Fig. J1 are bulk values for KCl and Ge (Ref. J1) and film values for silver (Ref. J2). Diffuse scattering is neglected, which is expected to be a valid approximation in practice. The use of the recursion relations for admittance (Ref. J3) was found to be simplest for this calculation.

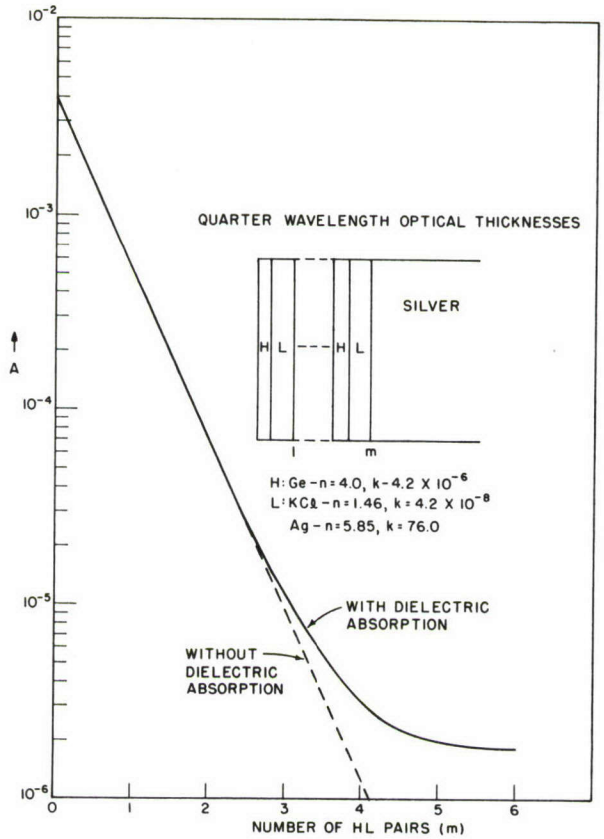

Fig. J1 - Computed mirror absorptance (A) vs number (m) of Ge-KCl pairs in a quarter wave stack reflection coating on a silver substrate

It is seen from Fig. J1 that absorptivity of a silver mirror is reduced by a factor of 2000 with five or six HL pairs, but that the absorption will increase with the addition of more pairs because of absorption within the reflection coating. Were it not for this the

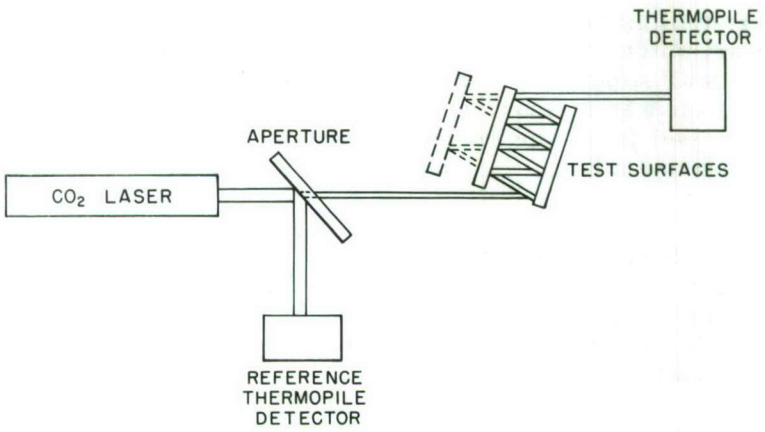

Fig. J2 - Schematic diagram of measurement apparatus for determining mirror absorptance using multiple reflections

absorptance of the mirror could be made arbitrarily small with the addition of more pairs. For 1 megawatt incident upon the mirror, the absorbed power would be reduced from 4000 watts to 2 watts by the use of this reflection coating. This is an example of the advantage of reflection coatings, not necessarily the optimum choice of one.

MEASUREMENT OF MIRROR ABSORPTANCE

The simplest determination of mirror absorptance A would be to measure specular reflectance R and relate it to A by A = 1 - R. Actually 1 - R measures total losses and includes diffuse scattering. But diffuse scattering is and can be made a relatively minor consideration in practice at 10.6 μm. Even if R is measured to typical 0.1-percent accuracy, however, A would be determined only to 20-percent accuracy for R = 00.5 percent. This difficulty has led other researchers to a type of calorimetry technique for measuring absorptance; a thermocouple detector is imbedded in the mirror, and the measured temperature rise is related to power absorbed from specific heat data. The accuracy is not high (e.g., 5 to 10 percent). We have adopted a relatively simple optical technique instead. The measurement apparatus is schematically depicted in Fig. J2. A CO_2 laser beam is bounced between two test mirror surfaces n times; i.e., R^n is measured to an accuracy δ. Adjustment of mirror spacing varies n. The basic advantage is that R is then determined to accuracy δ/n. Values of n = 20 are readily obtainable, and the reflectivity R is measurable to an accuracy of 0.005 percent or better. This claim has been verified by actual measurement. Hence, for example A can feasibly be determined to an accuracy of 1 percent or better for R = 99.5 percent.

DISCUSSION AND FUTURE WORK

The results of the present study indicate that reflection coatings should result in a great simplification of mirror design and reduction in cost. Indications that GaAs has appreciably lower absorptance than Ge, as well as other superior properties, make it appear as a worthy replacement for Ge in reflection coatings at 10.6 μm. Beside the capability in reflection coating design and measurement, we have the capability of fabricating mirrors with a delivered-high-vacuum evaporator. Reflection coating fabrication for 1.6 μm has been attempted to some degree in the past although not followed

through, and inferior films were found to result from poor vacuum preparation conditions. In particular, water vapor was found to be a serious offender in ordinary vacuums with, for example, NaCl films having absorptances 1000 times greater than the bulk value (Ref. J4). To eliminate water vapor contamination we have installed a liquid-nitrogen-cooled shroud in the bell jar of our evaporator. We also are scheduled to obtain an ultra-high-vacuum evaporator in the 10^{-12}-Torr range, which should virtually eliminate contamination problems.

We see no basic obstacle to mirror fabrication in agreement with the above theoretical predictions. It is certainly encouraging that this has been realized recently by Berthold (Ref. J5), who fabricated a 47-layer, quarter-wavelength, wideband dielectric mirror for use near 1 μm with measured reflectances in agreement with theory (neglecting diffuse scattering).

REFERENCES

J1. F. Horrigan et al., "Windows for High-Power Lasers," reprint, courtesy of Laser Optics, Inc., 1969

J2. H.E. Bennett and J.M. Bennett, in "Optical Properties and Electronic Structure of Metals and Alloys," North Holland, New York, 1966

J3. P.H. Berning, in "Physics of Thin Films," Vol. 1, academic press, New York, 1963

J4. R. Congleton, Hughes Aircraft, private communication

J5. J. Berthold, Applied Optics 8, 1919 (1969)

CONFIDENTIAL
Security Classification

DOCUMENT CONTROL DATA - R & D

(Security classification of title, body of abstract and indexing annotation must be entered when the overall report is classified)

1. ORIGINATING ACTIVITY (Corporate author)	2a. REPORT SECURITY CLASSIFICATION
Naval Research Laboratory Washington, D.C. 20390	Secret
	2b. GROUP 3

3. REPORT TITLE

NRL EIGHTH CARD PROGRAM INTERIM PROGRESS REPORT, 1 MARCH 1969 TO 30 SEPTEMBER 1969

4. DESCRIPTIVE NOTES (Type of report and inclusive dates)

An interim report

5. AUTHOR(S) (First name, middle initial, last name)

H.W. Gandy

6. REPORT DATE	7a. TOTAL NO. OF PAGES	7b. NO. OF REFS
December 31, 1969	142	48 plus App. A and B

8a. CONTRACT OR GRANT NO.	9a. ORIGINATOR'S REPORT NUMBER(S)
WRO-S419 b. PROJECT NO. ORD-0832-129/173-1/U1754 c. d.	NRL Memorandum Report 2072
	9b. OTHER REPORT NO(S) (Any other numbers that may be assigned this report)

10. DISTRIBUTION STATEMENT

EIGHTH CARD Program. This report may not be distributed further by the holder or released outside the holder's organization, except with the specific approval of ARPA/TIO. No distriubtion to DDC is authorized. This report may be cited, abstracted or quoted only in documents bearing the EIGHTH CARD notation. Information contained herin may be released only to persons known by the holder to be on the master access list of persons who have been authorized access to controlled EIGHTH CARD information.

11. SUPPLEMENTARY NOTES	12. SPONSORING MILITARY ACTIVITY
	Department of the Navy (Naval Ordnance Systems Command), Washington, D.C. 20360

13. ABSTRACT (Confidential)

This report presents the progress made at NRL in support of Advanced Development Objective (ADO) 17-54X, the High Energy Laser Program of the Navy, from the time of its initiation at the Laboratory in April 1969 through September 1969. This report includes both summary and detailed accounts of activities carried out in the three major areas of NRL responsibility: Site Implementation and Instrumentation, High-Power Propagation Test and Analysis, and Target and Materials Damage Test and Analysis.

DD FORM 1 NOV 65 1473 (PAGE 1)

S/N 0101-807-6801

CONFIDENTIAL
Security Classification

14. KEY WORDS	LINK A		LINK B		LINK C	
	ROLE	WT	ROLE	WT	ROLE	WT
Lasers Gas dynamics Gas lasers Carbon dioxide lasers						

CONFIDENTIAL

CONFIDENTIAL

Naval Research Laboratory
Technical Library
Research Reports Section

DATE: September 3, 2003

FROM: Mary Templeman, Code 5596.3

TO: **Code 6300 Dr. Gubser**

C: Tina Smallwood, Code 1221.1 ts 9/11/03

SUBJ: Review of NRL Memo Report

Dear Sir/Madam:

Please review NRL Memo Reports 2072,2089, 2149, 2162, 2197, 2222, 2274, 2349, 2382, 2421, 2453 for:

- ☑ Possible Distribution Statement
- ☑ Possible Change in Classification

Thank you,

Mary Templeman

Mary Templeman
(202)767-3425
maryt@library.nrl.navy.mil

The subject report can be:

- ☒ Changed to Distribution A (Unlimited)
- ☒ Changed to Classification Unclassified
- ☐ Other:

DL Gubser 9/3/03

Signature Date